New Collective structures in the Z=76 stable odd neutron nucleus, ^{187}Os

UNIVERSITY *of the*
WESTERN CAPE

by

Makuhane Abel Sithole

A thesis submitted in conformity with the requirements for the degree of Doctor of Philosophy

in the

Faculty of Science
Department of Physics

Supervisors: Prof. E. A. Lawrie
Dr. S. N. T. Majola
Dr. T. D. Bucher
Prof. J. F. Sharpey-Schafer

February 2022

Declaration

I, Makuhane Abel Sithole, declare that the *New collective structures in* ^{187}*Os nucleus, the Z = 76 stable odd neutron* is my own work, that it has not been submitted before for any degree or assessment at any other university, and that all the sources I have used or quoted have been indicated and acknowledged by means of complete references.

Signature:..... Date: 08 December 2021

"History of all great works is to witness that no great work was ever done without either the active or passive support a person's surrounding and one's close quarters"

John L. Macalisang

Abstract

Low- and medium-spin bands of ^{187}Os have been studied using the AFRODITE array, following the ^{186}W(^{4}He,3n)^{187}Os reaction at a beam energy of 37 MeV. The measurements of $\gamma - \gamma$ coincidences, angular distribution ratios (R_{AD}), polarization and γ-intensities were performed using eleven High Purity Germanium (HPGe) clover detectors. In the current work, all the previously known bands have been significantly extended and five new bands have been added to the level scheme. The observed bands are interpreted within the cranked shell model (CSM), cranked Nilsson-Strutinsky-Bogoliubov (CNSB) formalism and Quasiparticle-plus-Triaxial-Rotor (QTR) model. Systematic comparison of bands with the neighbouring isotopes has also been made. Comparison of the models with experimental data shows good agreement. The configurations of some of the previously observed bands have been modified. Most importantly, the coupling of 2^+ γ band to the $11/2^+[615]$ neutron configuration is observed for the first time.

Keywords

AFRODITE
Fusion Evaporation
Gamma-ray spectroscopy
Gamma Bands
Angular Distribution ratios
Linear Polarization Anisotropy
Level Scheme.

Publications

1. **M. A. Sithole**, J. F. Sharpey-Schafer, E. A. Lawrie, S. N. T. Majola, A. Kardan, T. D. Bucher, J. J. Lawrie, L. Mdletshe, S. S. Ntshangase, A. A. Netshiya, P. Jones, L. Makhathini, K. L. Malatji, P. L. Masiteng, I. Ragnarsson, B. Maqabuka, J. Ndayishimye, O. Shirinda, B. R. Zikhali, S. Jongile, G. O'Neill, L. Msebi, P. M. Someketa, D. Kenfack, S. H. Mthembu, T. C. Khumalo, and M. V. Chisapi: *Low- and medium-spin negative-parity bands in the ^{187}Os nucleus.* **Phys. Rev. C 103, 024325 (2021)**

2. **M. A. Sithole**, E. A. Lawrie, L. Mdletshe, S. N. T. Majola, A. Kardan, T. D. Bucher, J. F. Sharpey-Schafer, J. J. Lawrie, S. S. Ntshangase, A. A. Avaa, R. A. Bark, M. V. Chisapi, P. Jones, S. Jongile, D. Kenfack, T. C. Khumalo, L. Makhathini, K. L. Malatji, B. Maqabuka, S. H. Mthembu, L. Msebi, A. A. Netshiya, G. O'Neill, O. Shirinda, P. M. Someketa, and B. R. Zikhali: *Structure of collective states built on the 11/2+ isomer in ^{187}Os: Quasiparticle-plus-triaxial-rotor model and interpretation as tilted-precession bands.* **Phys. Rev. C 104, 044326 (2021)**

3. **M. A. Sithole**, J. F. Sharpey Schafer, S. N. T. Majola, T. D. Bucher, T. R. S. Dinoko, S. S. Ntshangase, E. A. Lawrie, N. A. Khumalo, S. Jongile, L. Mdletshe, R. A. Bark, N. Erasmus, P. Jones, B. V. Kheswa, J. J. Lawrie, L. Makhathini, K. L. Malatji, B. Maqabuka, S. P. Noncolela, J. Ndayishimye, O. Shirinda, B. R. Zikhali and P. L. Masiteng : *New collective structures in the ^{163}Yb nucleus.* **Eur. Phys. J. A 55, 178 (2019)**

4. S. N. T. Majola, **M. A. Sithole**, L. Mdletshe, D. Hartley, J. Timár, B. M. Nyakó, J. M. Allmond, R. A. Bark, C. Beausang, L. Bianco, T. D. Bucher, S. P. Bvumbi, M. P. Carpenter, C. J. Chiara, N. Cooper, D. M. Cullen, D. Curien T. S. Dinoko, B. J. P. Gall, P. E. Garrett *et al.,* : *First candidates for γ vibrational bands built on the [505]11/2$^-$ neutron orbital in odd-A Dy isotopes.* **Phys. Rev. C 101, 044312 (2020).**

5. L. Mdletshe, X. Q. Yang, E. A. Lawrie, **M. A. Sithole**, S. N. T. Majola, S. S. Ntshangase, J. F. Sharpey Schafer, S. H. Mthembu, T. D. Bucher, L. Msebi, R. A. Bark, A. A. Avaa, M. V. Chisapi, P. Jones, S. Jongile, Z. P. Li, L. Makhathini, K. L. Malatji, Z. Shi, B. Y. Song, A. A. Netshiya, L. Wang, J. Xiang, and S. Q. Zhang: *New experimental information on the* 4_3^+ *band in* ^{186}*Os interpreted with the vibrational-phonon and triaxial-rotor models.* **(to be submitted to Phys. Rev. C).**

6. S. N. T. Majola, Z. Shi, B. Y. Song, Z. P. Li, S. Q. Zhang, R. A. Bark, J. F. Sharpey-Schafer, D. G. Aschman, S. P. Bvumbi, T. D. Bucher, D. M. Cullen, T. S. Dinoko, J. E. Easton, N. Erasmus, P. T. Greenlees, D. J. Hartley, J. Hirvonen, A. Korichi, U. Jakobsson, P. Jones, S. Jongile, R. Julin, S. Juutinen, S. Ketelhut, B. V. Kheswa, N. A. Khumalo, E. A. Lawrie, J. J. Lawrie, R. Lindsay, T. E. Madiba, L. Makhathini, S. M. Maliage, B. Maqabuka, K. L. Malatji, P. L. Masiteng, P. I. Mashita, L. Mdletshe, A. Minkova, L. Msebi, S. M. Mullins, J. Ndayishimye, D. Negi, A. Netshiya, R. Newman, S. S. Ntshangase, R. Ntshodu, B. M. Nyakó, P. Papka, P. Peura, P. Rahkila, L. L. Riedinger, M. A. Riley, D. G. Roux, P. Ruotsalainen, J. J. Saren, C. Scholey, O. Shirinda, **M. A. Sithole**, *et al.,* : *β and γ bands in $N = 88$, 90, and 92 isotones investigated with a five-dimensional collective Hamiltonian based on covariant density functional theory: Vibrations, shape coexistence, and superdeformation.* **Phys. Rev. C 100, 044324 (2019).**

7. S. N. T. Majola, R. A. Bark, L. Bianco, T. D. Bucher, S. P. Bvumbi, D. M. Cullen, P. E. Garrett, P. T. Greenlees, D. Hartley, J. Hirvonen, U. Jakobsson, P. M. Jones, R. Julin, S. Juutinen, S. Ketelhut, B. V. Kheswa, A. Korichi, E. A. Lawrie, P. L. Masiteng, B. Maqabuka, L. Mdletshe, A. Minkova, J. Ndayishimye, P. Nieminen, R. Newman, B. M. Nyakó, S. S. Ntshangase, P. Peura, P. Rahkila, L. L. Riedinger, M. Riley, D. Roux, P. Ruotsalainen, J. Saren, J. F. Sharpey-Schafer, C. Scholey, O. Shirinda, **M. A. Sithole**, J. Sorri, S. Stolze, J. Timár, J. Uusitalo and G. Zimba, : *Spectroscopy of low-spin states in* ^{157}*Dy: Search for evidence of enhanced octupole correlations.* **Phys. Rev. C 100, 034322 (2019).**

8. L. Mdletshe, S. S. Ntshangase, J. F. Sharpey-Schafer, S. N. T. Majola, T. R. S. Dinoko, N. A. Khumalo, E. A. Lawrie, R. A. Bark, T. D. Bucher, N. Erasmus, P. Jones, S. Jongile, B. V. Kheswa, J. J. Lawrie, L. Makhathini, K. L. Malatji, B. Maqabuka, J. Ndayishimye, S. P. Noncolela, O. Shirinda and **M. A. Sithole**: *Low-lying positive parity bands in* ^{162}*Yb.* **Eur. Phys. J. A, 54, 176 (2018).**

9. B. Ding, C. M. Petrache, S. Guo, E. A. Lawrie, I. Wakudyanaye, Z. H. Zhang, H. L. Wang, H. Y. Meng, D. Mengoni, Y. H. Qiang, J. G. Wang, C. Andreoiu, A. Astier, A. Avaa, T. B ack, R. A. Bark, D. Bazzacco, A. Boso, T. D. Bucher, B. Cederwall, M. V. Chisapi, H. L. Fan, F. Galtarossa, F. H. Garcia, A. Goasduff, G. Jaworski, P. Jones, I. Kuti, J. J. Lawrie, G. S. Li, R. Li, M. L. Liu, Z. Liu, B. Lomberg, B. F. Lv, T. Marchlewski, L. Mdletshe, L. Msebi, S. H. Mthembu, D. R. Napoli, A. Netshiya, M. F. Nkalanga, K. Ortner, F. Recchia, S. Riccetto, A. Rohilla, T. W. Seakamela, M. Siciliano, **M. A. Sithole**, D. Sohler, *et al.,* : *Signature splitting of the* $g_{7/2}[404]7/2^+$ *bands in* ^{131}Ba *and* ^{133}Ce. **(Accepted to Phys. Rev. C).**

Acknowledgements

First, I would like to thank God who gave me this precious life, and for placing an open door of success before me that no one can shut.

It is a genuine pleasure to express my deep sense of gratitude to all the people whose contributions made this project a success:

Mega thanks to Prof. E. A. Lawrie for her invaluable guidance, suggestions, support and being patient with me during this PhD project. Regardless of the number of students you have who are in their final year, you were always available when I needed your help. You were also there during data analysis, interpretation of the data, writing up of two papers we published this year and writing up of this thesis. Thank you also for the productive meeting we had with you. I can write a book about expertise and your generosity. I conclude by saying that you are a good teacher.

Many thanks to Dr. S. N. T. Majola for all the effort you put in this project. I know you had a lot of work to do on your side, to help undergraduate students, postgraduate students, however you were always available when I needed your help. To me you are a mentor, friend, motivator and a brother, Ndo livhuwa vho dokotela Majola.

Many thanks to Dr. T. D. Bucher, for her guidance, involvement and contributions in this thesis. You were always available and willing to help whenever I needed your help. You were the first person to read my raw writings, and your comments were always constructive. Also thank you for helping with the overleaf I used to write this thesis.

To Prof. J. F. Sharpey-Schafer, No words cannot express how grateful I am to find myself working with an extraordinary person like you. Your expertise in nuclear physics, generous guidance, understanding, and support are unmeasurable. It is always a pleasure to work with you. You taught me one valuable lesson, to always put family first above all. Thank you for being a mentor, a friend, a supervisor and most importantly a grandfather. There is never a dull moment when you are around. Thank you John.

To my best colleague "The young Prof" L. Mdletshe, thank you brother for walking this road with me. There's a lot I can say about you, however let me reserve that for my trip to KZN where we will slaughter a cow for a celebration of our great achievements. You are the best human being I have ever met in this life.

To the other members of our team, Sinegugu Mthembu, I. Wakudyanaye, and Lwazi, thank you for being a good team.

Thanks to Prof. A. Kardan for helping with the Cranked Nilsson-Strutinsky-Bogoliubov calculations.

Word of appreciation to Prof. J. J. Lawrie, for helping with the cranked shell model calculations.

Words of appreciation to Dr. Obed Shirinda and Dr. K. L. Malatji for proof reading this thesis.

Thanks to John Simpson and the STFC Daresbury Laboratory for supplying the ^{186}W targets.

Thanks to UWC physics department staff for their support in managing the NRF scholarship and for all the administration support.

Words of appreciation to the subatomic HoD and the AFRODITE staff for their support in providing me with the space and resources I required for my PhD studies.

Thanks to NRF for the financial support during my PhD studies.

To my colleagues at Eesteriver, thank you for the parties you always hosted at 15 Hadeda street, and the activities we have done, such as birthday celebrations, hiking, etc. This helped a lot to cool off my mind because research sometimes can be a nightmare.

To Sumbana Azwindini thank you for your support and for being a most kind sister.
To Luke Masia, thank you for the support you gave me during my undergraduate studies.

Last but not least, these acknowledgements would be incomplete if I don't thank my family. To me Family it's everything.

I would like to thank A. Ndou, mother of my daughter, for her patience, assistance, and encouragement throughout the duration of this project.

My sincere thanks also go to my daughter Precious, she is my heart in another body, the source of my strength, the sunshine in my dark days.

To My sister Fatima, thank you for the role you played of being a mother and a father to me, when our parents left us in this universe.

To My Uncle Joseph Makuhane, No words can express how grateful I am for the support you gave me. Thank you and may God bless you.

To the Sumbana Family and Faith Gospel Church thanks for your love and support.

If they ever tell my story, let them say that I walked with giants. Men rise and fall like the winter wheat, but these names will never die. Let them say I lived in the time of Abel Makuhane, John Sharpey-Schafer, Elena Lawrie, Siyabonga Majola, Daphney Bucher, and Linda Mdletshe.

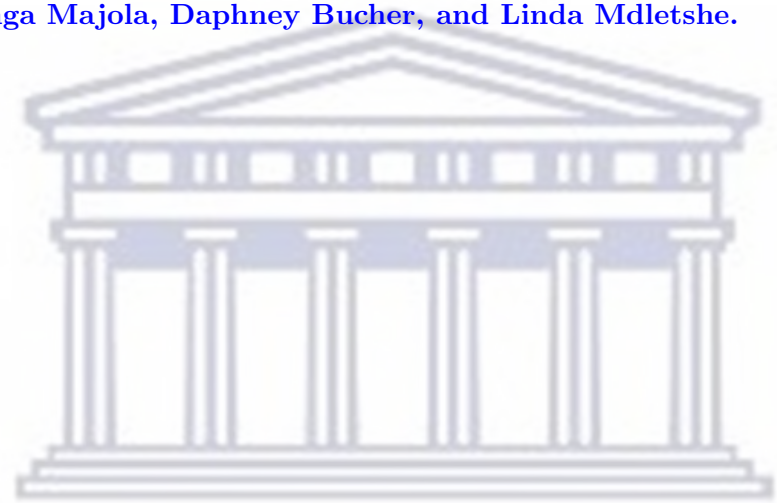

Contents

List of Figures

List of Tables

Chapter 1

Background study and scientific motivation

The shape of a nucleus is one of its most fundamental properties, and its exploration across the nuclear landscape provides insight into the mechanisms underlying how protons and neutrons are organized. The structural interpretation of nuclei between spherical (closed-shell) and deformed (open-shell) regions, has been strongly influenced by the Bohr model [16–18].

In effect, the shapes of most nuclei are not necessarily spherical, they may deviate away from spherical symmetry and develop permanent quadrupole deformation and triaxiality. Deformed nuclei can be characterised by the observation of many rotational bands. Over the past years, extensive investigations have been carried out on the spectroscopy of low-lying bands of these deformed nuclei, specifically in the deformed even-even nuclei ([19] and references therein).

Deformed axially-symmetric nuclei can generate angular momentum by collective rotation around an axis perpendicular to their symmetry axis. Such simple rotation in an even-even nucleus forms its ground-state rotational band. Nuclei with triaxial deformation (the three nuclear axes have different length) can rotate around all their three axes. Such simultaneous rotation in three dimensions (3D rotation) is more complex and in addition to the ground-state band generates some excited bands. To illustrate the nature of these bands, let us consider the rotational energy of a triaxial even-even nucleus,

$$E = \frac{\hbar^2}{2\Im_1}R_1^2 + \frac{\hbar^2}{2\Im_2}R_2^2 + \frac{\hbar^2}{2\Im_3}R_3^2, \tag{1.1}$$

where R_1, R_2, and R_3 are the rotational angular momenta along the three nuclear axes and $\Im_1$, $\Im_2$, and $\Im_3$ are the corresponding moments of inertia. The rotation about the axis with largest moment of inertia is favoured, because it needs least energy for a given angular momentum. The dependence of the moments of inertia on the triaxial deformation γ, is usually described using the empirically supported [20] irrotational-flow model,

$$\Im_k = \Im_0 sin^2(\gamma - k\frac{2\pi}{3}), \tag{1.2}$$

where k labels the three nuclear axes. The moment of inertia about the intermediate axis is largest.

The 3D rotation of triaxial even-even nuclei can be described schematically as follows, see Fig. 1.1. The ground-state band, which is the lowest-energy band, corresponds (approximately) to favoured rotations, where the rotational angular momentum increases along the intermediate axis. The 2^+ γ band, corresponds to dominant favoured rotation around the intermediate axis too, but also involves a unit of unfavoured rotation of approximately 2 $\hbar$ in the plane defined by the short and long nuclear axes, as shown in Fig. 1.1. Therefore, while the rotational angular momentum is still increasing along the intermediate axis the total rotational angular momentum $\vec{R}$ is tilted away from it. The unfavoured rotation may have different projections on the short and long nuclear axes, the total rotational angular momentum $\vec{R}$ precesses around the intermediate axis, as illustrated in the bottom part of Fig. 1.1. Unfavoured rotation of approximately 2 $\hbar$ and 4 $\hbar$ generates the 2^+ and 4^+ γ bands, respectively. The excitation energy of the γ band strongly depends on the triaxial deformation γ, for nuclei with increasing triaxiality, the excitation energy of the γ bands decreases.

While γ bands can be understood as generated by the precession of a deformed triaxial nucleus, they may also result from dynamical fluctuations, where the nuclear shape is axially symmetric on average, but vibrates with small amplitude with respect to the γ parameter. One-phonon γ vibration produces a 2^+ γ band, while 2-phonon γ vibration generates a 4^+ γ band. Gamma bands have been observed in many deformed nuclei and there is often a debate on whether these bands result from the rotation of a nucleus with rigid triaxial shape, or from the vibrations of a γ-soft nuclear shape. While some of the critical characteristics pertaining to the microscopic structure of γ bands remain elusive, it is worth noting that in the transitional rare-earth region [21–28] their excitation energy, runs parallel to that of their intrinsic configuration (the ground-state band in even-even nuclei), as a function of spin.

The stable even-even osmium (Os) nuclei show 2^+ γ bands at low excitation energy, suggesting that for these isotopes the γ degree of freedom is important [1–6]. The observed γ bands together with the 0_2^+ bands in the Os isotopes with $N = 106 - 116$

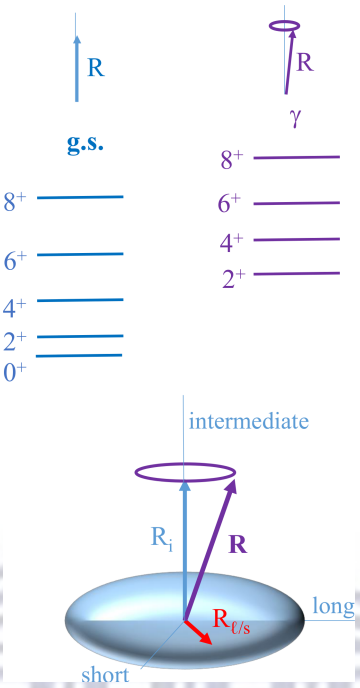

FIGURE 1.1: Sketch illustrating the precession of the rotational angular momentum $\vec{R}$ around the intermediate axis of a triaxially-deformed nucleus. For the ground-state band the total rotational angular momentum $\vec{R}$ is approximately aligned along the intermediate axis, however it is tilted away from this axis and precesses around it for the γ bands, because these bands involve unfavoured rotation in the plane defined by the short and long nuclear axes.

are illustrated in Fig. 1.2. From Fig. 1.2, one can note that as the neutron number N increases both the quadrupole deformation and the excitation energies of the γ band decrease steadily. The 2_2^+ state in ^{192}Os has the lowest excitation energy observed in the entire nuclear chart. In contrast the excitation energies of the excited 0_2^+ band remain almost constant for these isotopes varying in the range of E_{exc} = 1096- to 912-keV, see Fig. 1.2. In addition candidate two-phonon γ bands built on 4^+ states are also observed in these nuclei. These bands show a similar trend to the γ bands of decreasing excitation energy. The nature of these collective excitations has been a controversial subject for several decades and is still a matter of debate.

The odd-N nucleus can be a suitable candidate to study the nature of these collective excitations. It enables the collective structures in the core to be characterised by the manner in which the odd-N couples to the core excitations. In the osmium isotopes, the heaviest odd-N nucleus that can be reached by the use of the fusion-evaporation reaction is ^{187}Os.

In the last three decades, no detailed γ-ray spectroscopy has been carried out on the ^{187}Os nucleus [7] and its level scheme has not been well established, see Fig. 1.3. To date, known spectroscopic information about this nucleus is mainly available from the electron

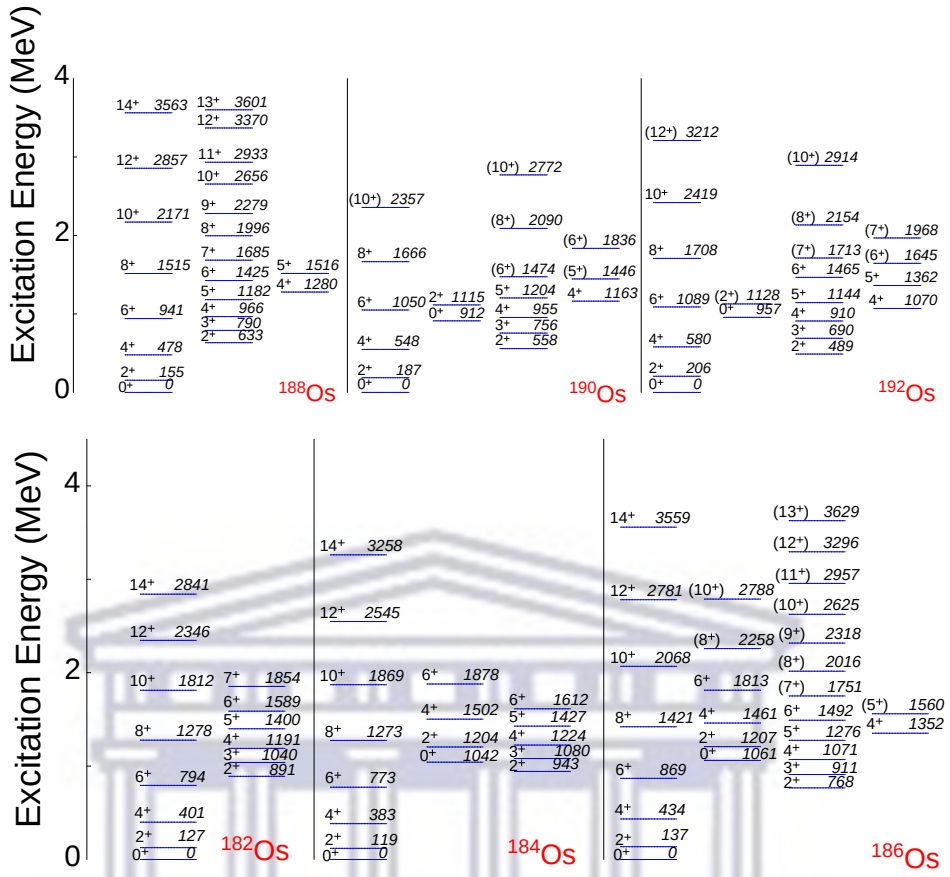

FIGURE 1.2: Summary of collective excitations in the even-even stable osmium isotopes showing the ground state and the excited 0_2^+, 2^+ and 4^+ rotational bands [1–6].

conversion, β decay, and transfer reaction studies [29–33]. Furthermore, there are also a few cases where this nucleus has been investigated through in-beam spectroscopy [7]. All these studies have made different contributions in the establishment of its decay scheme. In spite of this, rotational structures built on these low-lying excitations are yet to be fully established. More importantly, accurate determinations of multipolarities of the transitions are still needed in order to confidently determine the spins and parities of the excited states, which could subsequently allow one to understand the microscopic nature of the low-spin states and parities of rotational structures reported in the previous studies [7, 29–35].

The Nilsson diagram shown in Fig. 1.4, which represents the single-particle excitations as a function of the nuclear quadrupole deformation, was used to identify the approximate Fermi surface for ^{187}Os. The single-particle orbitals that lie close to the Fermi level are labelled in different colours, as indicated in Fig. 1.4. The quadrupole deformation ε_2 for ^{187}Os is 0.21 [7].

The main objective of this work is to study the spectroscopy of ^{187}Os in order to get an insight into the general behavior and microscopic nature of the low-lying single-particle

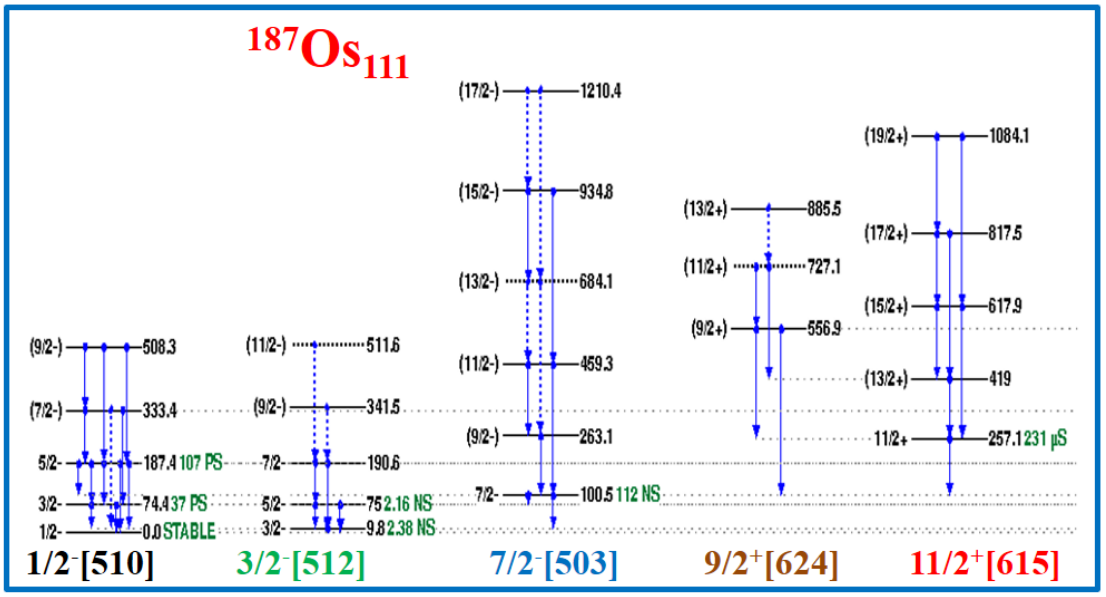

FIGURE 1.3: Decay scheme of ^{187}Os established by the previous in-beam work [7].

structures and expand on the experimental data reported in previous studies [7, 29–36]. Most importantly, we intend to investigate the coupling of the odd-nucleon in ^{187}Os to the collective excitations (particularly the γ band) of the ^{186}Os core. As shown in Fig. 1.2, the lowest collective excitations of the core that lie within the pairing gap ($\sim$ 2 MeV) are the γ bands. Therefore, we would expect to observe bands which are due to the coupling of the γ bands in the neighboring even-even cores with some valence nucleons.

The nature of the γ band in the Os isotopes is not fully understood, thus to shed some light on their structure we have to rely on nuclear models. There are different models that produce γ bands, based on different assumptions. There is a γ band which is caused by the rotation of a triaxial nucleus, like the one that is predicted by the triaxal rotor model [37]. There is also a γ band which comes from the assumption that the nucleus is γ soft and its shape oscillates between prolate and oblate deformation with equal probability throughout the whole range of the γ degree of freedom (model of Wilets and Jean) [38]. We also have the γ band that comes from the Bohr Hamiltonian [39]. This γ band is associated with a γ phonon vibration which means that the nuclear shape oscillates around an axially-symmetric deformation. In an odd-mass nucleus the γ band, (with whatever nature it has) would couple to the odd nucleon.

In an axially symmetric nucleus a single-particle orbital with angular momentum j can couple to the one-phonon quadrupole vibrations of the core, either with its angular momentum j parallel to the vibrational angular momentum to produce $K_> = (2+j)$, or it can be anti-parallel to give a rotational band with $K_< = |2 - j|$. In the transitional

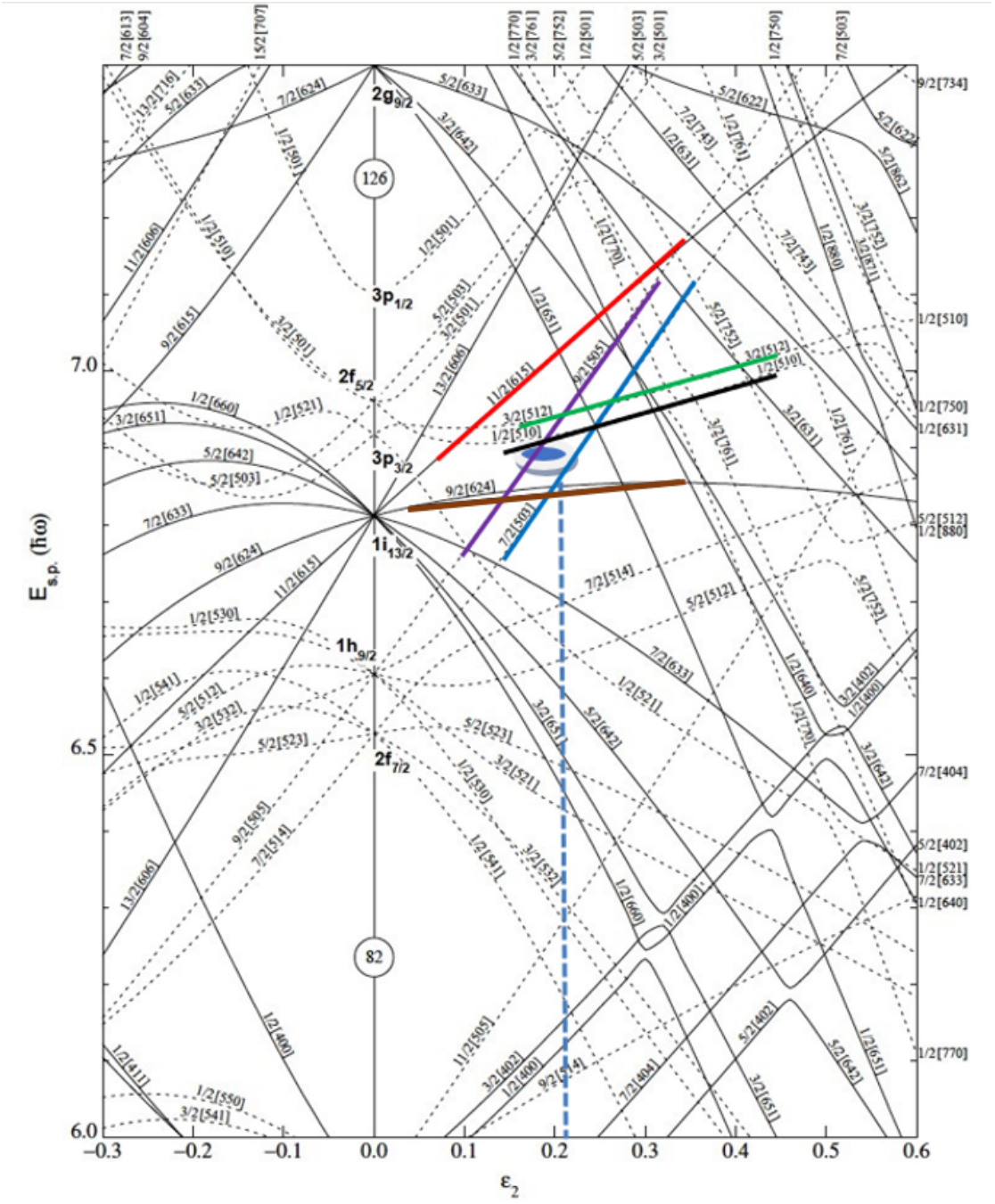

FIGURE 1.4: Nilsson diagram for neutrons ($82 \leq N \leq 126$) showing the single-particle energies as a function of the deformation parameter (ε_2). Orbitals that lie close to the Fermi surface are shown in different colours, modified from Ref. [8].

region there are few examples where both $K_>$ and $K_<$ couplings have been reported [40, 41]. On the other hand, if the γ band involves a large single-particle component from the orbital j a blocking effect can occur. For instance the blocking observed in ^{155}Gd for the coupling of the $h_{11/2}$ neutron and the 0_2^+ state of the core, suggested that this core state corresponds to a wavefunction with a considerable $\nu h_{11/2}$ contribution [42].

Chapter 2

Nuclear structure description using theoretical models

2.1 Introduction

The structural behavior of each atomic nucleus depends on the manner in which the nucleons interact within the nuclear medium. One of the challenges that nuclear physicists face, is to find a simple way to deduce the basic structure of a nuclear system directly from individual interactions of nucleons within the nucleus. It is still impossible to do that because the underlying interactions of neutrons and protons in the nuclear medium are still not entirely understood [43]. In a long search to address such limitations, nuclear physicists have persistently relied on the adoption of theoretical models. These models basically originate from mathematical formulations that have been used to describe well known physical systems, which share some intrinsic similarities with those of nuclei. A model that can predict most of the features that the nucleus exhibit can be regarded as a good nuclear model. However, up to date there is no single nuclear model that can fully describe the majority of features that nuclei exhibit. The reason being that every nuclear model was designed to meet some certain goals and has its own limitations. For instance the spherical shell model is a suitable model one can use to account for majority of features found in magic nuclei or nuclei near closed shell (shell gaps). While other models, such as the Nilsson model can be relevant to predict features observed for nuclei located far away from shell gaps. To date there are a varieties of nuclear models that one can use, but the use of any nuclear model depends on how it is related to the properties the nucleus of interest [44]. In the current chapter nuclear models such as

the Nilsson model, the cranked shell model (CSM), and the Quasiparticle-plus-Triaxial-Rotor model (QTR) will be reviewed. We will also briefly describe terminology relevant to our experimental results.

2.2 The liquid drop model

The liquid drop model was presented by Bohr in 1939 [45]. In this model he correlates the properties and the shape of the nucleus with that of the liquid drop. By doing so, he was successful in developing the first nuclear model which became instrumental in laying a foundation on the description of some of the fundamental nuclear phenomena such as nuclear fission, binding energy, the compound nucleus description of reactions, etc. Over the years, owing to the advancement of experimental techniques and apparatus, there are numerous experimental features that have been observed which could not be explained within the frame work of the liquid drop model. For example, the deviations in the experimental binding energies as a function of mass (due to shell effects) could not be accounted for. This led to the introduction of the shell model in nuclear physics.

2.3 The nuclear shell model

The nuclear shell model is a microscopic model which describes the motion of the individual nucleons. This model can be regarded as a tool used to explore some basic nuclear observables for the nuclei near the closed shells. The model describes the motions of the nucleons through single-particle excitations. This model forms the basis of other more complex nuclear models. The nuclear shell model was initially designed to account for some of the nuclear properties which were beyond the liquid drop model. This includes the discontinuous behaviour in the separation energies at specific values of neutrons and protons. These magic numbers of protons and neutrons are also known as shell gaps [46]. Experimentally, these discontinuities were observed to occur for the same proton (Z) and neutron (N) numbers namely, 2, 8, 20, 28, 50, 82, and $N = 126$.

For any shell theory to be regarded as a success it must be able to reproduce the shell closures at those occupation numbers. In an attempt to reproduce those shell closures the nuclear physicists developed a nuclear shell model with a harmonic oscillator potential. This model produces shell gaps with magic numbers of 2, 8, 20, 40, 70 and 112 [47]. While the first three magic numbers were in agreement with the experimental data, the consecutive higher ones were not. The Woods-Saxon and square-well potentials were also used to address this issue, but there was no success. To address this problem,

adjustments had to be made and l^2 and spin-orbit terms were added to the Spherical Harmonic Oscillator (SHO), see Fig. 2.1. This correction was introduced in 1949 by Mayer [48] following a suggestion by Fermi, and independently by Haxel, Jensen and Suess [49].

It is worth mentioning that the shell model is one of the most successful models in nuclear physics. It remains the standard of comparison for all other models and provides the justification and microscopic basis for the macroscopic collective models. This model was very successful in accounting for the observed nuclear properties such as spin-parity assignment of the states.

2.4 Nuclear surface deformations

The nuclear surface deformation can be described in the geometrical collective model first proposed by Bohr and Mottelson [18, 39] and detailed by Faessler and Greiner [50–55]. The nuclear surface can be described by a radius vector R which points from the origin to the surface. While different shapes are given by an expansion in spherical harmonics $Y(\theta, \phi)$,

$$R = R(\theta, \phi) = R_0 \left[1 + \sum_{\lambda=0}^{\infty} \sum_{\mu=-\lambda}^{\lambda} \alpha_{\lambda\mu} Y(\theta, \phi) \right], \tag{2.1}$$

where $R(\theta, \phi)$ represents the nuclear radius in the direction (θ, ϕ), R_0 is the radius of a spherical nucleus and $Y(\theta, \phi)$ are the spherical harmonics [37, 56].

The symbol λ represents the multipolarity of the shape, which also describes the dynamical properties of the nucleus. This parameter also describes the parity carried by the mode through the $\pi = (-1)^{\lambda}$ relation. The parameter μ is an integer taking its values from $-\lambda$ to $+\lambda$. The $\alpha_{\lambda\mu}$ parameter describes the changes of the nuclear volume with respect to the multiple order λ. For instance, $\lambda = 0$, 1, 2, 3 and 4 correspond to monopole, dipole, quadrupole, octupole and hexadecupole deformations respectively, see Fig. 2.2. The terms of interest are those with $\lambda = 2$ (quadrupole), and $\lambda = 3$ (octupole), respectively. Most of the models discussed in this work are based on quadrupole nuclear deformation. It is therefore in the author's best interest to discuss aspects related to this topic at relative length. The quadrupole deformations, have five coefficients for $\alpha_{2\mu}$. However, not all of them describe the shape of the nucleus. Three of them determine only the orientation of the nucleus in space and they correspond to the three Euler angles. These coefficients can be transformed to the body fixed system which coincides

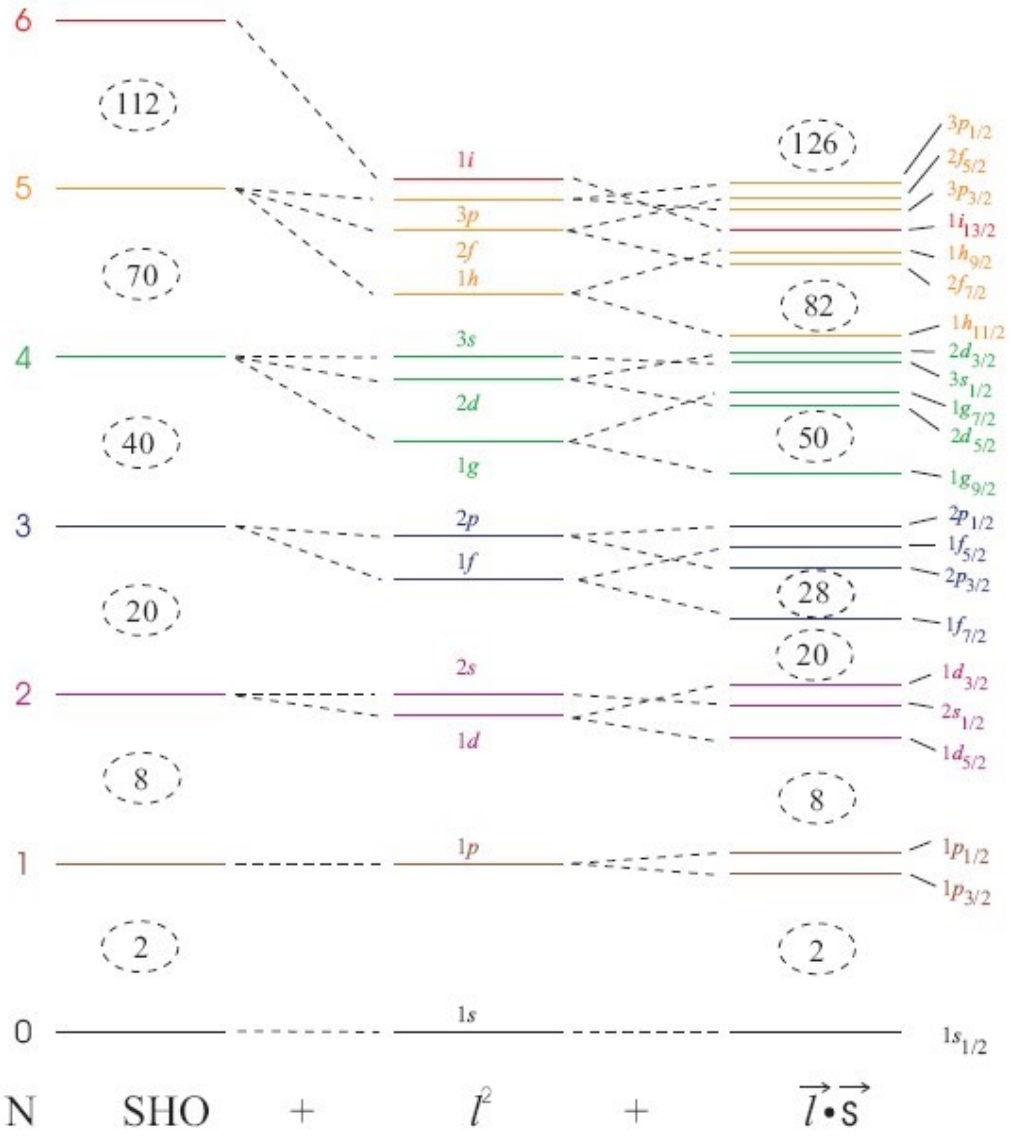

FIGURE 2.1: Schematic representation of energy levels in a modified oscillator potential. The levels that belong to the harmonic oscillator potential are on the left side of this diagram. These levels are split by the l^2 term to produce the second set of levels. The third set of levels which represent experimental observed shells shown on the right of this diagram are due to the spin-orbit ($\vec{l}.\vec{s}$) term [8].

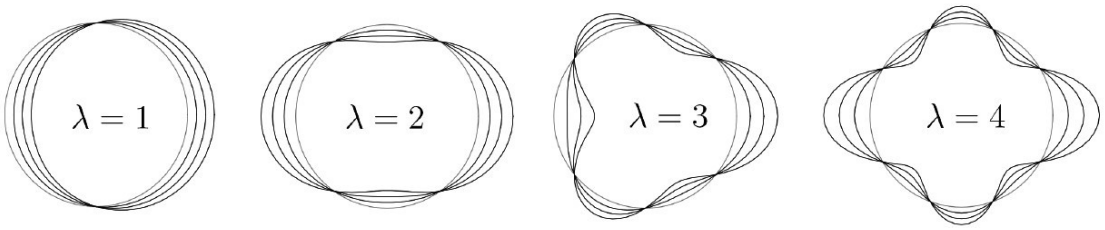

FIGURE 2.2: Schematic representation of dipole ($\lambda = 1$), quadrupole ($\lambda = 2$), octupole ($\lambda = 3$) and hexadecupole ($\lambda = 4$) deformations [8].

with the major axes of the nucleus by applying a suitable rotation. Then the five coefficients of $\alpha_{\lambda\mu}$ reduce to two real independent variables α_{20} and $\alpha_{22} = \alpha_{2-2}$. Since $\alpha_{21} = \alpha_{2-1} = 0$, which together with the three Euler angles $\Omega = (\Omega_1, \Omega_2, \Omega_3)$ give a complete description of the system. The coefficients α_{20} and α_{22} are related to the Hill-Wheeler [57] coordinates β, γ ($\beta > 0$) through the following equations:

$$\alpha_{20} = \beta_2 \cos\gamma, \tag{2.2}$$

$$\alpha_{22} = \frac{1}{\sqrt{2}}\beta_2 \sin\gamma. \tag{2.3}$$

The factor $\frac{1}{\sqrt{2}}$ was chosen such that

$$\sum_{\mu} |\alpha_{2\mu}|^2 = \alpha_{20}^2 + 2\alpha_{22}^2 = \beta_2^2. \tag{2.4}$$

The parameters β_2 and γ can be used to determine the nuclear shape. The parameter γ is a measure of deviation from axial asymmetry called the triaxiality parameter and β_2 represents the extent of quadrupole deformation. The increments of the three semi-axes in the body-fixed frame as a function of β_2 and γ are given by

$$\delta R_k(\theta, \phi) = \sqrt{\frac{5}{4\pi}}\beta_2 \cos(\gamma - \frac{2\pi}{3}k), \tag{2.5}$$

where k refers to the three principal axes of the nucleus [37, 44]. Further, when $\gamma = 0$ rad, the x = y while z is stretched that is z > x = y. This results into a nuclear deformation known as the prolate shape, which is axially symmetric. This shape is obtained when $\beta > 0$, $\gamma = 0°$. If γ is increased, the axial symmetry is lost because the x axis is elongated and y < x < z. At this step, the three axes are unequal and the surface shape is called triaxial. When γ reaches $\frac{\pi}{3}$, the x axis is equal to the z axis such that another axial symmetry occurs where y < x = z, and this results into the oblate

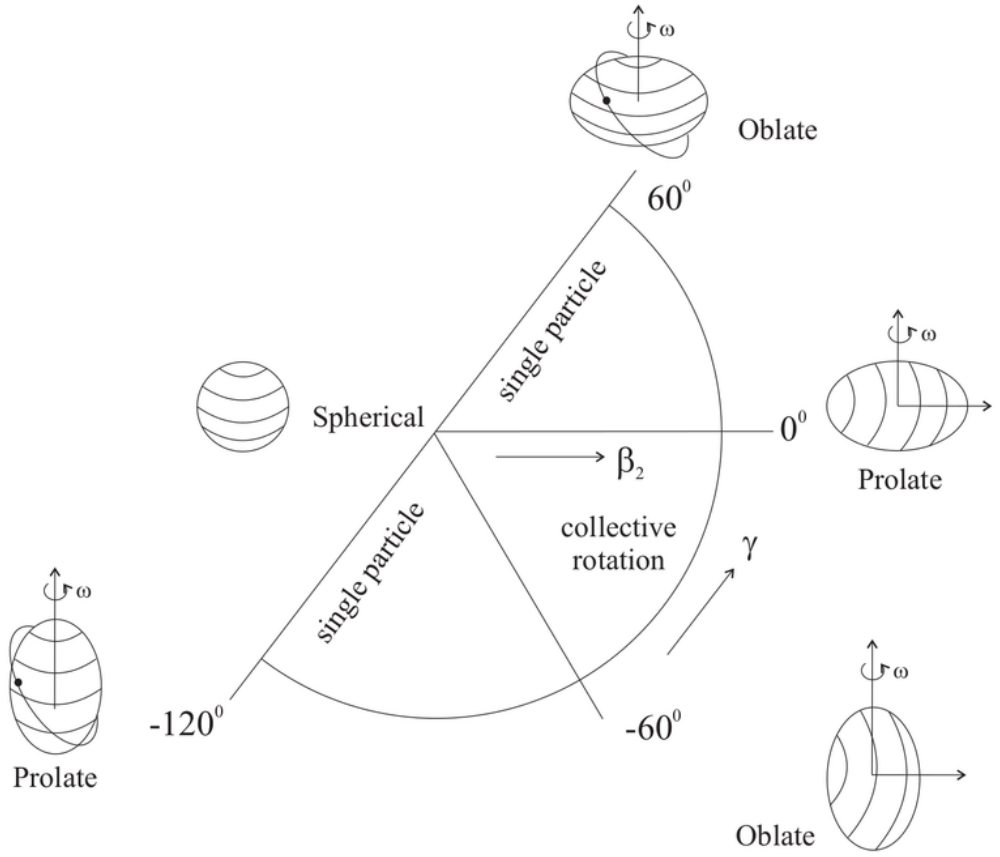

FIGURE 2.3: Schematic representation of the nuclear shape in β and γ plane with $\lambda = 2$ (quadrupole shapes). Figure taken from [9].

shape, see Fig 2.3. The latter has an hamburger shape and corresponds to $\beta > 0$, $\gamma = 60°$ condition.

The β_2 and γ parameterization is suitable when the nuclear potential is of Wood-Saxon type. This parameterization is used in Cranked Shell Model (CSM) and the Total Routhian Surface (TRS) calculations. Another parameterization is expressed in terms of the quadrupole deformation parameters ε_2 and γ, which is often referred to as Nilsson parameterization [12].

2.5 Nilsson model

Over the past decades, the spherical shell model has been used as a tool to describe nuclear properties across the nuclear chart. However with the growing amount of nuclear data experimental results showed that not all nuclei are spherical. Many nuclei that have

neutron and proton numbers far from shell closures are deformed. Obviously, in that case the assumption of a spherically symmetric potential fails. Instead of discarding the spherical shell model, a deformed potential was introduced, giving rise to a variety of deformed models. The most commonly used model of this kind is the Nilsson model, named after S.G. Nilsson, its principal designer [58]. The Nilsson model is one of the most successful nuclear models ever developed. It accounts for most of the observed features of single-particle levels in many deformed nuclei. To date, the Nilsson model is often the first model to be relied upon when one seeks to explain newly established experimental findings.

This model can be understood in terms of a deformation dependent Hamiltonian, commonly known as Nilsson Hamiltonian:

$$\vec{H} = -\frac{\hbar^2}{2M}\hat{\nabla}^2 + \frac{1}{2}M{\omega_0}^2 r^2 - M{\omega_0}^2 r^2 \epsilon_2 \frac{4}{3}\sqrt{\frac{\pi}{5}}Y_{20}(\theta,\phi) + C\vec{l}.\vec{s} + D\vec{l}^2, \tag{2.6}$$

where ω_0 represents the oscillator frequency, $r^2 = x^2 + y^2 + z^2$, $Y_{20}(\theta,\phi)$ is a spherical harmonic corresponding to a quadrupole deformed nucleus, $\vec{l}.\vec{s}$ is the spin-orbit interaction term of the spherical shell model and $\vec{l}^2$ is a term meant to bring down the orbitals with large $\vec{l}$. The constants of proportionality C and D can be determined by the adjustment to the experimental results. The details about the derivation of these terms are well described by R.F. Casten [47].

2.5.1 Nilsson diagrams

The Nilsson diagrams as shown in Figs. 2.4 and 2.5, describe the single-particle energy levels for a deformed nucleus. These diagrams can be easily understood when viewed in the light of two basic concepts. The first concept being the effect of the energy levels splitting and the second one is an interaction between two energy levels, called mixing. The splitting of the energy levels depends on the total angular momentum j and the nuclear deformation. This splitting is caused by the loss of sphericity of the nucleus, which results in the removal of the degeneracy of the magnetic substates. These states have identical single-particle angular momentum, j, but different projections on the symmetry axis. In fact individual angular momenta $(j_1, j_2, j_3...)$ are typically denoted with projections $(\Omega_1, \Omega_2, \Omega_3...)$ and the total angular momentum projection $(\Omega_1+\Omega_2+...)$ is denoted by K. The energy levels are altered by the mixing of two levels with the same quantum numbers K and parity π. The crossing of such levels are forbidden by the Pauli exclusion principle. As they approach each other in energy they mix strongly, and the states repel. This repulsion refers to the apparent bending of states observed in the

Nilsson diagrams. This energy level description accounts for the ground state and the first few excited states in the nuclei, where the effects of the nuclear rotation on the states are negligible. In the case of fast rotation of the core, the effects of the nuclear rotation on the states are no longer negligible and the Nilsson single-particle energies need correction [8]. These diagrams are very relevant to the present work, as they are used for the assignment of configurations to the low-energy single-particle states in ^{187}Os nucleus.

2.6 Cranked shell model

The cranked shell model can be considered as a version of the Nilsson model but applied to rotating nuclei. The model was first proposed by Inglis in 1954-1956 [59, 60], and was further developed by Bengtsson and Frauendorf in 1979 [61, 62]. This model consists of a Nilsson potential in a rotating frame of reference. In other words we take the single-particle energies as described by the Nilsson model, rotate the whole nucleus and subsequently observe how the energies of each one of these single-particle levels changes as a function of the rotational frequency. The difference between the stationary Nilsson potential and the rotating one is the Coriolis term that acts in addition to the nuclear force. The Coriolis term is proportional to the rotational frequency and to the projection of the total angular momentum on the rotational axis. This model is the most successful model when additional rotational forces influence the motion of the the nucleons. In essence, in this model, the time-dependant Schrödinger equation (see equation 2.7) is transformed from the space-fixed coordinate axes to the axes fixed with the rotating body,

$$i\hbar\frac{\partial\psi_{lab}}{\partial t} = h_{lab}\psi_{lab}, \tag{2.7}$$

where h_{lab} and ψ_{lab} represent the single-particle Hamiltonian and the wavefunction of the system in the laboratory frame, respectively.

In this model, high-spin states in nuclei are generated by the Hamiltonian in the intrinsic, rotating system:

$$h^{\omega} = h_{lab} - \hbar\omega i_x, \tag{2.8}$$

where h_{lab} is the nuclear Hamiltonian in the laboratory system, the second term $\hbar\omega i_x$ classically accounts for the nuclear rotational effects, such as the Coriolis and centrifugal forces in the rotating system. The energy eigenvalues of equation 2.8 are called Routhians. A Lagrange multiplier that is normally interpreted as the rotational frequency is

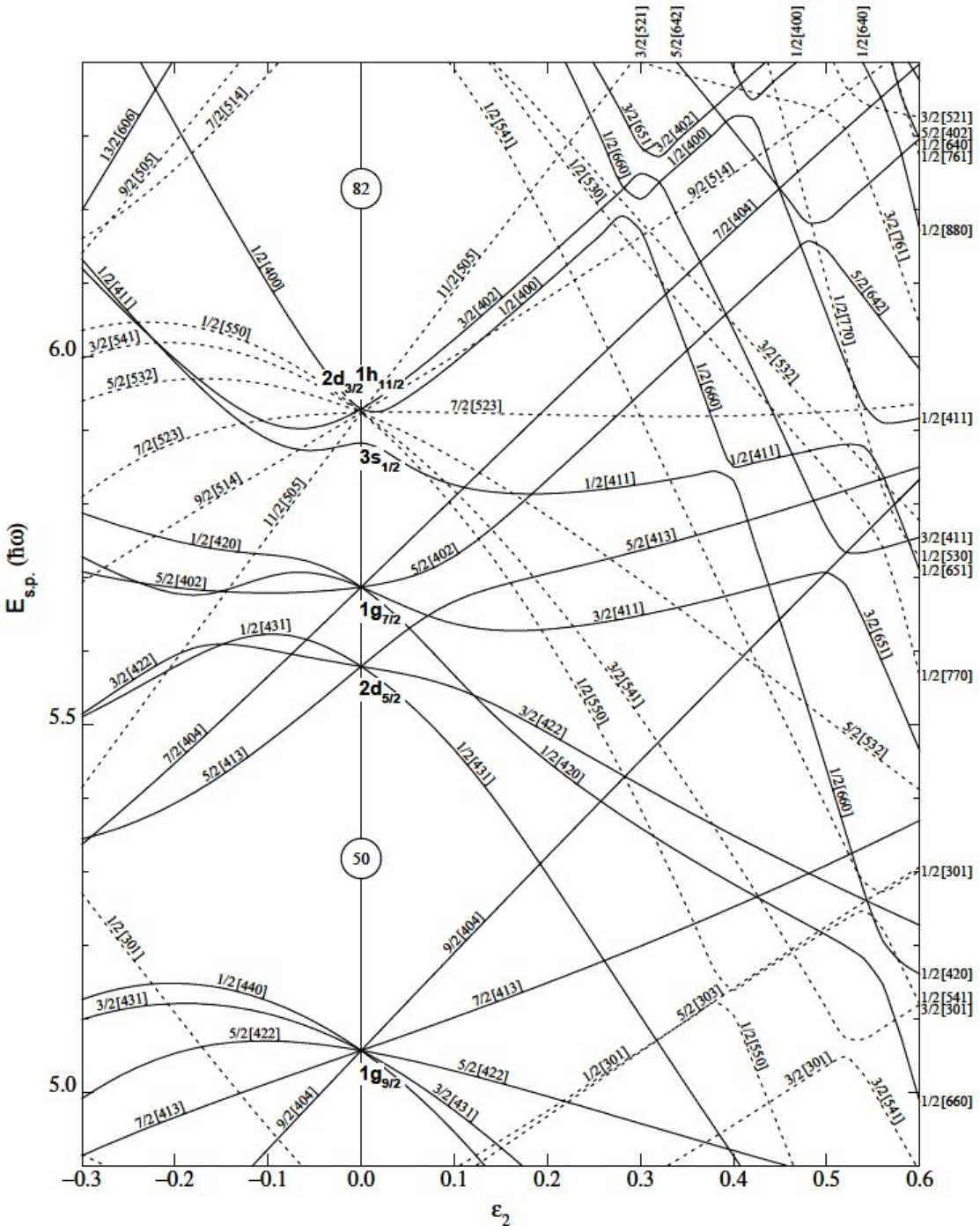

FIGURE 2.4: Nilsson diagram for protons ($50 \leq Z \leq 82$) as a function of ε_2 in a prolate ($\varepsilon_2 > 0$) and oblate ($\varepsilon_2 < 0$) nucleus. The quantum numbers $\Omega[Nn_z\Lambda]$ label the states and N is a major harmonic oscillator shell quantum number, n_z is the number of nodes in the wavefunction in the z direction and Λ is the component of angular momentum along the symmetry axis or z - axis. The projection of $j = l + s$ onto the z-axis is given by $\Omega = \Lambda + \Sigma$. Solid and dashed lines indicate the states with positive and negative parity, respectively [10, 11].

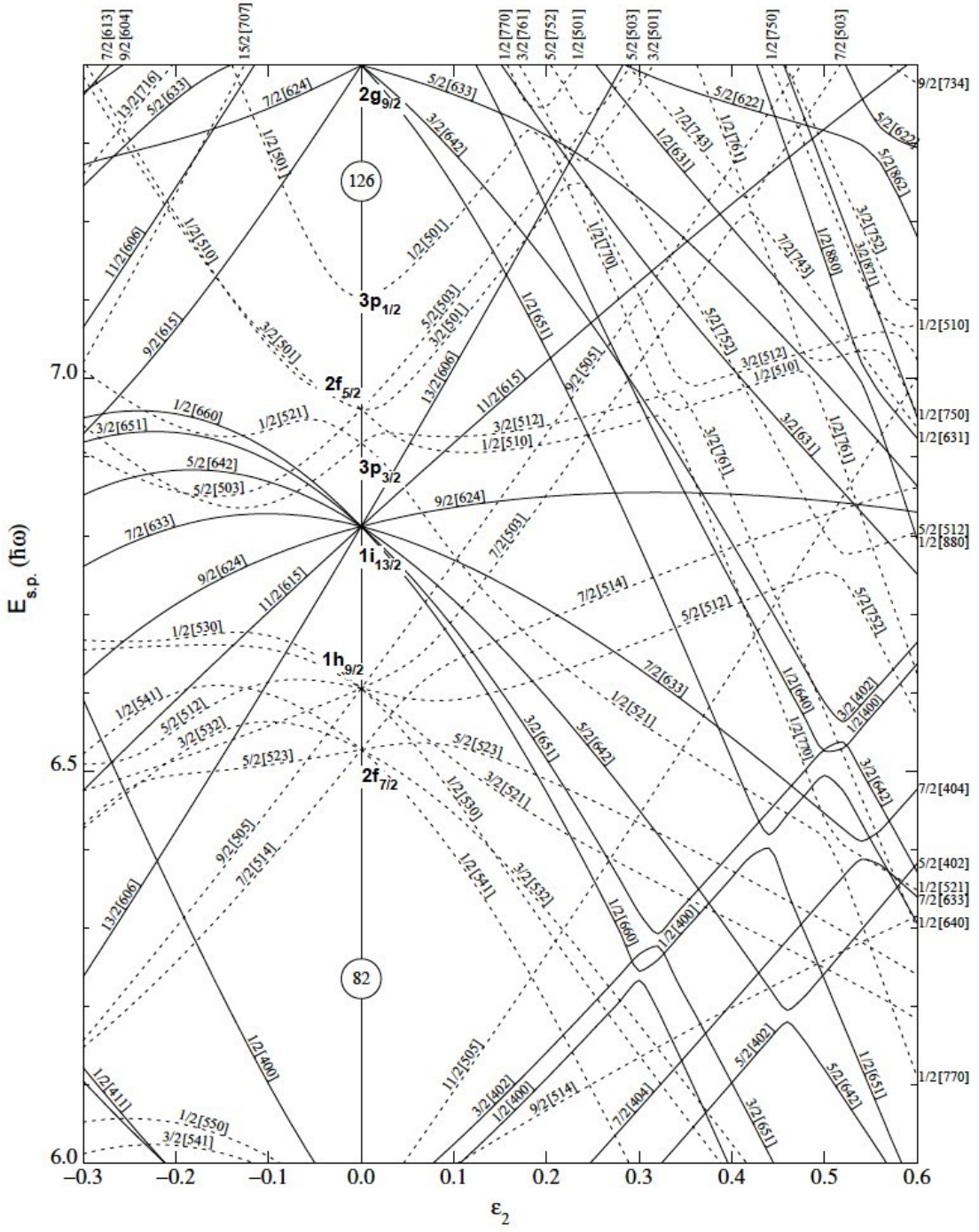

FIGURE 2.5: Nilsson diagram for neutrons ($82 \leq N \leq 126$) as a function of ε_2 in a prolate ($\varepsilon_2 > 0$) and oblate ($\varepsilon_2 < 0$) nucleus. The quantum numbers $\Omega[Nn_z\Lambda]$ label the states and N is a major harmonic oscillator shell quantum number, n_z is the number of nodes in the wavefunction in the z direction and Λ is the component of angular momentum along the symmetry axis or z - axis. The projection of $j = l + s$ onto the z-axis is given by $\Omega = \Lambda + \Sigma$. Solid and dashed lines indicate the states with positive and negative parity, respectively [10, 11].

given by ω. Further, i_x represents the projection of the single-particle angular momentum onto the rotational axis. In addition, if all of the independent single-particles in the system are taken into account, the cranking Hamiltonian takes the following form:

$$H^{\omega} = H_{lab} - \hbar\omega I_x. \tag{2.9}$$

The first term H_{lab} represents the sum of all single-particle Hamiltonians in the laboratory frame, while I_x denotes the total aligned angular momentum over all occupied orbitals. The details about this model are well derived and explained in Refs. [61–63].

2.6.1 Alignments

From theoretical point of view, the alignment represents the slope of the Routhian when it is plotted as a function of the rotational frequency. Each Routhain has a different slope which implies that it corresponds to a different single-particle alignment. The experimental data does not tell us directly what is the alignment, in other words what is the projection of the single-particle angular momentum along the rotational axis. The question then is how to extract the information about alignment of the valence nucleons from the experimental data. First of all we have to look at the rotational band and use equation 2.10 to assign rotational frequency for each level,

$$\hbar\omega(I) = \frac{E(I+1) - E(I-1)}{I_x(I+1) - I_x(I-1)}, \tag{2.10}$$

where $\hbar\omega(I)$ is the rotational frequency based on the excitation energy of the states with spins $I+1$ and $I-1$, respectively. I_x denotes the projection of the total angular momentum along the rotational axis, see equation 2.11,

$$I_x = \sqrt{(I+1/2)^2 - K^2}, \tag{2.11}$$

where K denotes the projection of the angular momentum onto the symmetry axis. It may be obtained from the band-head spin, if K is conserved or it may also be taken from the Nilsson quantum numbers $\Omega[Nn_z\Lambda]$ of the quasiparticle configuration assigned to the band. I is the total angular momentum of the state and it has an intrinsic single-particle and rotational angular momenta components. In order to find out how much is the single particle component, i.e. the alignment, we have to subtract the angular momentum which is due to rotation (I_{xr}) from the aligned angular momentum I_x [62].

2.6.2 Routhians

Routhians are single-particle energies in a rotating frame and they depend on the rotational frequency. At zero rotational frequency these Routhians correspond to the single-particle orbitals calculated by the Nilsson model. If the rotational frequency increases these single-particle orbitals get modified. For the single-particle angular momentum in the same direction as the rotation the Coriolis term becomes large and because this term comes with negative sign, it reduces the energy. For the Routhians that appear flat as a function of the rotational frequency, the single-particle angular momentum is actually perpendicular to the rotation and the Coriolis term is approximately zero.

The experimental data delivers the energy $E(I)$ of the states of the band as a function of the angular momentum I. The experimental data should be transformed into the rotating frame as:

$$E^{\omega} = \frac{1}{2}[E(I+1) + E(I-1)] - \hbar\omega(I)I_x(I). \tag{2.12}$$

For comparison purpose, it is advisable to first calculate the experimental energies E^{ω} and the aligned angular momentum I_x relative to a reference rotational band as:

$$i^{\omega} = I_x^{\omega} - I_{xref}^{\omega}, \tag{2.13}$$

$$e^{\omega} = E_x^{\omega} - E_{xref}^{\omega}. \tag{2.14}$$

In order to determine the functions e^{ω} and i^{ω} an appropriate choice of reference is required. The choice of reference plays a key role in the analysis of the rotational spectra. The ground-state rotational band or the first excited band are often used as a reference.

2.7 Cranked Nilsson-Strutinsky-Bogoliubov (CNSB) model

The cranked shell model has proved to be a successful tool to describe the rotational bands in most axially symmetric nuclei [62]. However, experimental results have shown that some nuclei appear to have triaxial ground-state deformations as concluded by the analysis of nuclear masses [64]. For a triaxial nucleus, the possibility of rotation around any of the three principal axes is high. But before considering simultaneous

rotation around all three nuclear axes, it is useful to examine the features of single-axis rotation for a nucleus with triaxial shape. The general features of the rotating nuclei can be understood in the Nilsson-Strutinsky model. In this model the rotating nucleus is described as a rotating liquid drop where shell effects are also included [65]. The modified version of this model that includes pairing correlations is known as the Cranked Nilsson-Strutinsky-Bogoliubov model.

The CNSB model approach is based on the ultimate Cranker formalism [66]. This model includes the pairing, unlike in the Cranked Nilsson-Strutinsky (CNS) formalism where the pairing is neglected. Usually at high spin where pairing is negligible, nuclear rotational bands will have a moment of inertia which is close to that of a rigid body [67]. Therefore, a large moment of inertia indicates a large deformation, which means that it becomes energetically cheaper to increase the spin by rotation. The fact that pairing is negligible in the CNS approach makes it possible to specify configurations in a detailed way, based on the occupation of orbitals which have their main amplitudes in specific j-shells or groups of j-shells. However, with the CNSB model it is very difficult to specify configurations in a detailed manner. The only good quantum numbers in the CNSB formalism are parity π and signature α for protons and neutrons. The total energy for the correct number of particles with pairing included (particle number projections) is minimized not only in the deformation space but also in a mesh in the pairing parameters, Fermi energy λ and pairing gap Δ. More details about this model are given in Refs. [68, 69]. This model was used to interpret the results for ^{187}Os.

2.8 Collective motions

A very interesting method to describe nuclear collective motion starts from a multipole expansion of the fluctuations in the nuclear density distribution around a spherical or deformed equilibrium shape. The collective motions are divided into two main categories: rotational, which gives rise to characteristic band structures and vibrational, which consist of small oscillations around a spherical or deformed shape. These collective motions will be discussed in the current chapter.

2.8.1 Collective rotations

Nuclei can deviate from spherical symmetry and develop permanent deformation. Such nuclei are known as deformed nuclei. Deformed nuclei can exhibit collective rotations about an axis perpendicular to the nuclear symmetry axis [70]. The shape of the rotating

nucleus is determined by the nucleons, which are in rapid internal motion within the nuclear potential. Nuclear rotation can generate excited states with excitation energies that are predicted via equation 2.15,

$$E_{Rot}(J) = \frac{\hbar^2}{2\Im}[J(J+1)], \tag{2.15}$$

where $\Im$ is the moment of inertia of the deformed nucleus. By adding rotational energy to the system, thus increasing the quantum number J, excited states are generated and form a sequence known as a rotational band [46]. All states belonging to the same rotational band maintain the same value for K. The energies of these excited states show that the energy ratio for a symmetric top rotor would be approximated by $E_{4_1^+}/E_{2_1^+} = 3.33$. This ratio is significantly different for a vibrating spherical nucleus [46], and has become one of the characteristics of identifying deformed nuclei. When nuclear rotational motion is superimposed on an intrinsic excitation, characterized by the projection K, the total angular momentum can take on values $J = K$, $K+1$, $K+2$, ..., except when $K = 0$, in which cases with only even spins, J are allowed. Thus, for the rotational energies, relative to the base energy of the intrinsic excitation, equation 2.15 becomes

$$E_{Rot}(J) = \frac{\hbar^2}{2\Im}[J(J+1) - K(K+1)]. \tag{2.16}$$

The energy expressions, equations 2.15 and 2.16, are quite accurate to validate the rotational concept for low spin states in deformed nuclei.

2.9 Collective vibrations

Collective motion of the nucleons can cause deformed nuclei to vibrate while rotating and thus generate angular momentum. The modes of vibrations that we will discuss in this chapter are the quadrupole vibrations. The quadrupole vibrations carry two units of angular momentum, and can be classified as $K = 0$ and $K = 2$. The former are known as β vibrations, and correspond to $K = 0$. The latter, with $K = 2$, are called γ vibrations and represent a time dependent variation along the axial symmetry [46, 47]. These names come from the fact that the β vibration corresponds to fluctuations in the quadrupole deformation β, while the γ vibration corresponds to oscillations in γ [47]. These two vibrational modes appear in essentially all deformed nuclei, usually around 1 MeV for $A > 100$ [47]. In the transitional region, β and γ bands are usually observed between 500-1500 keV [22, 23].

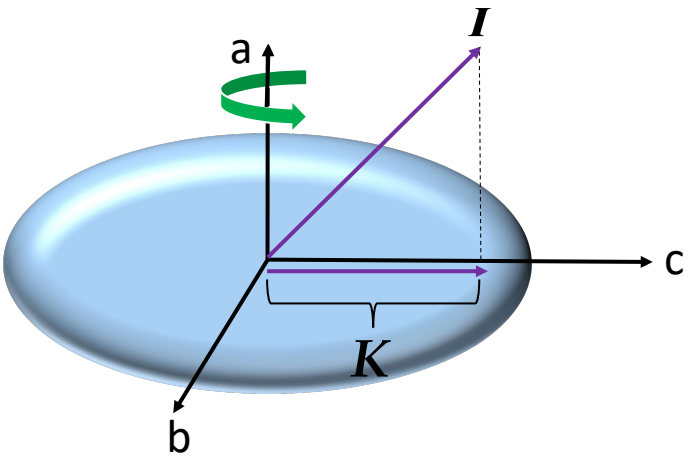

FIGURE 2.6: A prolate deformed nucleus with axial symmetry showing the rotation axis (a), the nuclear symmetry axis (c), the total angular momentum I, and projection K onto c.

The nature of the first-excited $K^{\pi} = 0^{+}$ states in even-even nuclei has been studied extensively over the last few decades [71–82]. However, despite this the microscopic identity of these states remains difficult to describe, more especially for nuclei located in the transitional rare-earth region. There are three ways of which the $K^{\pi} = 0^{+}$ bands can be generated. The first one is shape coexistence, the second is the pairing isomers and the third is β vibration.

The γ vibration is more difficult to visualize. It may be viewed as an alternate "squashing" of an American football in two directions 90° to the symmetry axis or alternating along (a) and (b) axes (see Fig. 2.6), and hence this mode carries angular momentum that is aligned with the symmetry axis, $K = 2$. This mode corresponds to a rotational band with $I^{\pi} = 2^{+}, 3^{+}, 4^{+}, \ldots$. There are two other (often used) descriptions of the γ band, related to γ soft and γ rigid nuclear shape. If we say that the nucleus is γ soft we mean that it vibrates in the γ direction. In terms of the Wilets-Jean model [38] the shape of such nucleus oscillates between prolate and oblate deformation keeping the same quadrupole deformation. Alternatively the γ band can result from the rotation of a nucleus with rigid triaxial shape.

2.10 Quasiparticle-plus-Triaxial-Rotor model

The QTR model which uses a modified oscillator potential was used to perform the calculations for the bands in ^{187}Os. In these calculations we used the GAMPN, ASYRMO

and PROBMO codes of P. B. Semmes and I. Ragnarsson [83]. These programs were ran one after the other in the sequence as listed above. The GAMPN program is used to calculate the single-particle energies and wavefunctions for the odd nucleon, in our case the odd neutron. The parameters used in the current work are the nuclear deformation parameters: quadrupole deformation $\varepsilon_2 = 0.21$, hexadecopole deformation $\varepsilon_4 = 0$, the triaxiality deformation $\gamma = 20°$, mass number A = 187 and atomic number Z = 76, also the Nilsson strength parameters given in Ref. [84]. For asymmetric nuclear shapes the single-particle state is made up of a mixture of Nilsson states with same parity and different occupation probabilities whereas for axially symmetric nuclear shapes and large deformation the single-particle state is a pure Nilsson state. From the single-particle states generated by the GAMPN code a set of 7 positive-parity orbitals lying close to the Fermi level were selected and later used for the construction of the particle-plus-rotor states. The output of the single-particle states with positive parity near the Fermi level and generated by the GAMPN program in the current work are listed in the Table 5.1.

The ASYMO code couples the single-particle states generated by the GAMPN code with the rotating triaxial core and calculates excitation energies and wavefunctions for the states of the rotational bands. The PROBMO code calculates the electromagnetic matrix elements, both diagonal and off-diagonal, from the eigenvectors of the particle-plus-rotor Hamiltonian generated by ASYMO code. The diagonal matrix elements are shown as the static moments (electric quadrupole moment Q_s and the magnetic dipole moment μ), in units of e-barn (eb) and nuclear magnetons (μ_N) respectively. The electric quadrupole moment Q_s is the spectroscopic moment, which can be directly observed in the experiments, while the intrinsic moment Q_0 rejects the nuclear deformation. The off-diagonal matrix elements are displayed as $B(E2)s$ and $B(M1)s$ (in units of e^2b^2 and μ_N^2 respectively), and as γ-ray partial transition rates $T(E2)$ and $T(M1)$. Furthermore, the mixed $E2/M1$ transitions can be calculated and the mixing ratio $\delta^2 = \frac{T(E2)}{T(M1)}$ is listed. However our experimental setup did not have the geometry to determine precisely these mixing ratios. The detailed interpretation of the current results using these calculations are given in chapter 5.

Chapter 3

Experimental methods

In this work, the ^{186}W(^{4}He, 3n)^{187}Os reaction, at a beam energy of 37 MeV, was used to study the nuclear structure of ^{187}Os nucleus. A stack of four ^{186}W targets mounted on thin carbon foils with a total thickness of 400 μg/cm^2 was used in this experiment. The ^{4}He beam was delivered to the stationary target by the K = 200 separated sector cyclotron at iThemba LABS. The AFRican Omnipurpose Detector for Innovative Techniques and Experiments (AFRODITE) γ-ray spectrometer array [85] was employed to detect resulting γ-γ coincidences from the excited states of ^{187}Os. The array consisted of 11 High-Purity Germanium (HPGe) clover detectors in bismuth germanate ($Bi_4Ge_3O_{12}$), abbreviated as BGO shields, 4 Low Energy Photon Spectrometer (LEPS) and 8 Lanthanum Bromide ($LaBr_3$) detectors.

3.1 Nuclear reaction selection

The success of a particular nuclear structure experiment depends on various parameters such as selecting a reaction which gives highest yield for the nucleus of interest and smaller yield for contaminants. The selection of the nuclear reaction depends on the type of physics one intends to study. If it is the study of high spins, one will use the heavy-ion beam such as ^{20}Ne, because it brings in a large amount of angular momentum. However, for the study of low spins states a reaction with a lighter beam, such as ^{4}He, which brings in less angular momentum will be more appropriate. For a given target and projectile the beam energy (that will give an optimal yield and grazing angular momentum) was determined using the Projected Angular Momentum Coupled Evaporation (PACE4) [86, 87] simulation code. This code uses a Monte Carlo simulation to predict cross-section and angular momentum distribution for the reaction of interest. Fig. 3.1 shows the PACE4 calculations performed in the current work. As shown in Fig. 3.1, the

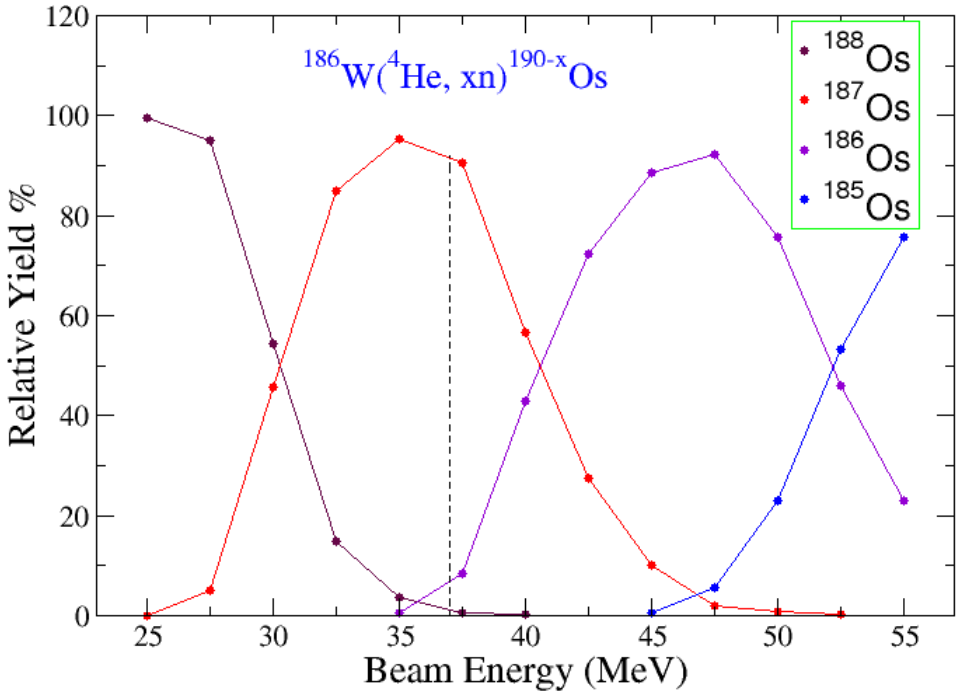

FIGURE 3.1: PACE4 output for the ^{187}Os experiment: beam energy vs cross-section.

beam energy of 37 MeV is predicted to produce the highest yield for the nucleus of interest which is ^{187}Os. For a fusion evaporation reaction to occur the energy of the beam has to be large enough to overcome the Coulomb barrier. However, increasing the beam energy too much has an undesired side effect of increasing the excitation energy of the compound nucleus, which causes more particles to be evaporated resulting in more contaminants.

3.1.1 Heavy-ion fusion evaporation reaction

In the study of high-spin states one searches for reactions which transfer to the compound nucleus the highest possible angular momentum at the largest possible cross-section. It was found that heavy-ion fusion evaporation reactions [88, 89] provide the most efficient way to achieve this. Certain conditions have to be taken into account to make sure that the desired nucleus is produced. These include the target-beam combination and the energy of the incoming beam projectile. In the current work, the ^{186}W target is bombarded by a ^{4}He beam which has sufficient energy to overcome the Coulomb barrier, and resulted in the formation of unstable excited ^{190}Os compound nucleus, see Fig. 3.2.

The Coulomb barrier that must be overcome in order for the strong nuclear interaction to take place is given by:

$$V_{CB}(R) = \frac{1}{4\pi\epsilon_0}\frac{Z_b Z_t e^2}{R}, \tag{3.1}$$

where Z_b and Z_t represent the beam and target atomic numbers, respectively, R is the distance between the beam and target nuclei, e is the charge of an electron and ϵ_0 is the permittivity of free space. For the rare-earth region the interaction radius is best represented by [90]:

$$R = [1.36(A_b^{1/3} + A_t^{1/3}) + 0.5]fm, \tag{3.2}$$

where A_b and A_t refer to a beam and a target mass number, respectively. The excited compound nucleus releases its excess energy and gain stability through particle emission. At this stage the neutron evaporation dominates the early decaying process of the ^{190}Os compound nucleus. Three neutrons were emitted from ^{190}Os compound nucleus and resulted in the residual nucleus ^{187}Os. The emitted neutrons lower the excitation energy by each taking away 8-10 MeV, plus kinetic energy between 1-2 MeV. In spite of this, they carry away little angular momentum. The nucleus continues to cool off by the emission of statistical γ-rays which are dipoles in nature. These γ-rays carry off little angular momentum and remove excitation energy. Through these series of emissions the yrast line is eventually reached. The levels near the yrast line are connected to each other mainly by stretched $E2$ transitions which take 2 $\hbar$ of angular momentum and eventually lead to the nuclear ground state.

3.1.2 Detecting γ radiation

A γ-ray can be classified as a form of electromagnetic radiation (each quantum of which is called a photon), that carry very high energy. Gamma-rays are highly penetrative across various kinds of materials. Their wavelengths are very short such that they can pass through the detection media without interacting with any of its material particles. The interaction of this type of radiation with the detector material depends on the electron density of the material. In semiconductor detectors information is extracted from the electron-hole pairs formed when the radiation interacts with the detector material. The electron-hole pairs are known as charge carriers. The detection signal is formed by collecting these charge carriers.

There are three key processes by which a γ-ray can interact with matter, namely, the photoelectric effect, Compton scattering, and pair production. For a germanium (Ge)

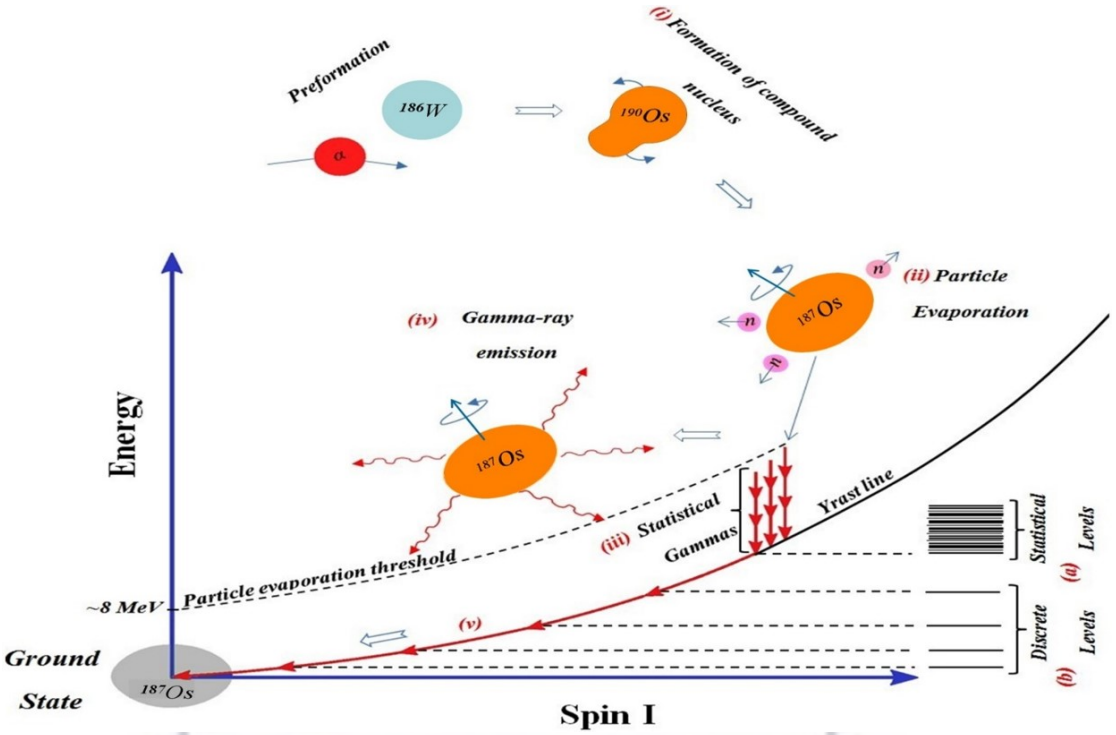

FIGURE 3.2: The fusion evaporation reaction schematic diagram illustrating how the compound nucleus de-excites to the ground state.

material, the photoelectric process is dominant at energies less than 0.1 MeV, as shown in Fig. 3.3. The probability of the photoelectric effect increases as the atomic number Z increases and decreases rapidly with increasing γ-ray energy. After 0.1 MeV, Compton scattering is the dominant process, see Fig. 3.3. The Compton scattering is almost independent of the atomic number, but it depends strongly on the electron density of the material [91]. This process affects the quality of the spectra obtained. The Compton scattered events usually contribute to an unwanted background in the detector spectra, known as a Compton Continuum, due to scattered photons not losing their energy in the detector. As can be seen in Fig. 3.4, the Compton continuum negatively affects the quality of the γ-rays spectrum. The background can be reduced by surrounding the detector with Compton suppression shields that are made of materials with good scintillation properties and a high atomic number Z such as BGO. The (Bismuth Germanate) suppression shield is then run in anti-coincidence with the central detector. As the BGO material has a very high density of electrons, it can be made less bulky than lighter scintillators to achieve a useful degree of escape suppression. This enables a larger number of HPGe detectors and shields to be located near a target. The third process through which photons can interact with matter is pair production. A γ-ray with an energy that exceeds twice the rest mass energy of the electron (greater than 1.02 MeV), may be directly converted into an electron-positron pair. This process takes place in the Coulomb field of the nucleus whereby a γ-ray creates an electron-positron

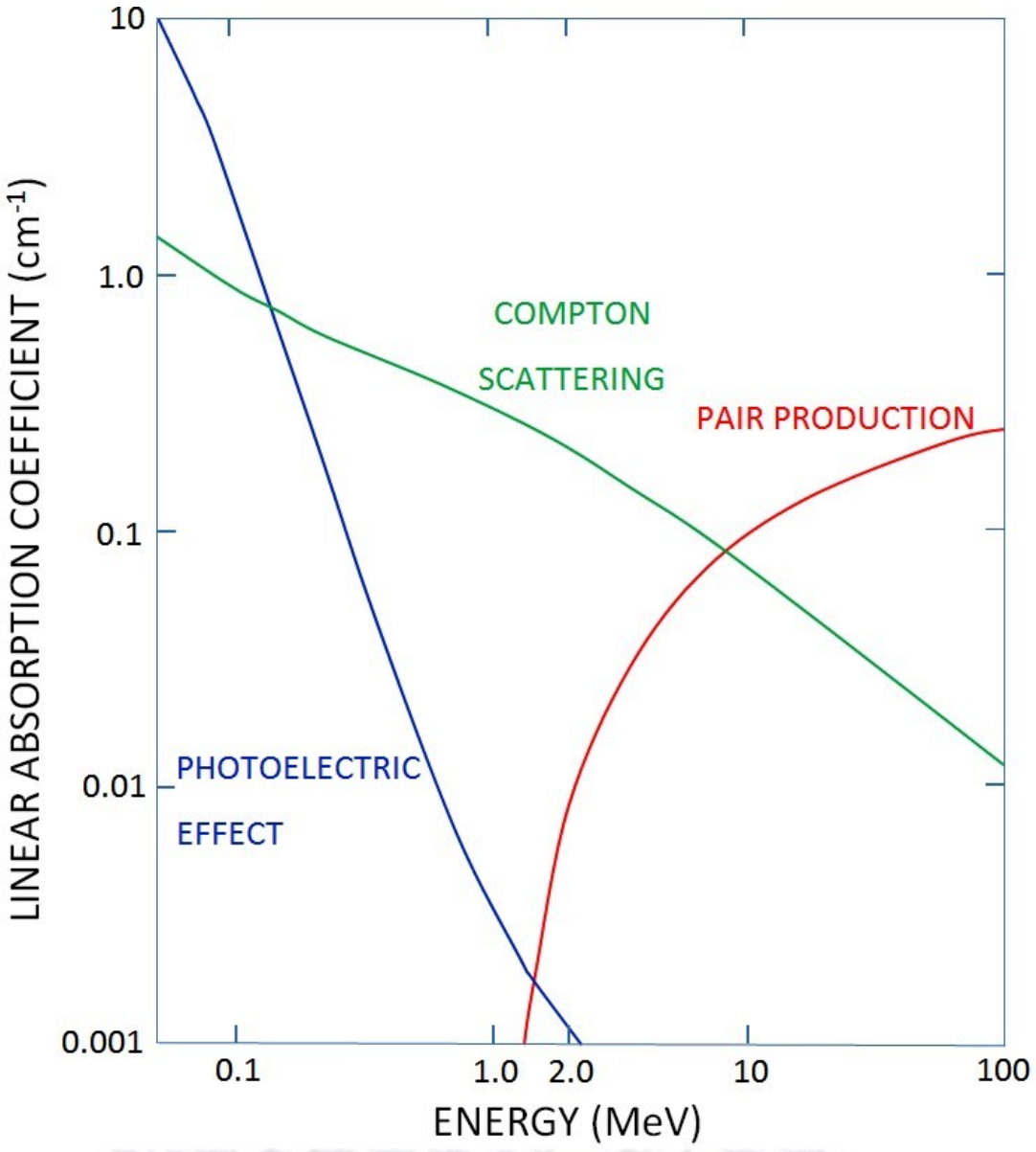

FIGURE 3.3: Illustration of the energy dependence of the various γ-ray interaction processes in a germanium crystal [8].

pair. This process is dominant for γ-ray energies greater than 5 MeV. The probability for pair production largely depends on the energy of the incident γ-ray and varies as the square of the atomic number Z. The underlying theory of these processes is well established and has been fully discussed in references [46, 92].

3.1.3 High-purity germanium (HPGe) detectors

A nucleus may emit radiation in the form of γ-rays when it de-excites. The emitted γ-rays contain information about the structure of the nucleus. In order to obtain this information we have to use detectors to detect those γ-rays. The best detectors for

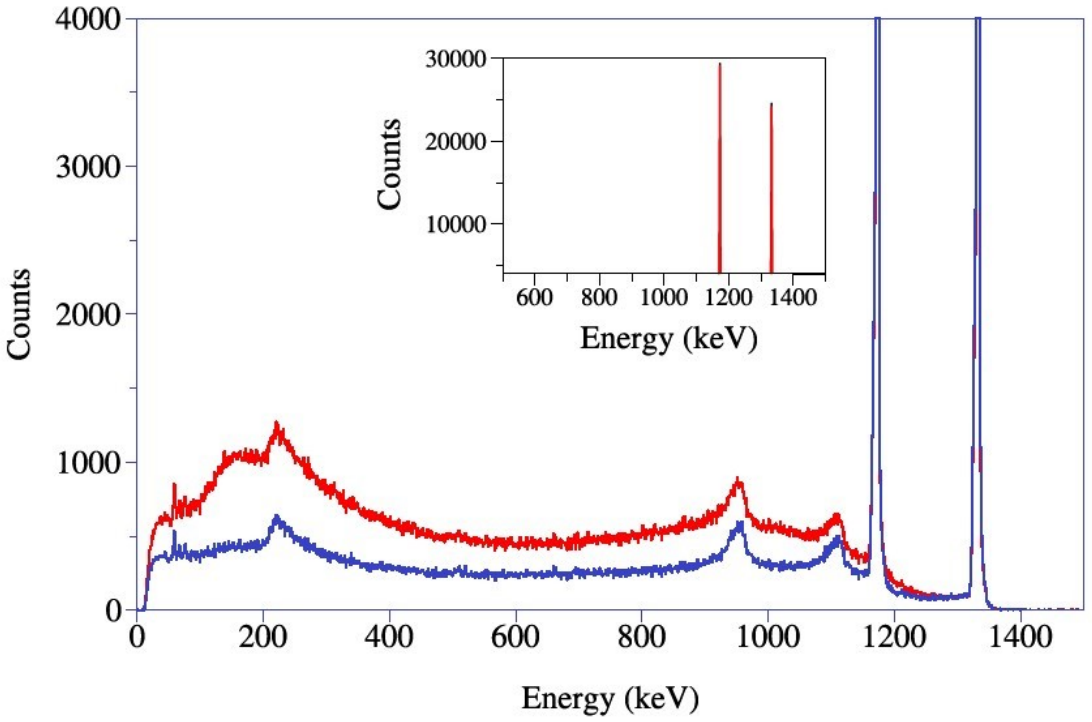

FIGURE 3.4: This figure illustrates the impact of the Compton continuum on the energy spectra. The red colored spectrum indicates a huge background caused by the Compton scattered events and the blue colored spectrum shows a case where Compton background has been significantly suppressed with the aid of a Compton suppression shield. The insert shows the spectrum at high number of counts where the top part of the photo-peaks are visible [8].

γ-ray spectroscopy are high-purity germanium (HPGe) detectors. The HPGe detectors are made of semiconductor material which has a superior energy resolution when cooled to liquid nitrogen temperature. This superior energy resolution is possible because a comparatively low energy, 3 eV, is needed to create an electron-hole charge pair [92]. These detectors are made of four coaxial n-type Ge crystals arranged in a form of a clover leaf, hence the name clover detectors. Clover and LEPS detectors are examples of HPGe detectors. Clover detectors are very efficient in measuring the high energy γ-rays above 100 keV. These detectors have a large peak to total (P/T) ratio. The large P/T ratio is achieved by surrounding the detector with a BGO shield which reduces the background from the Compton scattering of the high energy γ-rays. The specification for the energy resolution for each crystal for high energy γ-rays of 1.33 MeV is less than 2.1 keV and for low energy γ-rays of 122 keV, the resolution is less than 1.1 keV at full width at half maximum (FWHM). These features make the clover detector an essential and effective tool for γ-ray spectroscopy. The low energy photon spectrometer (LEPS) detectors are made of a single germanium crystal about 10 mm thick. In the AFRODITE spectrometer the LEPS crystals are electrically segmented into four quadrants. These detectors are effective to detect γ-rays below 200 keV as well as X-rays.

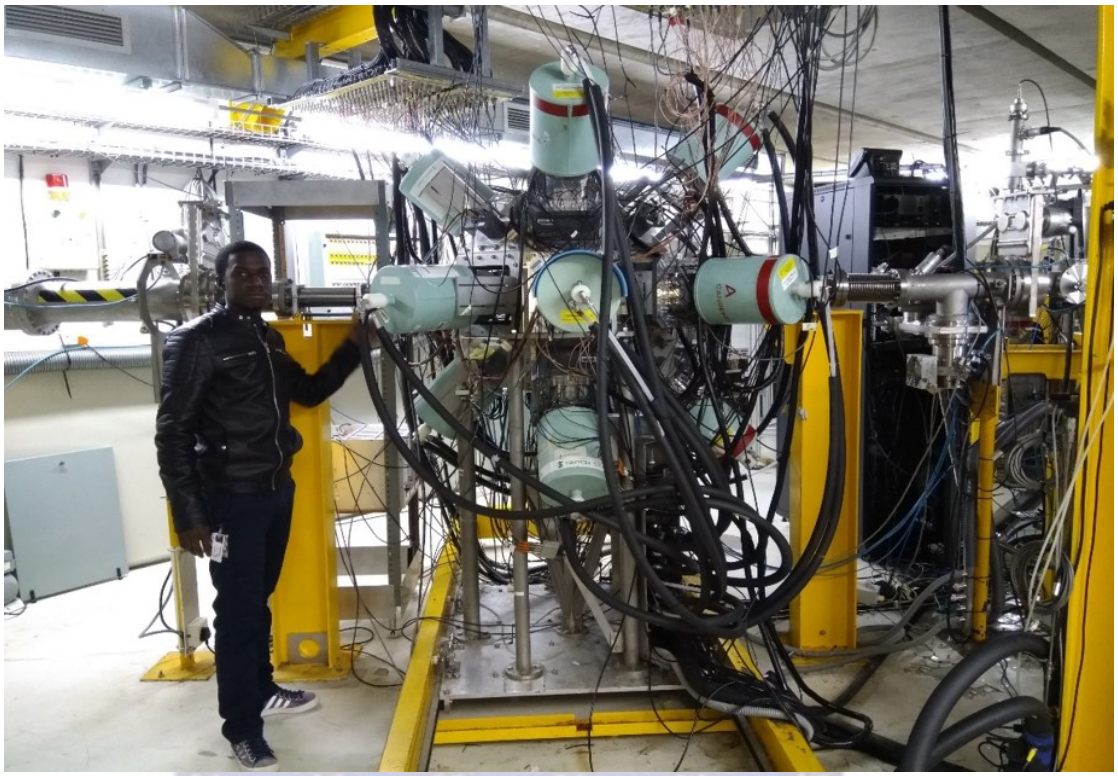

FIGURE 3.5: Photo showing HPGe clover detectors in BGO shields in the AFRODITE array together with LEPS detectors at the forward angles.

3.1.4 The AFRODITE array

The AFRODITE array was used to detect γ-rays emitted from the residual nuclei produced in the heavy ion fusion reaction explained in section 3.1.1. The array normally consists of two types of germanium detectors namely, clover and low energy photon spectrometer (LEPS) detectors. The AFRODITE-array can accommodate a maximum of 16 germanium detectors. The germanium detectors are mounted in a rhombicuboctahedron frame which is composed of 18 square facets positioned at 0, 45°, 90°, 135° and 180° with respect to the beam direction. The target is mounted at the centre of the array while the 0° and 180° angles are used for the beam line. The germanium detectors are maintained at liquid nitrogen temperature in their own cryostats. The liquid nitrogen dewars are filled every 24 hours by an automatic filling system. Fig. 3.5 is a photograph showing the array in the current work. The array consisted of 11 HPGe clover detectors in BGO shields, 4 LEPS and 8 LaBr detectors.

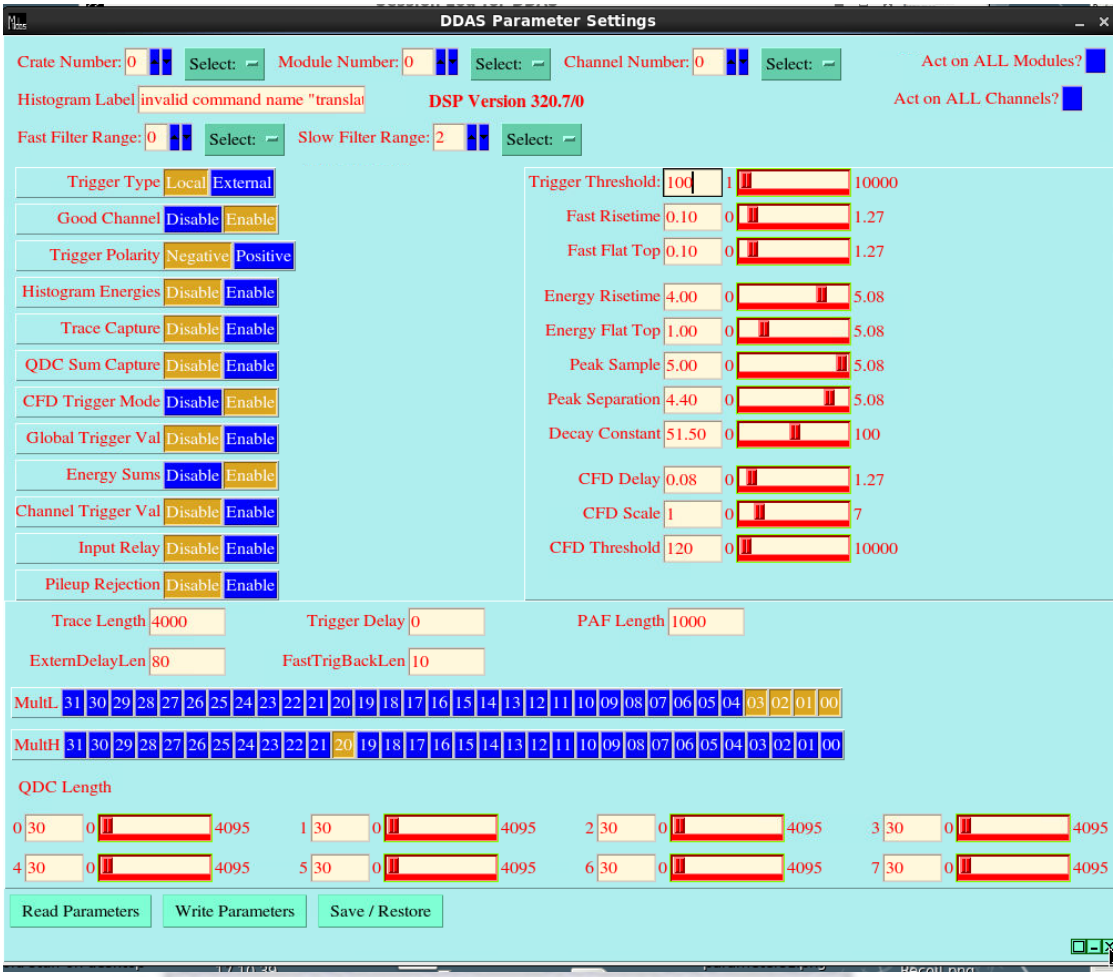

FIGURE 3.6: A DDAS window displaying a set of parameters used for the optimization of the system for better energy resolution of an individual detector.

3.1.5 Basic ideas on the electronics used in this experiment

In order to collect nuclear spectroscopy data an appropriate data acquisition system is required. At iThemba LABS, Digital Data Acquisition System (DDAS) is used for AFRODITE experiments including the current experiment (PR296). The DDAS comprises two distinct processes, the first process is the front-end system which consists of XIA crate and Pixie-16 modules connected to a server PC. The server PC hosts and runs the acquisition for data collection. The second process is the control part on the server PC running the merge, filter, event-building, on-line sorting, storage and graphic unit interface. Data are read from the merger and output to tape server. The tape server receives and stores data locally, either on a USB, tape, disc, network, etc. The stored data can be sorted with the MTsort [93–96]. A DDAS window that shows an example for a set of input parameters used to optimize the system for better energy resolution for an individual Ge crystal of a clover detector is shown in Fig. 3.6.

3.2 Data analysis

This section explains the techniques and methods used to analyse the data obtained from the current work. The data was collected over 9 shifts. The large amount of data collected was copied to external hard drive at the end of the experiment for offline analysis. Midas [93] and MTSort were used to sort our data into a matrix form. The RadWare [97] software packages were used to examine the matrix effectively determine the coincidence relationships of the observed γ events.

3.2.1 Gain-matching

In general, the gain of all data acquisition channels is different, thus the correspondence between the energy and the channel number is different. Therefore, before combining the data from different detectors for data analysis all clover detectors have to be gain matched to avoid mismatching in the spectra. During the experiment, there were changes in the gain-matching coefficients of the clover crystals, also called gain drifts which were probably caused by temperature variations during the run of the experiment. These drifts disrupt the energy calibration, and result in the peaks in the clover spectra being misaligned. The shifts were corrected by using an accurately calibrated spectrum from the beginning of the experiment. The shifted spectra were fitted in GF3, their centroids extracted, and the correct gain-matching coefficients were obtained. The AG command was used to test whether the drifts can be corrected by applying a linear transformation to the position of each channel as shown in equation 3.3,

$$x' = a + bx, \tag{3.3}$$

where x' is the new channel number, x is the old (shifted) channel number, b = (OLDCH2-OLDCH1)/(NEWCH2-NEWCH1) and a = OLDCH2 - b*NEWCH2. After confirming that the drifts were linear the measured shifted centroids of two reference peaks were measured for each run and gain drift correction was introduced. It is important to be consistent with the choice of the peaks used for gain-matching. Once the gain-matching process has been completed, the data has to be sorted again to make sure that all the peak centroids from all the clover detectors and in all runs are aligned.

3.2.2 Energy calibration

In order to properly identify the various γ-ray peaks in the spectra of the detectors, the detectors must be calibrated. From the detectors we collect the charge signal for which

the amount of charge corresponds to the detected γ-ray energy. The data acquisition system transforms the energy information into channel number. In order to identify peaks, we have to do energy calibration to convert back from the channel number to energy. One reason to do energy calibration for each experiment is because the detectors may perform differently from one experiment to the next. A radioactive γ-ray source such as ^{152}Eu, ^{133}Ba, ^{60}Co is commonly used to supply peaks of known energies in the spectrum. This is done because the raw data stored on the hard disk is in the form of channels and the correspondence between the channels and the energies is not the same for any two crystals. This correspondence between the energies and the channels for each crystal is determined with the help of data from a source of known γ-ray energies. In the current work we used ^{152}Eu source which has γ-ray energies that are not very different from those to be measured in the ^{187}Os spectrum. This source has a γ-ray spectrum with the energies ranging from 40 to 1408 keV and also the relative intensities for these γ-rays are well known [98]. The energy calibration was done before the start of the experiment, where the ^{152}Eu source was placed on the target ladder inside the target chamber and the data were recorded in event mode. In the current work we used the RadWare software package [108] to determine the centroid of each photo-peak and to fit the spectra for ^{152}Eu source. This software has a built-in functions for energy calibration functions such as "ca", "ca3" and "ca4". However in this work we used the "ca" command to automatically fit the entire spectrum and calculate the energy calibration coefficients. The "ca" command requires the source file (.sou) which contains γ-ray energies and intensities of all the individual radioactive sources. The relations between the data acquisition channel x and the γ-ray energy for the clover detectors was parametrized using the quadratic equation:

$$E = a + bx + cx^2, \tag{3.4}$$

where a, b and c are energy calibration coefficients for an individual crystal of all the clover detectors and x is the channel number. These coefficients are used in the sorting code to gain match the collected data during the experiment and offline.

3.2.3 Addback

The clover detectors of the AFRODITE γ-ray spectrometer are made up of four crystal elements. This configuration is important because it enhances the peak-to-total ratio P/T by applying an add-back procedure. Therefore, γ-rays can be fully absorbed in a single crystal or can be Compton scattered first in one crystal and then in another crystal. The energy deposited in the first crystal can be added to the energy deposited

in the second crystal to recover the total energy of the γ-ray. This technique is called addback and is very important in increasing the photo peak efficiency for high energy γ-rays.

3.2.4 Efficiency calibration

Efficiency of a detector can be defined as a ratio between the number of γ-rays detected over the number of γ-rays emitted by the source. For instance, if we have a source that emits 100 γ-rays, and the detector detects all 100 γ-rays, it means the detector has 100% efficiency. If it detects 50 out of 100, it has 50% efficiency. After the experiment the efficiency calibration was done to accurately determine the intensity of the γ-rays measured during the experiment. Unlike for the energy calibration discussed in section 3.2.2, when we collect data for the efficiency calibration the source must be exactly placed at the target position to reflect the efficiency relevant to the collected data. In the present work a ^{152}Eu source was used to perform efficiency calibration. The data were recorded in singles mode and later sorted offline using the MTsort program [94] and the output spectra were converted into RadWare [97] readable format using the eg2rad command. The RadWare GF3 program was then used to find the peak areas and the centroids for peaks in the source spectrum. The RadWare EFFIT program was used to fit the data points obtained from the ^{152}Eu source. The program EFFIT reads the data from the input file .sin and fits an efficiency curve for the data using the following expression:

$$\epsilon_\gamma = e^{[(A+Bx+Cx^2)^{-G}+(D+Ey+Fy^2)^{-G}]^{\frac{1}{G}}}, \tag{3.5}$$

where G denotes the interaction parameter between the low and high energy regions. Parameters A, B and C describe the efficiency at low energies and D, E and F describe the efficiency at high energies. The parameters x and y are given by:

$$x = ln\left[\frac{E_\gamma}{100}\right], \tag{3.6}$$

$$y = ln\left[\frac{E_\gamma}{1000}\right]. \tag{3.7}$$

The relative efficiency curve shown in Fig. 3.7 was obtained using the RadWare EFFIT program [97]. As shown in Fig. 3.7, the efficiency is energy dependent and its maximum for clover detectors occurs at ~122 keV. At low energy the efficiency of the detector decreases steeply as the absorption by the cryostat end-cap increases. At higher energies

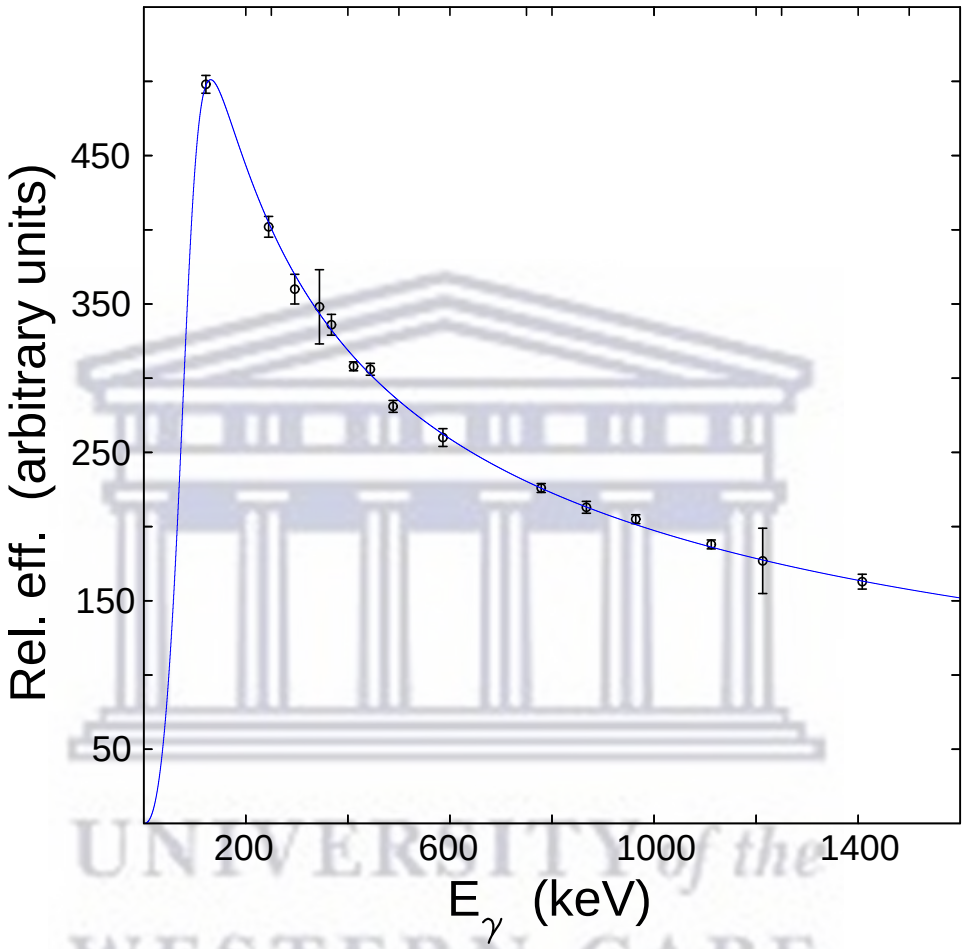

FIGURE 3.7: Relative efficiency curve for all 11 AFRODITE clover detectors measured with a ^{152}Eu source.

there is a higher probability that the γ-rays will not interact with the crystals. The probability to detect high energy γ-rays is much smaller compared to those with energy $\sim$200 keV, which are stopped and easily detected. This decrease in efficiency is caused by the decrease in cross section of both the photoelectric effect and Compton scattering as a function of the energy of the γ-rays, see Fig. 3.3.

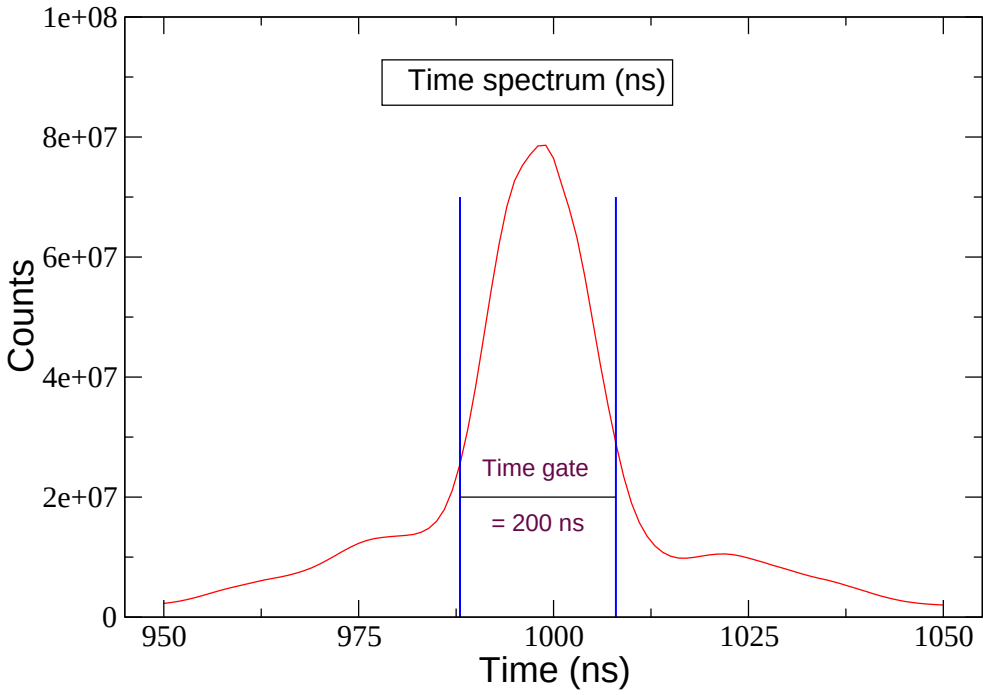

FIGURE 3.8: A plot of the time spectrum showing the difference in the times of two coincident γ-rays. The prompt events occurred in the range 988-1008 ns.

3.2.5 Time gate condition

In order to minimize the randoms in our data, the sorting code was edited and different time gates were chosen, for an example the 200 ns gate shown in Fig. 3.8. This time gate was chosen to maximize the events from the nucleus of interest to be sorted and the unwanted events, such as, randoms and background to be vetoed. A shorter time gate results in fewer randoms and the longer time gate results in more randoms. The random coincidences cannot be completely avoided, but they can at least be minimized [12]. However, a too short coincidence window can cause a loss of efficiency to detect low energy transitions which demand slightly longer time for charge collection. For this reason three sorts, each with a different time-gate, were performed, the first with a true gate of 10 channels (100 ns), the second with 20 channels (200 ns), and lastly with 31 channels (310 ns). The 200 ns time gate was found to be the perfect time gate in this work. Therefore this gate used for the construction of the present level scheme.

3.2.6 Coincidence matrices

After the clover data have been gain matched, it was sorted into five RadWare-compatible [97] γ-γ matrices. The first one was used to build the level scheme of the ^{187}Os nucleus. It is a symmetric matrix (equal counts on both x and y axes). Two asymmetric matrices were used to measure angular distribution ratios. In these matrices the γ-ray energies on the x-axis were detected by all detectors while the ones on the y-axis were detected by the detectors at 90°, or 135°. These are the 90° vs all matrix and 135° vs all matrix, respectively. The other two asymmetric matrices were used in the polarization analysis, for the purpose of parity assignments. The γ-ray energies on the x-axis were also detected at all angles and the ones on the y-axis were detected by the detectors positioned at 90° with respect to the beam direction, taking only the events that correspond to perpendicular and parallel Compton scattering events only. The RadWare code ESCL8R was used to examine the γ-γ matrix and study the γ-γ coincidence relationships. This code enables the user to set individual gates on transition energies on one axis and project them onto the other axis. The resulting spectrum displays transition energies that have been detected in coincidence with a γ-ray energy that is gated upon. This mechanism can be easily understood in terms of the demonstration shown in Fig. 3.9 (i) which presents a γ-γ matrix. A series of gated γ-rays spectra, which demonstrate how the coincident γ-rays appear in the gated spectra are also shown in the figure. The analysis of such gated spectra helps to discover the coincidence relationships and build the level scheme of the nucleus, as discussed below.

3.2.7 The γ-γ coincidence

The decay process of an excited nucleus usually produces many γ-rays that are emitted in quick succession. When these γ-rays hit the detectors, for each of them, the data acquisition records the γ energy, detector number and the arrival time. When the data are sorted, for every coincident event recorded, the time difference between any pairs of the detectors is calculated and checked if it is within the coincidence window. In the current experiment, a coincidence time window of 200 ns was set and any pairs of γ-rays that arrived within that time were considered a γ-γ coincidence event and the γ-rays were regarded as belonging to one decay path. However, tracking down numerous decay paths that are formed following a fusion evaporation reaction is usually a challenge. This is mainly because the resulting γ decays are a consequence of a countless number of nuclear levels, which span over a broad range of excitation energies, starting from zero to about tens of MeV.

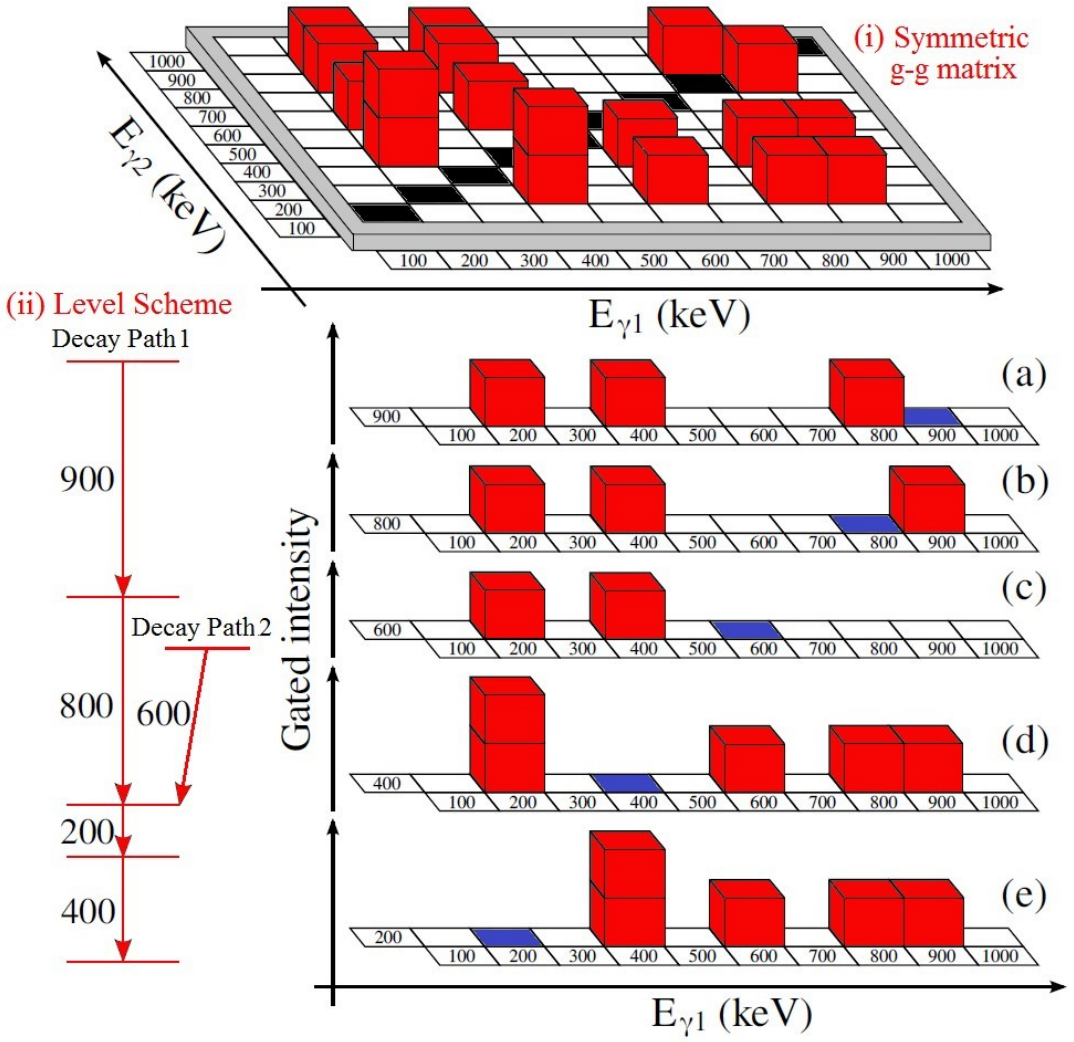

FIGURE 3.9: This figure demonstrates how to set a gate on the γ-γ matrix and also how to observe the γ-rays that are in the same decaying path. For example, when a gate is set on 400 keV (E_{γ_1} axis) and projected on (E_{γ_2} axis), the resulting spectrum (see section (d) of this figure) displays γ-rays, which share the same decay path with it (i.e., 200-, 600-, 800- and 900-keV). After careful consideration of all decay paths, the information can be used to build a level scheme such as the one shown (ii). The labels (a), (b), (c), (d), and (e) represent gated spectra and the blue shade denotes the gate on each spectrum [8].

3.2.8 Construction of the level scheme

The ESCL8R is an interactive program for graphics-based analysis of γ-γ coincidence data for the construction of level schemes. It allows to edit, built-up level scheme continually as the analysis proceeds. Energies and intensities of the γ-ray transitions in the level scheme can be fitted using the γ-γ matrix. Shown in Figure 3.10 is the background-subtracted total projection spectrum of the current work. Level scheme building process starts with known transitions, known levels and known cascades and it can be expanded as the investigation of spectra that are gated below or above of those

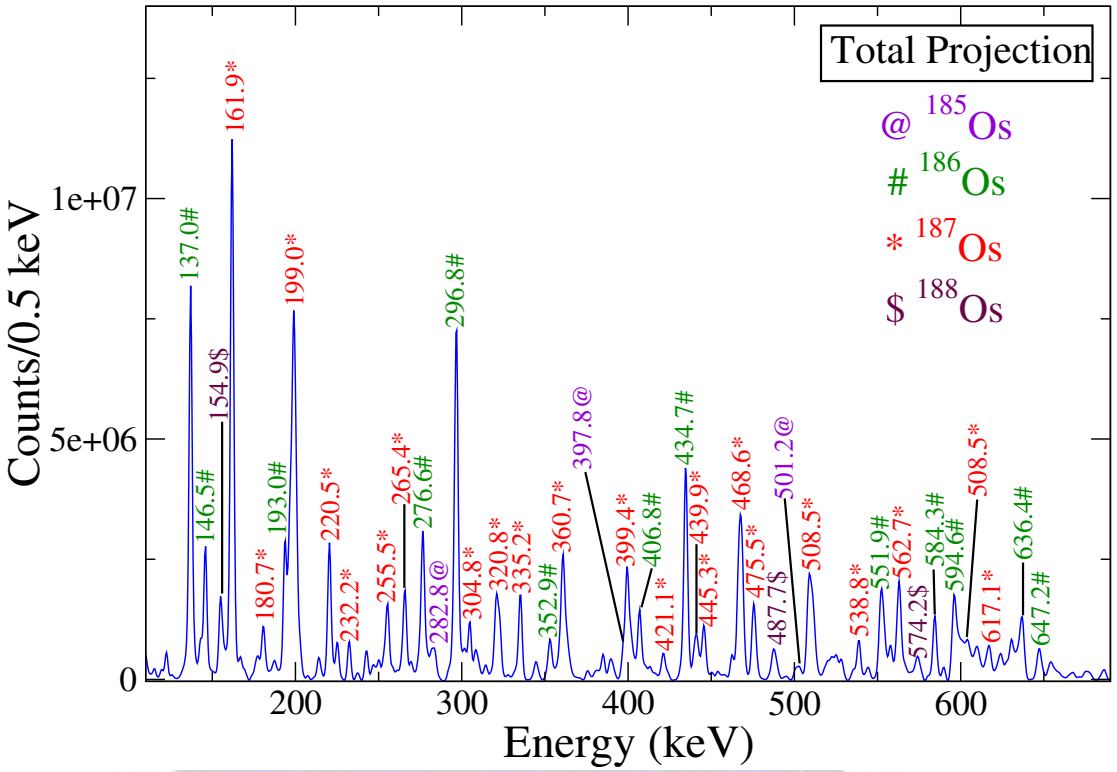

FIGURE 3.10: Background-subtracted total projection spectrum. The γ rays denoted by violet and labelled by a (@) symbol belong to ^{185}Os. The γ rays that belong to ^{186}Os are labelled in green and a hash (#) symbol. The γ rays labelled in red and asterisk (*) symbol belong to the ^{187}Os nucleus. The γ rays denoted by maroon and labelled by a ($) symbol belong to the ^{188}Os nucleus.

known γ-ray transitions are investigated. If we take a gate on the lowest ground-state transition, we see hundreds of transitions in the spectrum and it is hard to determine how to place them in the right position in the level scheme. If we take a gate on a known transition that is positioned at a higher energy in the level scheme, we see only the transitions that feed the initial level of the gating transition or decay below the final level of the gating transition. Such gated spectra contain fewer peaks and it is usually easier to identify the placement of the observed new transitions.

3.2.9 Measurement of γ-rays relative intensities

The γ-ray intensities are important for calculating the angular distribution ratios, transition probabilities and branching ratios. They are also useful for the coincidence analysis and the level scheme construction. These γ-ray intensities can indicate the ordering of the transitions in rotational bands. The γ-ray intensity is deduced from the gated spectra, which are fitted to obtain the areas of the peaks of interest and their corresponding uncertainties. In general the γ-rays intensity can be calculated using the following relation:

$$I_\gamma = \frac{A_\gamma}{\epsilon_\gamma}, \tag{3.8}$$

where A_γ is the area of the peak and ϵ_γ is the efficiency of the array for the energy of the γ-ray of interest. However in this work "xmesc" program was used to measure the intensities of the γ-rays of the ^{187}Os nucleus. This program uses the command "Fit" to fit the intensities of the γ-rays added in the decay scheme of the ^{187}Os nucleus. The measured intensities for the γ-rays of interest are listed in Table 4.1.

3.2.10 Spin and parity measurements

The spin and parity measurements of the energy levels were performed upon building the decay scheme. It was done by analyzing the angular distribution ratios and the linear polarizations of the emitted γ-rays.

3.2.10.1 Spin measurement

For fusion evaporation reactions the intensity of the γ-rays emitted in different directions in space obeys an angular distribution which is given by [12, 99]:

$$W(\theta) = \sum_{k=even} \alpha_k A_k(J_i, L_1, L_2, J_f) P_k(\cos\theta), \tag{3.9}$$

where $P_k(\cos\theta)$ is Legendre polynomial and depends on θ only, A_k are the angular distribution coefficients which are theoretically calculated. The A_k depend on the initial and final spins J_i and J_f respectively, on the multiple order of the radiation L_1 and if the transition is mixed on $L_2 = L_1 + 1$, and the mixing ratio δ. The attenuation coefficients α_k have values between 0 and 1 and are expressed as a function of the distribution parameter (σ/J), where σ is the Gaussian parameter of the alignment of the nuclear state and J is its spin [12, 99].

In the current work, the AFRODITE array consisted of 4 clovers at 135° and 7 clovers at 90°. The angular distribution ratios were deduced from data collected using detectors at 90° and 135° and the measured ratios were used to assign spins to the excited nucleus states. The angular distribution ratios in this work are given by:

$$R_{AD} = \frac{I_{\gamma_1}^{135^\circ}(Gated_{\gamma_2}^{all})}{I_{\gamma_1}^{90^\circ}(Gated_{\gamma_2}^{all})}, \tag{3.10}$$

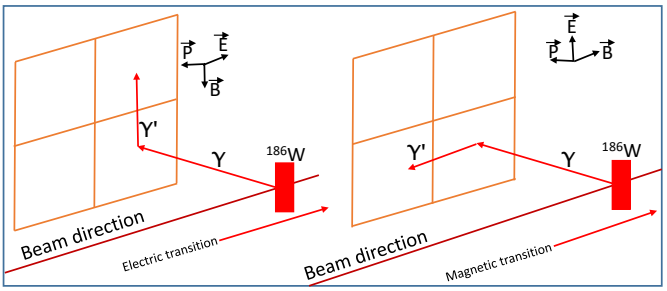

FIGURE 3.11: Compton scattering in clover detector for stretched electric and magnetic transition, modified from [12].

where the numerator of equation 3.10 denotes the coincidence intensity of the γ-ray of interest, γ_1 detected at an angle of 135°, gated on γ_2 detected in all detectors. The denominator of equation 3.10 denotes the coincidence intensity of γ_1 detected at an angle of 90°, gated on γ_2 detected in all detectors. The measured R_{AD} ratios gives a value ∼0.43 for pure stretched dipoles and a value of ∼0.87 for a stretched quadrupoles.

3.2.10.2 Parity measurement

Linear polarization measurements were performed to determine whether the γ-ray is electric or magnetic in nature. In linear polarization measurements we are mostly interested in a fraction of the γ-rays that hit a crystal of a clover detector and Compton scatter into another crystal where they are absorbed. As these γ-rays have larger probability to scatter perpendicular to their electric field vector $\vec{E}$, one can determine an electric or magnetic nature of the transition by knowing the Pointing vector $\vec{P}$ which is a directional vector of the electromagnetic energy and measuring the direction of $\vec{E}$ from the number of double hit events scattered vertically and horizontally, see Fig. 3.11. The polarization anisotropy A_P is expressed as:

$$A_P = \frac{\alpha N_V - N_H}{\alpha N_V + N_H}, \tag{3.11}$$

where N_V and N_H are the number of γ-rays scattered between the crystals of the clover detectors at 90° perpendicular and parallel to the beam direction, respectively. The relative efficiency parameter $\alpha = N_H/N_V$, is determined using unpolarized γ-rays as α = 1.07.

Chapter 4

Experimental results

This chapter presents results on the ^{187}Os level-scheme that were obtained in the current work. The AFRODITE γ-ray spectrometer array [85] was used to detect $\gamma - \gamma$ coincidences events produced from the ^{186}W(^{4}He,3n)^{187}Os reaction at 37.0 MeV. The experimental set up for this work is discussed in chapter 3. The data from the 11 HPGe clover detectors in BGO shields were analyzed and the results are presented in this chapter. Approximately 3.7×10^{9} events were unfolded from the data in the offline analysis and replayed into a $\gamma - \gamma$ RadWare [97] matrix through which the level scheme for the ^{187}Os nucleus was created.

4.1 Rotational bands in ^{187}Os

The nuclear structure of ^{187}Os was previously investigated in Refs. [7, 29–36, 100]. In their work, the band heads and some low-energy levels of the rotational bands of ^{187}Os were observed but not fully established. The current work is aimed at searching for new collective structures and extending the known rotational bands of ^{187}Os. In this present work we have not only managed to reproduce and confirm the validity of the findings by the previous in-beam work [7] but have also established numerous additional rotational structures, see Figs. 4.1, 4.12 and 4.18. New transitions deduced in the present work are labelled in red, while transitions from previous in-beam work are labelled in black. Angular distribution and polarization measurements have been performed to identify the spins and parities of newly established structures and to confirm the assignments made by the previous works. Measured properties of γ-rays and rotational levels observed in this work are listed in Table 4.1.

TABLE 4.1: The angular distribution ratios, R_{AD}, the γ-ray intensities and the polarization asymmetries, A_P, measured for the γ-ray transitions with energies of E_γ, together with the assigned multipolarities (γ Mult.). E_i (I_i^π) and E_f (I_f^π) are the energy (spins) for the initial and final levels, respectively. The star ($*$) symbols indicate the new transitions that have been established in the current work. The dash sign (-) refers to information that could not be obtained. The uncertainties on the γ-ray energies are typically of 0.3-keV for strong transitions and up to 0.5-keV for weak transitions and doublets.

E_i (keV)	E_f (keV)	E_γ (keV)	I_γ	I_i^π	I_f^π	R_{AD}	A_p	γ Mult.
Band 1								
74.4	0.0	74.4	-	$3/2^-$	$1/2^-$	0.46 (9)	-	$M1/E2$
329.9	74.4	255.5*	55.3(9)	$7/2^-$	$3/2^-$	0.86 (1)	0.22 (18)	$E2$
731.7	329.9	401.8*	36.1(12)	$11/2^-$	$7/2^-$	0.87 (1)	0.21 (11)	$E2$
1259.7	731.7	528.0*	24.8(8)	$15/2^-$	$11/2^-$	0.96 (2)	-	$E2$
1883.9	1259.7	624.2*	15.9(5)	$19/2^-$	$15/2^-$	0.94 (2)	-	$E2$
2558.6	1883.9	674.7*	8.5(3)	$23/2^-$	$19/2^-$	0.97 (2)	-	$E2$
3237.1	2558.6	678.5*	2.40(12)	$27/2^-$	$23/2^-$	0.94 (2)	-	$E2$
Band 2								
187.2	0.0	187.2	5.9(3)	$5/2^-$	$1/2^-$	0.80 (3)	-	$E2$
187.2	9.8	177.4	8.9(6)	$5/2^-$	$3/2^-$	0.73 (2)	-	$M1/E2$
508.1	187.2	320.9	20.7(10)	$9/2^-$	$5/2^-$	0.84 (2)	-	$E2$
508.1	190.5	317.6*	5.3(3)	$9/2^-$	$7/2^-$	0.88 (7)	-	$M1/E2$
951.2	508.1	443.1*	15.1(6)	$13/2^-$	$9/2^-$	0.72 (3)	-	$E2$
951.2	511.3	439.9*	3.9(3)	$13/2^-$	$11/2^-$	0.47 (2)	-	$M1/E2$
1494.8	951.2	543.6*	9.6(4)	$17/2^-$	$13/2^-$	0.97 (3)	-	$E2$
2110.6	1494.8	615.8*	6.6(3)	$21/2^-$	$17/2^-$	0.93 (4)	-	$E2$
2762.0	2110.6	651.4*	2.15(14)	$25/2^-$	$21/2^-$	0.77 (8)	-	$E2$
Band 3								
190.5	9.8	180.7	21.4(6)	$7/2^-$	$3/2^-$	0.84 (1)	-	$E2$
511.3	190.5	320.8	36.7(12)	$11/2^-$	$7/2^-$	0.88 (1)	0.11 (19)	$E2$
956.6	511.3	445.3*	31.1(10)	$15/2^-$	$11/2^-$	0.86 (2)	0.05 (18)	$E2$
1492.1	956.6	535.4*	5.9(6)	$19/2^-$	$15/2^-$	0.88 (4)	-	$E2$
1492.1	935.0	557.1*	21.1(7)	$19/2^-$	$15/2^-$	0.98 (2)	-	$E2$
1492.1	1209.6	282.4*	6.9(3)	$19/2^-$	$17/2^-$	0.44 (4)	-	$M1/E2$
2102.1	1492.1	610.0*	24.9(8)	$23/2^-$	$19/2^-$	1.03 (4)	-	$E2$
2729.5	2102.1	627.4*	10.7(4)	$27/2^-$	$23/2^-$	1.05 (3)	-	$E2$

All the R_{AD} ratios in Table 4.1 were obtained by setting a gate on pure stretched quadrupole transitions. The experimentally measured R_{AD} ratios as a function of energy is shown in Fig. 4.2. For polarization measurements, the A_P values yield $A_P < 0$ and $A_P > 0$ for pure stretched magnetic and electric transitions, respectively, see Fig. 4.3

4.1.1 Negative-parity bands

This section presents the results for the negative-parity bands of ^{187}Os deduced in this work. We report eight negative-parity bands in the current ^{187}Os level scheme. Bands 1, 6, 7 and 1A are entirely new, while bands 2, 3, 4 and 5 have been significantly extended, see Fig. 4.1.

4.1.1.1 Bands 1 and 2

Band 1 is a new rotational sequence built on the known 74.4-keV energy level. This level was assigned the -1/2 signature of the $1/2^-[510]$ Nilsson configuration [7]. In the present work, 6 in-band transitions have been added to band 1. The angular distribution measurements carried out for all in-band transitions are consistent with stretched quadrupole (ΔI = 2) nature. Band 1 decays to the 0 keV level via the 74.4-keV transition. Fig. 4.4 shows a spectrum with transitions associated with band 1.

Band 2 has been previously observed up to $I^\pi = 9/2^-$ by Ref. [7]. In the present work this band has been extended significantly up to $I^\pi = 25/2^-$. The R_{AD} values extracted for the in-band transitions, which include the four new transitions (443.1-, 543.6-, 615.8- and 651.4-keV), are consistent with stretched quadrupole (ΔI = 2) nature. This band decays to band 3 through the 439.9-, 317.6- and 177.4-keV transitions. While the latter (i.e 177.4-keV transition) is known from the previous study [7], the former transitions are new. According to Ref. [7], the multipolarity of the 177.4-keV transition is consistent with mixed M1/E2 nature. The R_{AD} values for the 177.4- and 317.6-keV transitions measured in our work also suggest that these linking transitions have mixed M1+E2 nature. The R_{AD} value for the 439.9-keV transition however shows that this transition is a stretched dipole. Therefore bands 2 and 3 have the same parity and are linked by $I \rightarrow (I-1)$ transitions. This is in agreement with the previous spin and parity assignments for the low-energy levels of these bands. Fig. 4.5 shows a coincidence spectrum which confirms the presence of the new transitions of band 2.

4.1.1.2 Band 1A

As shown in Figs. 4.1 and 4.6, a series of new levels that decay to band 1 have been observed and are identified as Band 1A. This band decays to band 1 via 406.1-, 533.3- and 633.2-keV transitions. The R_{AD} values for the 406.1- and 633.2-keV transitions were found to be 0.59(2) and 0.46(3), respectively, suggesting that these transitions have stretched dipole (ΔI = 1) character. The R_{AD} value for the 533.3-keV transition

could not be obtained due to insufficient statistics. The polarization asymmetries A_p for the transitions in these bands could also not be obtained due to low statistics.

4.1.1.3 Band 3

Band 3 was previously known up to $I^\pi = 11/2^-$ and only had two in-band transitions, namely 180.7- and 320.8-keV transitions which were reported by Ref. [7]. In the current work this band has been extended up to $I^\pi = 27/2^-$ by four in-band transitions (see Figs. 4.1 and 4.7). The R_{AD} and polarization measurements deduced for the in-band transitions are consistent with them being stretched E2. Band 3 decays to bands 4 and 5 through the 557.1- and 282.4-keV transitions, respectively. The R_{AD} values for these transitions are consistent with stretched quadrupole ($\Delta I = 2$), and stretched dipole ($\Delta I = 1$) nature, respectively.

4.1.1.4 Bands 4 and 5

Bands 4 and 5 are signature partner bands built on the isomeric state at 100.5-keV with half-life of 112 ns. In the previous in-beam work [7], these bands were observed up to $I^\pi = 15/2^-$ and $I^\pi = 17/2^-$, respectively. The current work has extended these bands up to $I^\pi = 27/2^-$ and $I^\pi = 29/2^-$, respectively, (see Figs 4.1, 4.8, 4.9 and Table 4.1). Band 4 decays to band 5 through 196.1-, 250.3-, 301.7-, 331.4 and 351.5-keV transitions. The 196.1- and 250.3-keV transitions were previously reported in Ref. [7], but their multipolarities were not measured. In the current work, the R_{AD} values for these transitions were measured and found to be 0.40(3) and 0.56(4), respectively, thus suggesting stretched dipole (ΔI = 1) nature. Band 5 also decays to band 4 through the 162.6-, 225.3-, 274.8-, 302.3- and 325.3-keV transitions. The first three transitions are known from the previous in-beam work [7] but their multipolarities were not deduced. In the current work, the R_{AD} measurements performed for these transitions are suggestive of a stretched dipole (ΔI = 1) nature.

4.1.1.5 Bands 6 and 7

Bands 6 and 7 are new bands built on the known 444.9-keV and 687.4-keV energy levels, respectively [7]. The current work has established these bands up to $I^\pi = 21/2^-$ and $I^\pi = 23/2^-$, respectively, (see Fig. 4.1, and Table 4.1). These bands decay to both bands 4 and 5. Band 6 decays to band 4 through the 488.2- and 344.4-keV transitions. It also decays to both bands 5 and 7 through the 181.9- and 260.6-keV transitions,

respectively. The R_{AD} values for the 488.2-, 344.4-, and 260.6-keV transitions were found to be 0.48(4), 0.37(2) and 0.24(10), respectively. Thus suggesting these transitions have stretched dipole ($\Delta I = 1$) character. Band 7 decays to both bands 5 and 6 through the 547.7-, 424.1-, 283.9- and 242.2-keV transitions, respectively. The R_{AD} values for the 424.1-, 283.9- and 242.2-keV transitions were found to be 0.57(5), 0.46(2) and 0.32(2), respectively, suggesting stretched dipole ($\Delta I = 1$) nature. Band 7 also decays to band 4 through the 586.9-keV transition. The R_{AD} value of this transition is consistent with stretched quadrupole ($\Delta I = 2$) nature. The R_{AD} values extracted for the in-band transitions, for both bands 6 and 7 are consistent with stretched quadrupole ($\Delta I = 2$) nature. The polarization asymmetries A_p could not be obtained for the transitions in these bands due to low statistics. Figs. 4.10 and 4.11 show spectra illustrating the transitions associated with bands 6 and 7.

4.1.2 Positive-parity bands

Fig. 4.12 shows partial level scheme of ^{187}Os deduced in this work. The rotational structures established from this work are labeled in red while known bands deduced from previous in-beam work [7] are labeled in black.

4.1.2.1 Bands 8 and 9

Bands 8 and 9 are signature partner bands built on an isomeric state at 257.1-keV with a half-life of 231 μs [7]. This isomeric state was first observed by Conlon [101], who deduced that a 156.7-keV M2 transition with $T_{1/2}$ =231 μs is present in ^{187}Os, but was not able to place it in the decay scheme. The 156.7-keV M2 transition was then placed in the ^{187}Os decay scheme by Malmskog et al. [30], who then concluded that this transition directly feeds the 100.5-keV level and that led to the establishment of the 257.1-keV isomeric level. Bands 8 and 9 have been previously observed up to $I^{\pi} = 19/2^{+}$ and $17/2^{+}$, respectively.

The present work has extensively extended bands 8 and 9 up to $I^{\pi} = 35/2^{+}$ and $41/2^{+}$, respectively, see Figs 4.12. To illustrate the transitions in bands 8 and 9, gated spectra are shown in Figs. 4.13 and 4.14. The combined effects of the R_{AD} and polarization measurements, performed for the interlinking transitions between these bands, are consistent with them being stretched dipole in character. The R_{AD} were also obtained for some of the in-band members of both bands 8 and 9 where possible, and they are consistent with them being stretched E2 character, see Table 4.1.

4.1.2.2 Bands 10 and 11

Bands 10 and 11 are new bands built on the 894.2-keV level. The transitions were grouped together to form rotational bands. The grouping of these transitions follow the coincidence relationships in the gated spectra. At higher excitation energies the γ-ray energies increase while the intensities decrease. The measured angular distribution ratios of these rotational bands support the placement of these transitions in the proposed rotational bands. The R_{AD} ratios suggest that the in-band transitions are consistent with E2 nature. These rotational structures decay predominantly to bands 8 and 9. Figs. 4.15 and 4.16 present spectra which show transitions associated with bands 10 and 11. The spin and parity of the new 894.2-keV level, the band head of band 10, are established by the measured stretched dipole and stretched quadrupole nature of the 475.2- and 637.1-keV transitions, respectively, see Table 4.1. The spin assignment of this band is further confirmed by the measured dipole nature of all linking transitions. The R_{AD} measurements have also been measured for some of the in-band member where possible and they are consistent with them being stretched E2s. Similarly for band 11, the spin of the 1126.5-keV level is assigned based on the angular distribution values of the 508.5- and 707.5-keV transitions as well as spin and parity selection rules. The spin and parity assignment for the remaining levels of this band were further confirmed through R_{AD} measurements of the interlinking transitions decaying out of these levels.

4.1.2.3 Bands 12 and 13

Only the band heads of bands 12 and 13 were known with $I^{\pi} = 9/2^{-}$ and $I^{\pi} = 11/2^{-}$, established by the previous in-beam work [7]. The previous in-beam work assigned these bands to the $9/2^{+}[624]$ configuration. In the present work these bands are weakly populated and only two new levels were added. Fig. 4.17 shows spectra illustrating the transitions associated with these bands.

4.1.3 Other bands

Additional new states that decay to bands 8, 9, 10 and 11 are observed in this work as shown in Fig. 4.18. However, due to low statistics, these states were not assigned to any particular configurations.

4.1.4 Residual nuclei populated due to exit channels

In fusion evaporation reaction experiments there are many sources of contaminants. However, the most predominant ones are the residual nuclei produced in other reaction channels. The PACE4 results obtained in the current work indicated that the reaction used for our experiment is very clean. However, a reasonable relative yield of the ^{185}Os, ^{186}Os, and ^{188}Os nuclei were predicted in the PACE4 calculations, see Fig 3.1. The decay schemes of these nuclei observed in our data, were constructed. The main reason for building the decay schemes of these isotopes, was to avoid the confusion between the new transitions of the nucleus of interest ^{187}Os, and these contaminants. The decay schemes of these residual nuclei are shown in Figs 4.19, 4.20, and 4.21. In this work, no new γ-ray energies were observed in these nuclei.

Table 1. (Continued)

E_i (keV)	E_f (keV)	E_γ (keV)	I_γ	I_i^π	I_f^π	R_{AD}	A_p	γ Mult.
				Band 4				
459.3	100.5	358.8	30.6(15)	$11/2^-$	$7/2^-$	0.81 (2)	-	$E2$
459.3	263.1	196.1	100(4)	$11/2^-$	$9/2^-$	0.56 (4)	-	$M1/E21$
935.0	459.3	475.7	49.0(17)	$15/2^-$	$11/2^-$	0.82 (2)	-	$E2$
935.0	684.4	250.3	22.5(8)	$15/2^-$	$13/2^-$	0.40 (3)	-	$M1/E2$
1511.6	935.0	576.6*	5.9(6)	$19/2^-$	$15/2^-$	0.96 (9)	-	$E2$
1511.6	956.6	554.9*	11.2(4)	$19/2^-$	$15/2^-$	0.79 (2)	-	$E2$
1511.6	1209.6	301.7*	8.3(4)	$19/2^-$	$17/2^-$	0.24 (11)	-	$M1/E2$
2145.4	1511.6	633.8*	16.3(6)	$23/2^-$	$19/2^-$	0.94 (6)	-	$E2$
2145.4	1813.7	331.4*	2.47(18)	$23/2^-$	$21/2^-$	0.34 (2)	-	$M1/E2$
2822.1	2145.4	676.7*	6.3(3)	$27/2^-$	$23/2^-$	0.89 (6)	-	$E2$
2822.1	2470.3	(351.5*)	1.61(17)	$27/2^-$	$25/2^-$	0.45 (9)	-	$M1/E2$
				Band 5				
263.1	100.5	162.6	80.8(6)	$9/2^-$	$7/2^-$	0.45 (1)	-	$M1/E2$
684.4	263.1	421.2	35.1(13)	$13/2^-$	$9/2^-$	0.94 (2)	-	$E2$
684.4	459.3	225.3	37.7(13)	$13/2^-$	$11/2^-$	0.41 (2)	-	$M1/E2$
1209.6	684.4	525.2	32.2(11)	$17/2^-$	$13/2^-$	0.90 (1)	-	$E2$
1209.6	935.0	274.8	19.0(7)	$17/2^-$	$15/2^-$	0.58 (3)	-	$M1/E2$
1813.7	1209.6	604.1*	25.8(9)	$21/2^-$	$17/2^-$	0.93 (3)	-	$E2$
1813.7	1511.6	302.3*	5.9(6)	$21/2^-$	$19/2^-$	0.42 (8)	-	$M1/E2$
2470.3	1813.7	656.6*	9.6(4)	$25/2^-$	$21/2^-$	0.94 (3)	-	$E2$
2470.3	2145.4	325.3*	2.89(21)	$25/2^-$	$23/2^-$	-	-	$M1/E2$
3136.0	2470.3	665.7*	3.64(20)	$29/2^-$	$25/2^-$	0.90 (3)	-	$E2$
				Band 6				
444.9	100.5	344.4	15(4)	$9/2^-$	$7/2^-$	0.37 (2)	-	$M1/E2$
444.9	263.1	181.9*	5.5(14)	$9/2^-$	$9/2^-$	-	-	$M1/E2$
947.7	444.9	503.0*	9.7(5)	$13/2^-$	$9/2^-$	0.82 (3)	-	$E2$
947.7	459.3	488.2*	10.4(6)	$13/2^-$	$11/2^-$	0.48 (4)	-	$M1/E2$
947.7	687.4	260.6*	4.1(3)	$13/2^-$	$11/2^-$	0.24 (10)	-	$M1/E2$
1532.0	947.7	584.3*	12.0(6)	$17/2^-$	$13/2^-$	0.75 (2)	-	$E2$
2176.7	1532.0	644.7*	4.4(3)	$21/2^-$	$17/2^-$	0.89 (8)	-	$E2$
				Band 7				
687.4	100.5	586.9*	6.0(6)	$11/2^-$	$7/2^-$	0.75 (2)	-	$E2$
687.4	263.1	424.1*	8.5(7)	$11/2^-$	$9/2^-$	0.57 (5)	-	$M1/E2$
687.4	444.9	242.2*	7.7(5)	$11/2^-$	$9/2^-$	0.32 (2)	-	$M1/E2$
1231.9	687.4	544.5*	13.4(6)	$15/2^-$	$11/2^-$	0.87 (2)	-	$E2$
1231.9	947.7	283.9*	6.6(4)	$15/2^-$	$13/2^-$	0.46 (2)	-	$M1/E2$
1231.9	684.4	547.7*	3.3(3)	$15/2^-$	$13/2^-$	-	-	$M1/E2$
1852.6	1231.9	620.7*	7.0(4)	$19/2^-$	$15/2^-$	1.07 (10)	-	$E2$
2512.1	1852.6	659.5*	2.23(18)	$23/2^-$	$19/2^-$	0.77 (8)	-	$E2$
				Band 1A				
735.5	329.9	406.1*	9.5(5)	$11/2^-$	$9/2^-$	0.59 (2)	-	$M1/E2$
1264.4	735.5	528.9*	3.5(22)	$15/2^-$	$11/2^-$	0.76 (10)	-	$E2$
1264.4	731.7	533.3*	4.5(22)	$15/2^-$	$13/2^-$	-	-	$E2$
1892.0	1259.7	633.2*	3.9(21)	$19/2^-$	$17/2^-$	0.46 (3)	-	$M1/E2$
1892.0	1264.4	627.6*	5.4(3)	$19/2^-$	$15/2^-$	0.87 (14)	-	$M1/E2$
2570.0	1892.0	678.0*	2.1(15)	$23/2^-$	$19/2^-$	-	-	$E2$

Table 1. (Continued)

E_i (keV)	E_f (keV)	E_γ (keV)	I_γ	I_i^π	I_f^π	R_{AD}	A_p	γ Mult.
				Band 8				
617.8	257.1	360.7	42.3(2)	$15/2^+$	$11/2^+$	0.71 (4)	0.04 (9)	$E2$
617.8	419.0	199.0	100.0(3)	$15/2^+$	$13/2^+$	0.41 (4)	-	$M1/E2$
1084.2	617.8	466.5	52.8(2)	$19/2^+$	$15/2^+$	0.82 (3)	0.01 (8)	$E2$
1084.2	818.4	265.9	20.7(2)	$19/2^+$	$17/2^+$	0.41 (7)	-	$M1/E2$
1647.3	1084.2	563.0*	27.7(2)	$23/2^+$	$19/2^+$	0.83 (2)	0.03 (12)	$E2$
1647.3	1287.0	360.5*	7.3(1)	$23/2^+$	$21/2^+$	0.33 (7)	-	$M1/E2$
2301.4	1647.3	654.1*	7.8(1)	$27/2^+$	$23/2^+$	0.91 (2)	-	$E2$
2301.4	1825.8	475.5*	2.9(2)	$27/2^+$	$25/2^+$	0.59 (8)	-	$M1/E2$
3032.3	2301.4	730.9*	2.8(2)	$31/2^+$	$27/2^+$	0.93 (3)	-	$E2$
3814.5	3032.3	782.2*	0.9(1)	$35/2^+$	$31/2^+$	0.77 (6)	-	$E2$
				Band 9				
419.0	257.1	161.9	131(20)	$13/2^+$	$11/2^+$	0.45 (1)	-	$M1/E2$
818.4	419.0	399.4	51.5(2)	$17/2^+$	$13/2^+$	0.89 (2)	0.20 (14)	$E2$
818.4	617.8	200.3	44.0(2)	$17/2^+$	$15/2^+$	0.45 (1)	-	$M1/E2$
1287.0	818.4	468.6*	42.8(2)	$21/2^+$	$17/2^+$	0.89 (1)	0.08 (11)	$E2$
1287.0	1084.2	202.6*	7.7(1)	$21/2^+$	$19/2^+$	0.38 (3)	-	$M1/E2$
1825.8	1287.0	538.8*	18.0(2)	$25/2^+$	$21/2^+$	0.94 (2)	0.02 (18)	$E2$
1825.8	1647.3	178.4*	2.4(1)	$25/2^+$	$23/2^+$	0.37 (2)	-	$M1/E2$
2442.9	1825.8	617.1*	9.9(1)	$29/2^+$	$25/2^+$	0.92 (2)	0.06 (20)	$E2$
3129.3	2442.9	686.4*	3.4(2)	$33/2^+$	$29/2^+$	0.98 (2)	-	$E2$
3854.1	3129.3	724.7*	1.2(2)	$37/2^+$	$33/2^+$	0.83 (7)	-	$E2$
4575.9	3854.1	721.8*	0.5(1)	$41/2^+$	$37/2^+$	0.73 (7)	-	$E2$

Table 1. (Continued)

E_i (keV)	E_f (keV)	E_γ (keV)	I_γ	I_i^π	I_f^π	R_{AD}	A_p	γ Mult.
Band 10								
894.2	257.1	637.1*	47.5(20)	$15/2^+$	$11/2^+$	0.74 (2)	-	$E2$
894.2	419.0	475.2*	31.3(11)	$15/2^+$	$13/2^+$	0.38 (2)	-	$M1/E2$
1381.3	894.2	487.1*	7.2(3)	$19/2^+$	$15/2^+$	0.77 (2)	-	$E2$
1381.3	818.4	562.7*	19.4(7)	$19/2^+$	$17/2^+$	0.40 (2)	-	$M1/E2$
1381.3	1126.5	254.8*	7.6(3)	$19/2^+$	$17/2^+$	0.54 (2)	-	$M1/E2$
1954.8	1381.3	573.5*	6.7(2)	$23/2^+$	$19/2^+$	0.73 (2)	-	$E2$
1954.8	1287.0	667.6*	4.0(2)	$23/2^+$	$21/2^+$	0.27 (4)	-	$M1/E2$
2592.8	1954.8	638.0*	2.2(2)	$27/2^+$	$23/2^+$	0.76 (2)	-	$E2$
2592.8	1825.8	767.0*	1.8(2)	$27/2^+$	$25/2^+$	0.41 (3)	-	$M1/E2$
3293.6	2592.8	700.8*	1.9(8)	$31/2^+$	$27/2^+$	0.92 (2)	-	$E2$
3293.6	2442.9	850.6*	1.2(2)	$31/2^+$	$29/2^+$	-	-	$M1/E2$
Band 11								
1126.5	419.0	707.5*	20.6(7)	$17/2^+$	$13/2^+$	0.86 (2)	-	$E2$
1126.5	617.8	508.5*	44.8(14)	$17/2^+$	$15/2^+$	0.26 (2)	-	$M1/E2$
1126.5	894.2	232.2*	10.3(3)	$17/2^+$	$15/2^+$	0.34 (2)	-	$M1/E2$
1126.5	818.4	308.1*	5.1(2)	$17/2^+$	$17/2^+$	0.37 (2)	-	$M1/E2$
1646.5	818.4	828.2*	2.9(2)	$21/2^+$	$17/2^+$	0.77 (2)	-	$E2$
1646.5	1126.5	520.0*	8.0(3)	$21/2^+$	$17/2^+$	0.71 (4)	-	$E2$
1646.5	1287.0	(359.5)*	3.0(2)	$21/2^+$	$21/2^+$	-	-	$M1/E2$
1646.5	1381.3	265.4*	5.4(2)	$21/2^+$	$19/2^+$	0.35 (3)	-	$M1/E2$
2241.3	1646.5	594.8*	8.1(3)	$25/2^+$	$21/2^+$	0.74 (2)	-	$E2$
2241.3	1287.0	954.1*	1.0 (2)	$25/2^+$	$21/2^+$	0.93 (9)	-	$E2$
2936.8	2241.3	695.5*	3.0(2)	$29/2^+$	$25/2^+$	0.72 (5)	-	$E2$
2936.8	1825.8	(1110.8)*	0.6(1)	$29/2^+$	$25/2^+$	-	-	$E2$
3672.8	2936.8	(736.0)*	0.6(1)	$(33/2^+)$	$29/2^+$	-	-	$E2$
Bands 12 & 13								
556.9	100.5	456.5	0.7(9)	$(9/2^+)$	$7/2^-$	-	-	-
556.9	257.1	299.7	1.7(3)	$(9/2^+)$	$11/2^+$	-	-	$M1$
910.0	556.9	353.1*	1.4(12)	$(13/2^+)$	$(9/2^+)$	-	-	-
727.4	419.0	308.4	6.1(5)	$(11/2^+)$	$13/2^+$	-	-	-
727.4	556.9	171.0	1.0(10)	$(11/2^+)$	$(9/2^+)$	-	-	-
1146.9	727.4	419.5*	1.2(11)	$(15/2^+)$	$(11/2^+)$	-	-	-

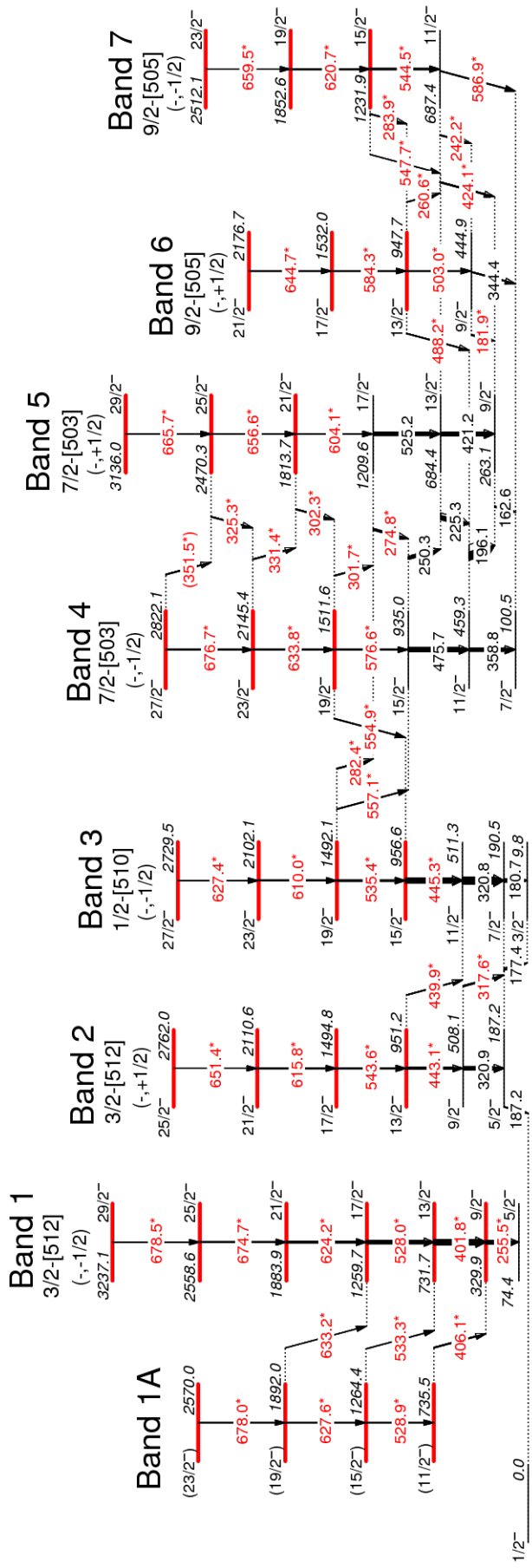

FIGURE 4.1: Partial level scheme of ^{187}Os deduced from the current work showing the negative-parity bands. New transitions are labelled in red while previously known transitions are labelled in black. Proposed configurations for each band structure are given above the bands.

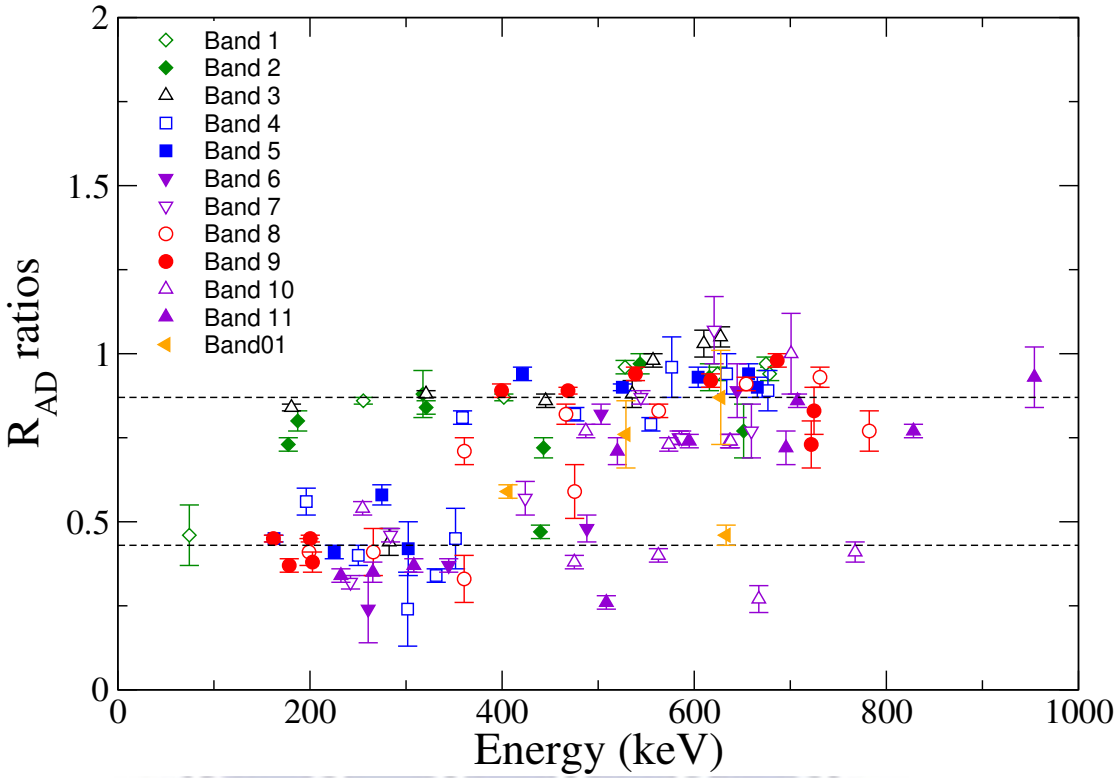

FIGURE 4.2: Angular distribution ratios as a function of energy deduced from the current work. The angular distribution ratio gives a value of ∼0.87 for stretched quadrupole and ∼0.43 for stretched dipole.

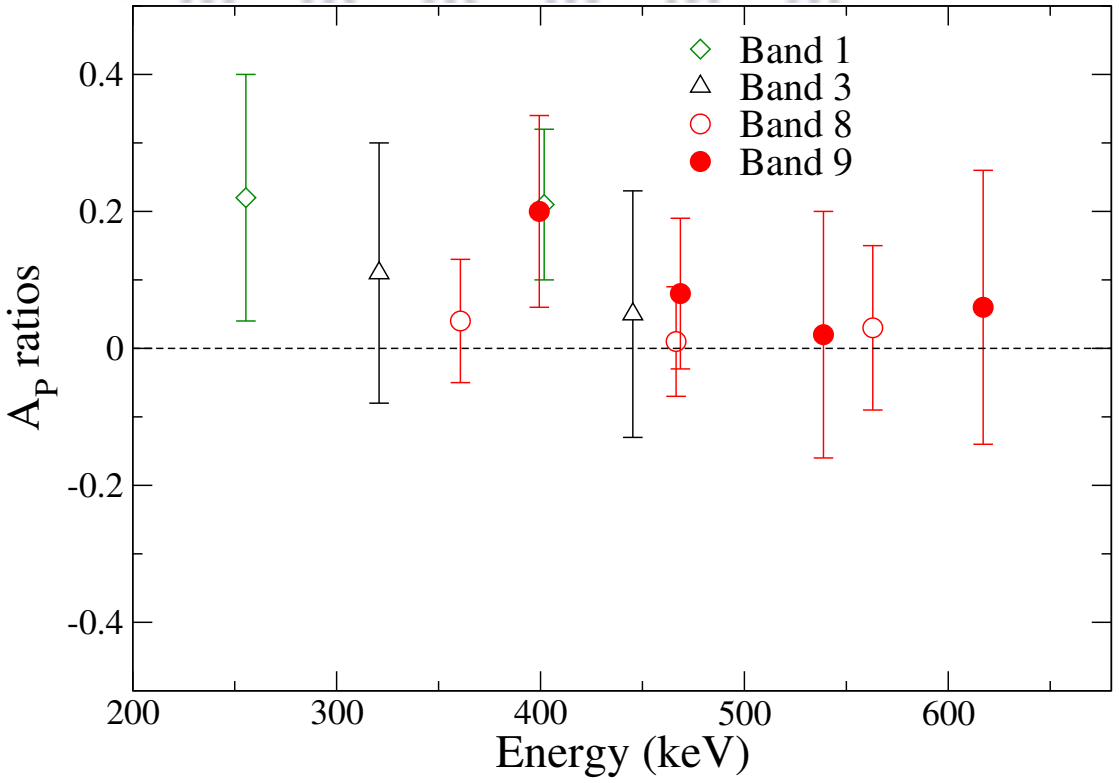

FIGURE 4.3: Plot for polarization anisotropy measurements as a function of energy deduced from the current work.

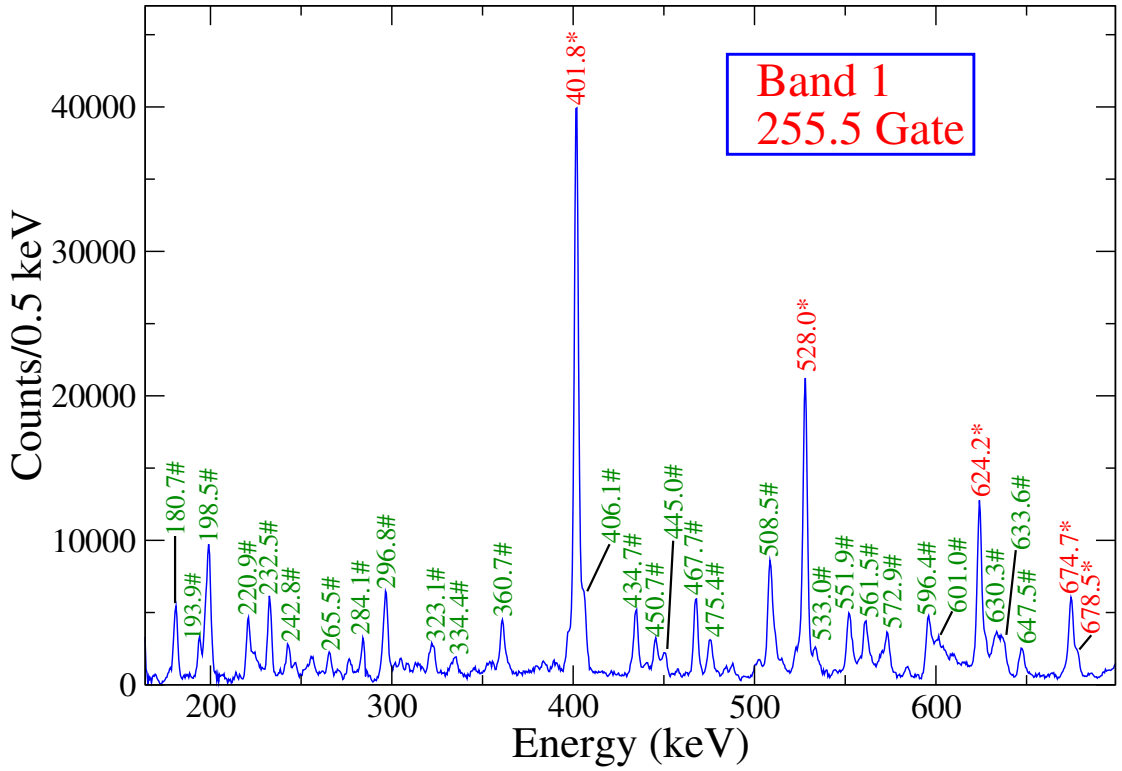

FIGURE 4.4: Coincidence spectrum obtained by setting a gate on the 255.5-keV transition of band 1. New transitions are shown in red and denoted by asterisk (*), while contaminants and other transitions of ^{187}Os not associated with the band of interest, are shown in green and labelled by a hash (#) symbol.

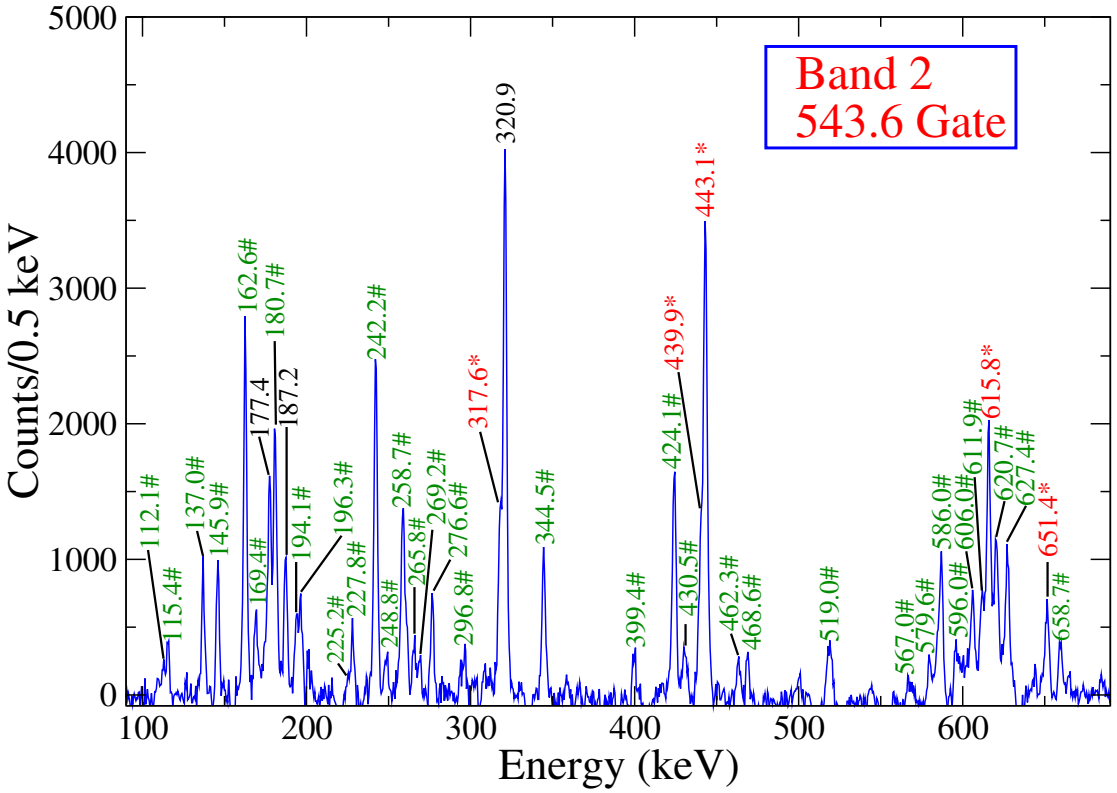

FIGURE 4.5: Coincidence spectrum obtained by setting a gate on the 543.6-keV transition of band 2. New transitions are shown in red and denoted by asterisk (*), while contaminants and other transitions of ^{187}Os not associated with the band of interest, are shown in green and labelled by a hash (#) symbol. The known transitions associated with the band of interest are shown in black.

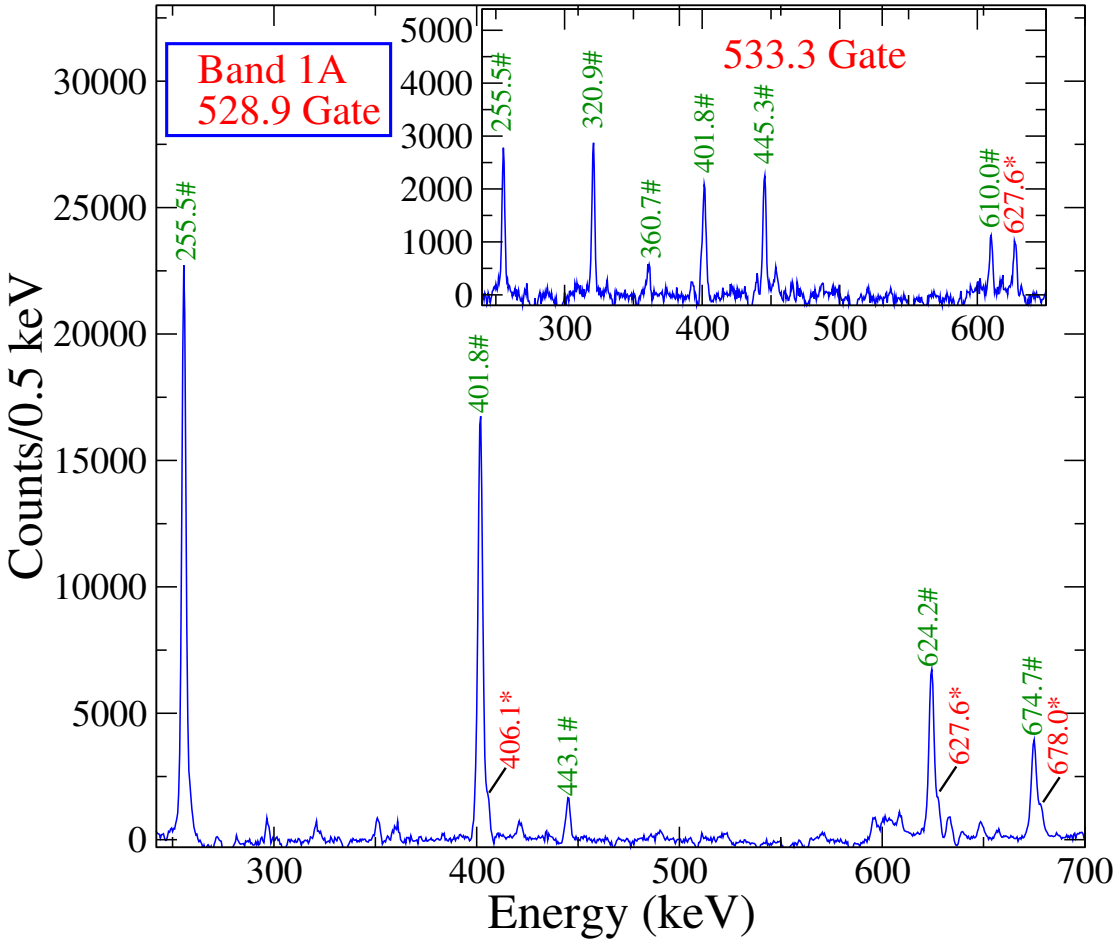

FIGURE 4.6: Coincidence spectrum obtained by setting a gate on the 528.9-keV transition of band 1A. New transitions are shown in red and denoted by asterisk (*), while contaminants and other transitions of ^{187}Os not associated with the band of interest, are shown in green and labelled by a hash (#) symbol. The inset shows a spectrum gated on the 533.3-keV transition to validate the existence of this band.

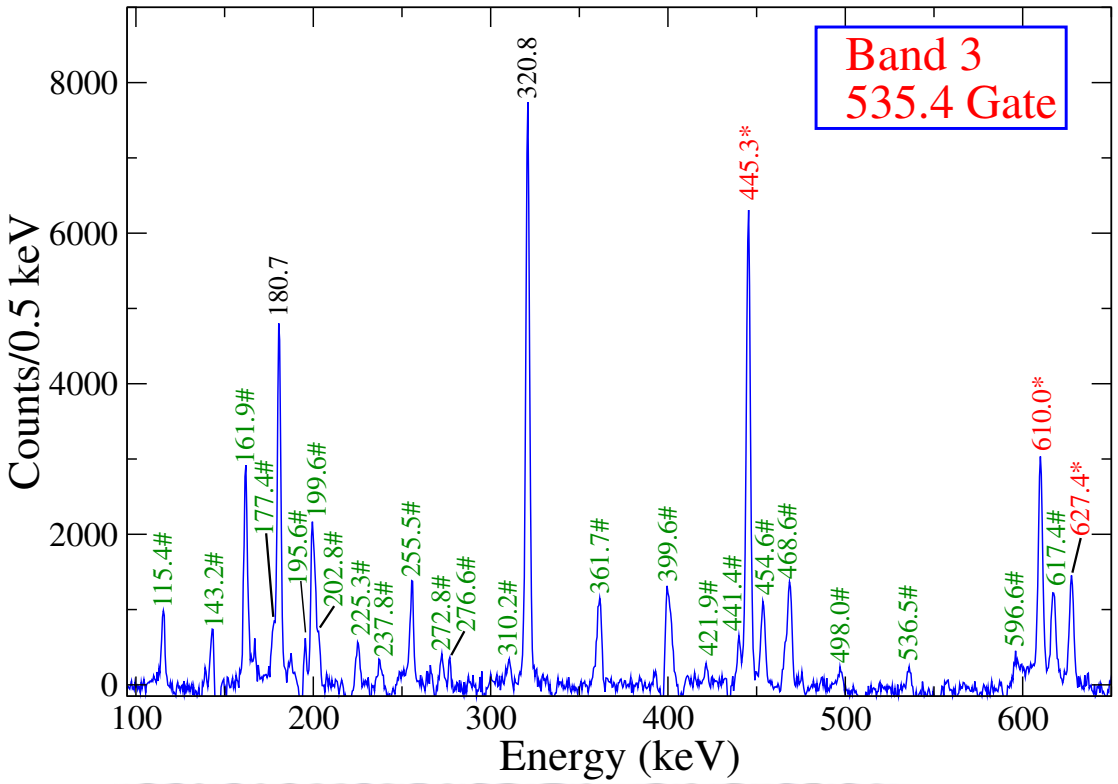

FIGURE 4.7: Coincidence spectrum obtained by setting a gate on the 535.4- keV transition of band 3. New transitions are shown in red and denoted by asterisk (*), while contaminants and other transitions of ^{187}Os not associated with the band of interest, are shown in green and labelled by a hash (#) symbol. The known transitions associated with the band of interest are shown in black.

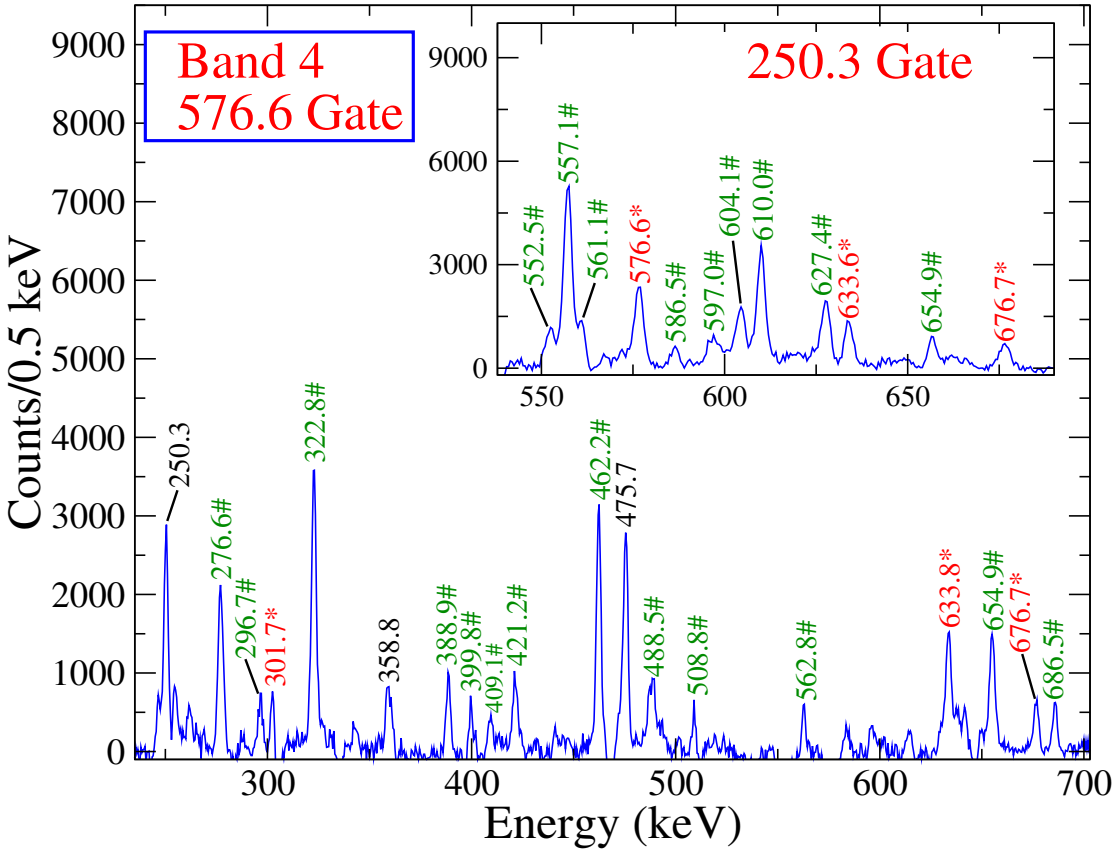

FIGURE 4.8: Coincidence spectrum obtained by setting a gate on the 576.6-keV transition of band 4. New transitions are shown in red and denoted by asterisk (*), while contaminants and other transitions of ^{187}Os not associated with the band of interest, are shown in green and labelled by a hash (#) symbol. The known transitions associated with the band of interest are shown in black. The inset shows a spectrum gated on the 250.3-keV transition to illustrate the new 576.6-keV γ-ray.

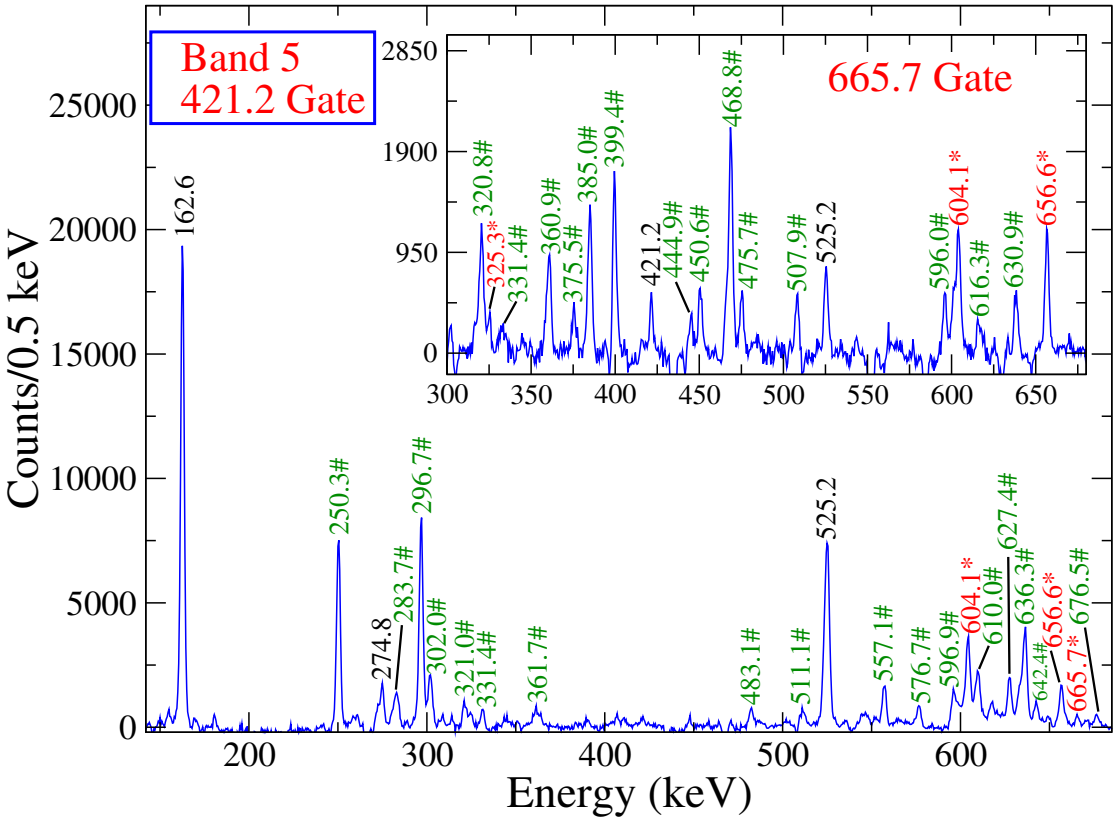

FIGURE 4.9: Coincidence spectrum obtained by setting a gate on the 421.2-keV transition of band 5. New transitions are shown in red and denoted by asterisk (*), while contaminants and other transitions of ^{187}Os not associated with the band of interest, are shown in green and labelled by a hash (#) symbol. The known transitions associated with the band of interest are shown in black. The inset shows a spectrum gated on the 665.7-keV transition to illustrate the new 604.1- and 656.6-keV γ-ray.

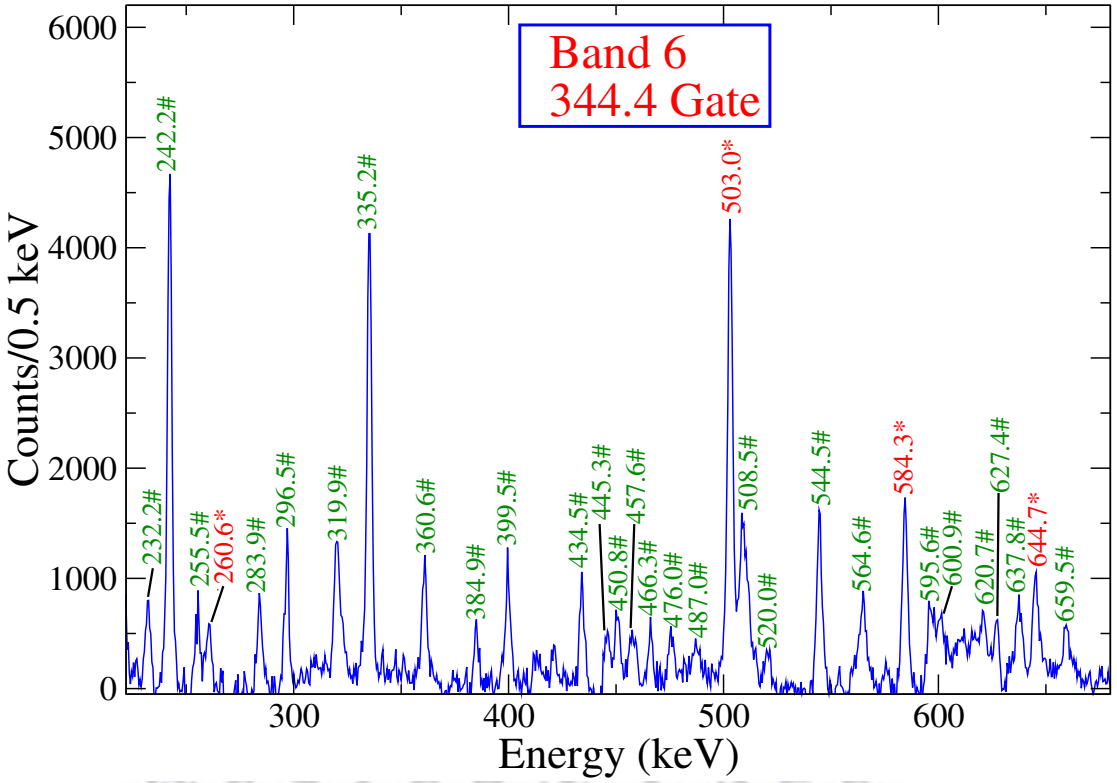

FIGURE 4.10: Coincidence spectrum obtained by setting a gate on the 344.5-keV transition of band 6. New transitions are shown in red and denoted by asterisk (*), while contaminants and other transitions of ^{187}Os not associated with the band of interest, are shown in green and labelled by a hash (#) symbol.

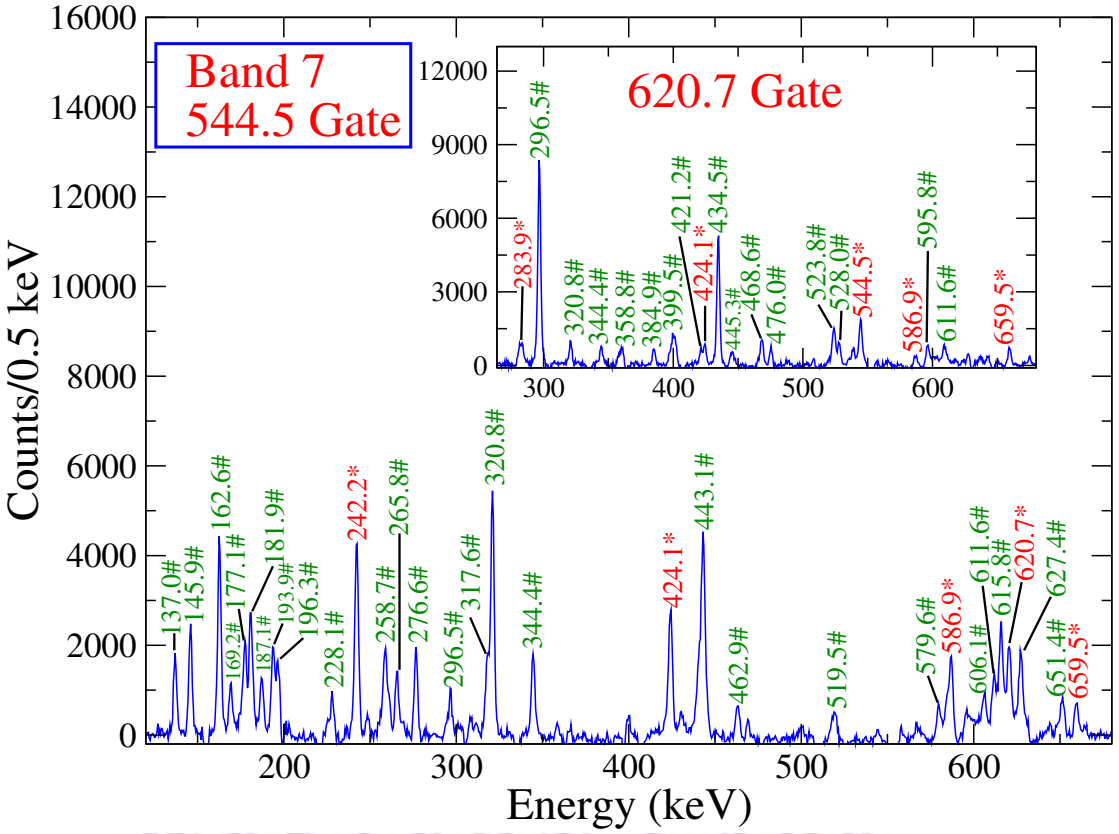

FIGURE 4.11: Coincidence spectrum obtained by setting a gate on the 544.5-keV transition of band 7. New transitions are shown in red and denoted by asterisk (*), while contaminants and other transitions of ^{187}Os not associated with the band of interest, are shown in green and labelled by a hash (#) symbol. The known transitions associated with the band of interest are shown in black. The inset shows a spectrum gated on the 620.7-keV transition to illustrate the new 544.5- and 283.9-keV γ-rays.

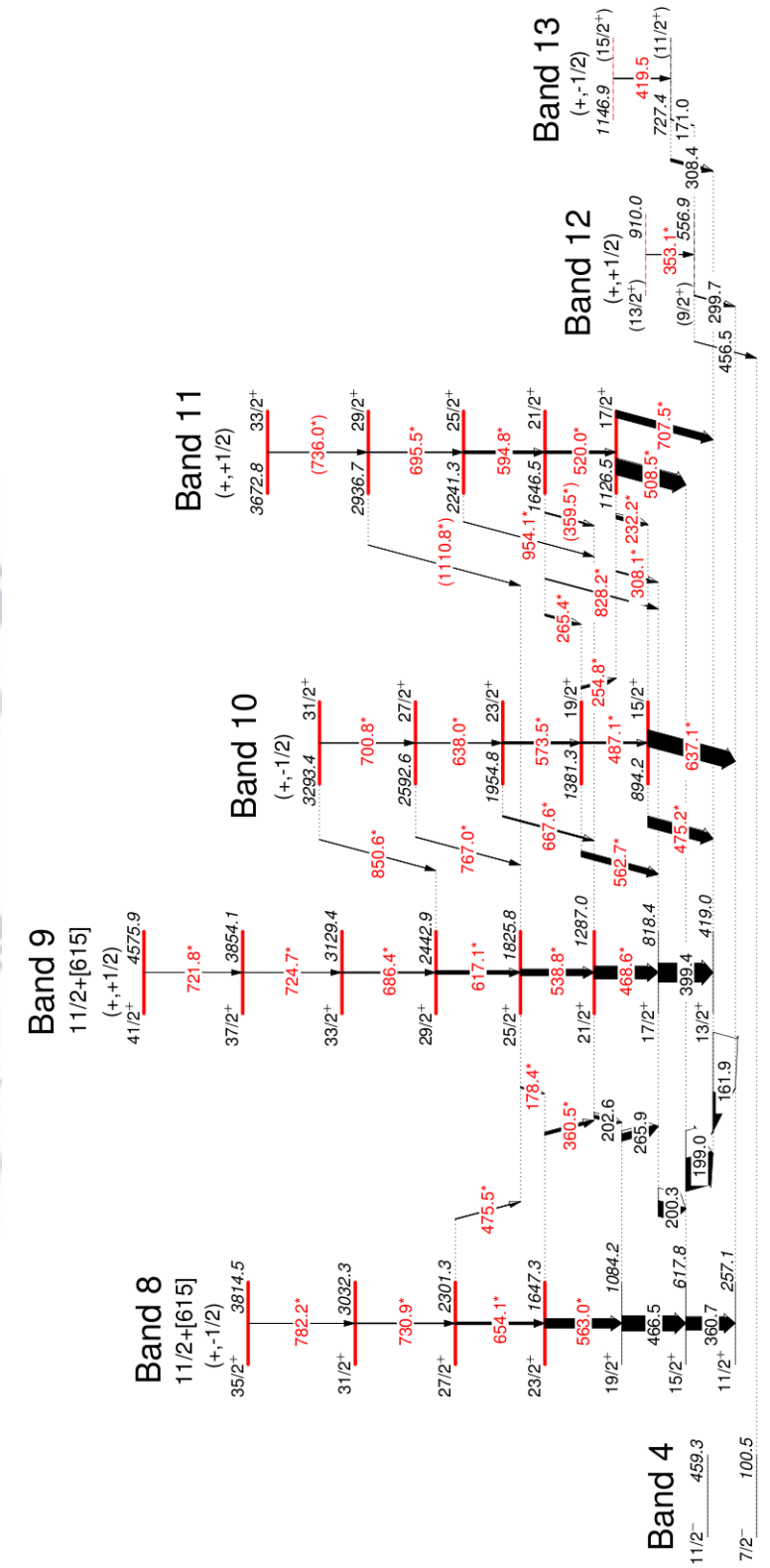

FIGURE 4.12: Partial level scheme of ^{187}Os deduced from the current work showing the positive-parity bands. New transitions are labelled in red and asterisk (*) symbol while previously known transitions are labelled in black.

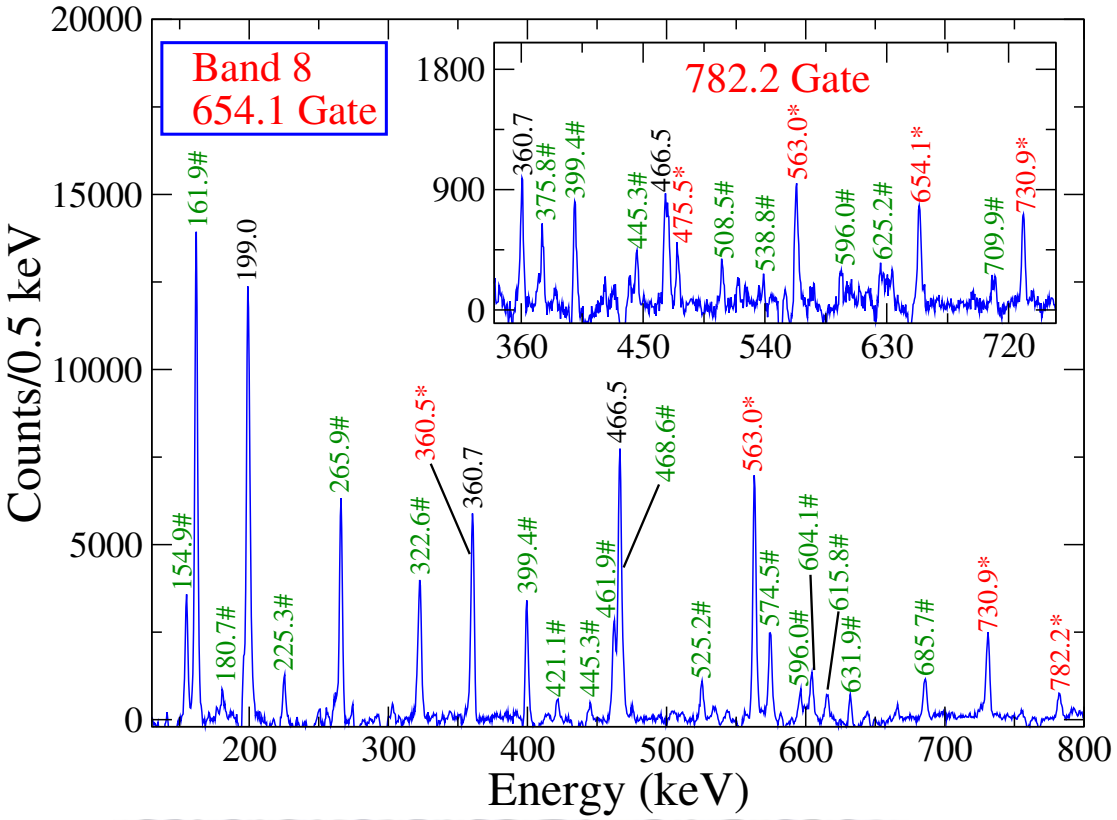

FIGURE 4.13: Coincidence spectrum obtained by setting a gate on the 654.1-keV transition of band 8. New transitions are labelled in red and asterisk (*), while contaminants and other transitions of ^{187}Os not associated with the band of interest are denoted by green and labelled by a hash (#) symbol. The known transitions associated with the band of interest are labelled in black. The spectrum gated on 782.2-keV is inserted to show the 475.5- and 654.1-keV transitions.

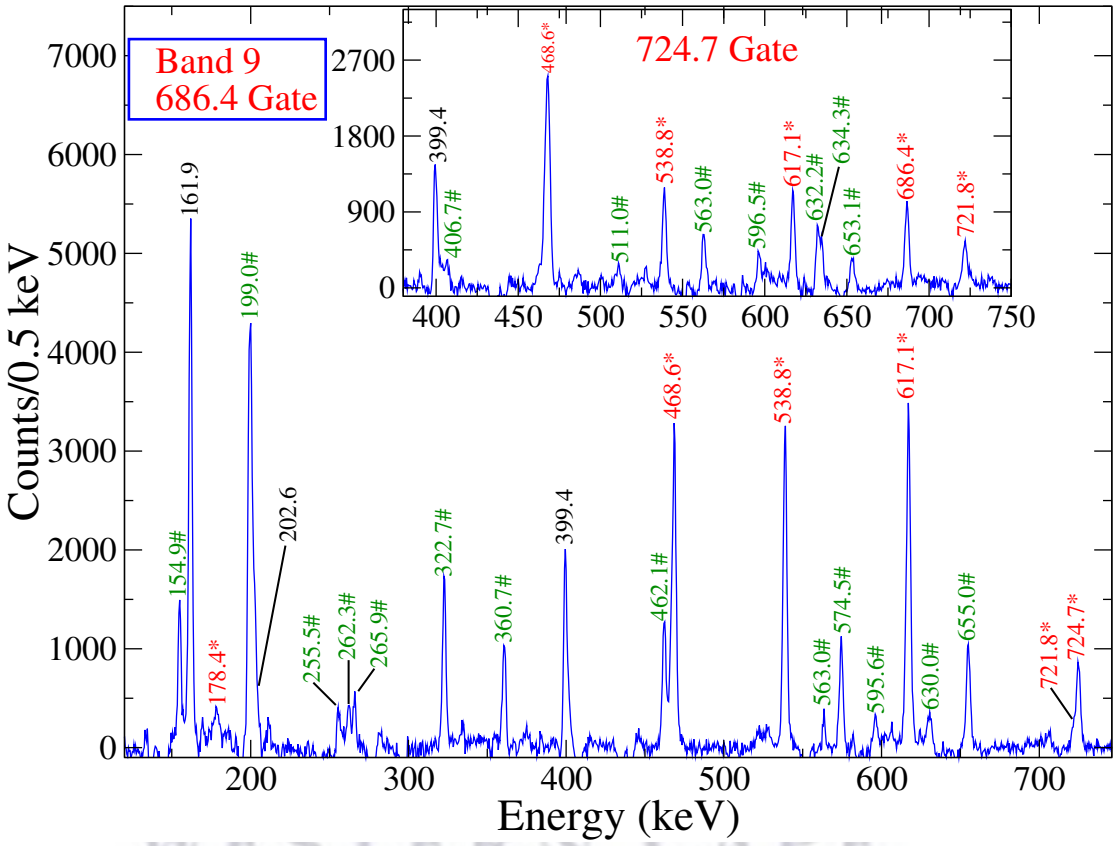

FIGURE 4.14: Coincidence spectrum obtained by setting a gate on the 686.4-keV transition of band 9. New transitions are labelled in red and asterisk (*), while contaminants and other transitions of ^{187}Os not associated with the band of interest are denoted by green and labelled by a hash (#) symbol. The known transitions associated with the band of interest are labelled in black. The spectrum gated on 724.7-keV is inserted to show the 399.4- and 686.4-keV transitions.

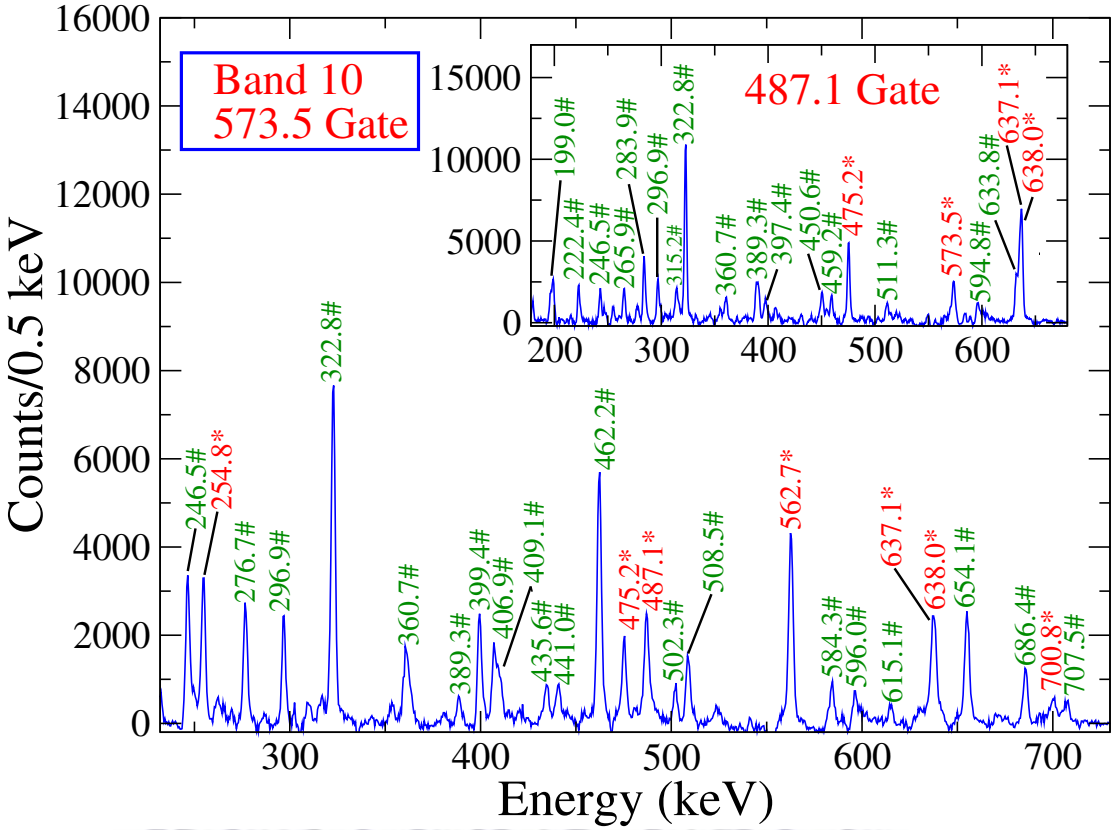

FIGURE 4.15: Coincidence spectrum obtained by setting a gate on the 573.5-keV transition of band 10. New transitions are labelled in red and asterisk (*), while contaminants and other transitions of ^{187}Os not associated with the band of interest are denoted by green and labelled by a hash (#) symbol. The spectrum gated on 487.1-keV is inserted to show the 573.5-keV transition.

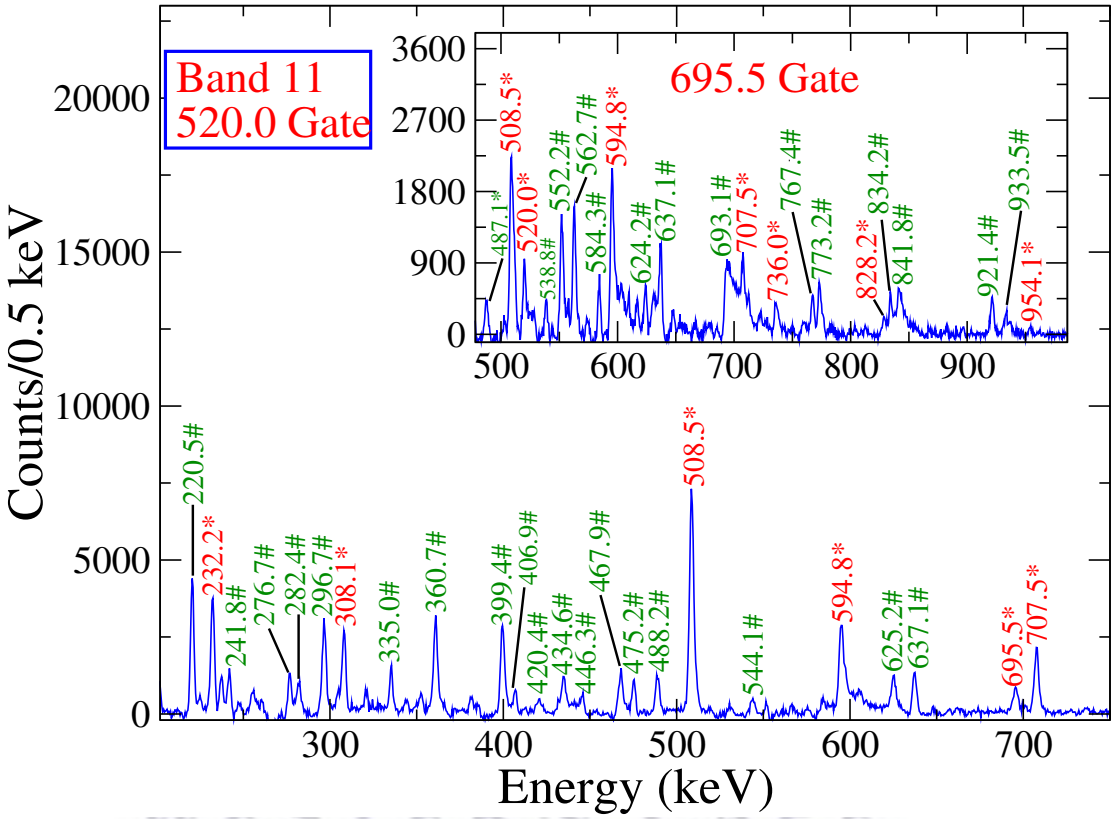

FIGURE 4.16: Coincidence spectrum obtained by setting a gate on the 520.0-keV transition of band 11. New transitions are labelled in red and asterisk (*), while contaminants and other transitions of ^{187}Os not associated with the band of interest are denoted by green and labelled by a hash (#) symbol. The spectrum gated on 695.5-keV is inserted to show the 487.1-, 520.0-, 736.0-, 828.2- and 954.1-keV transitions.

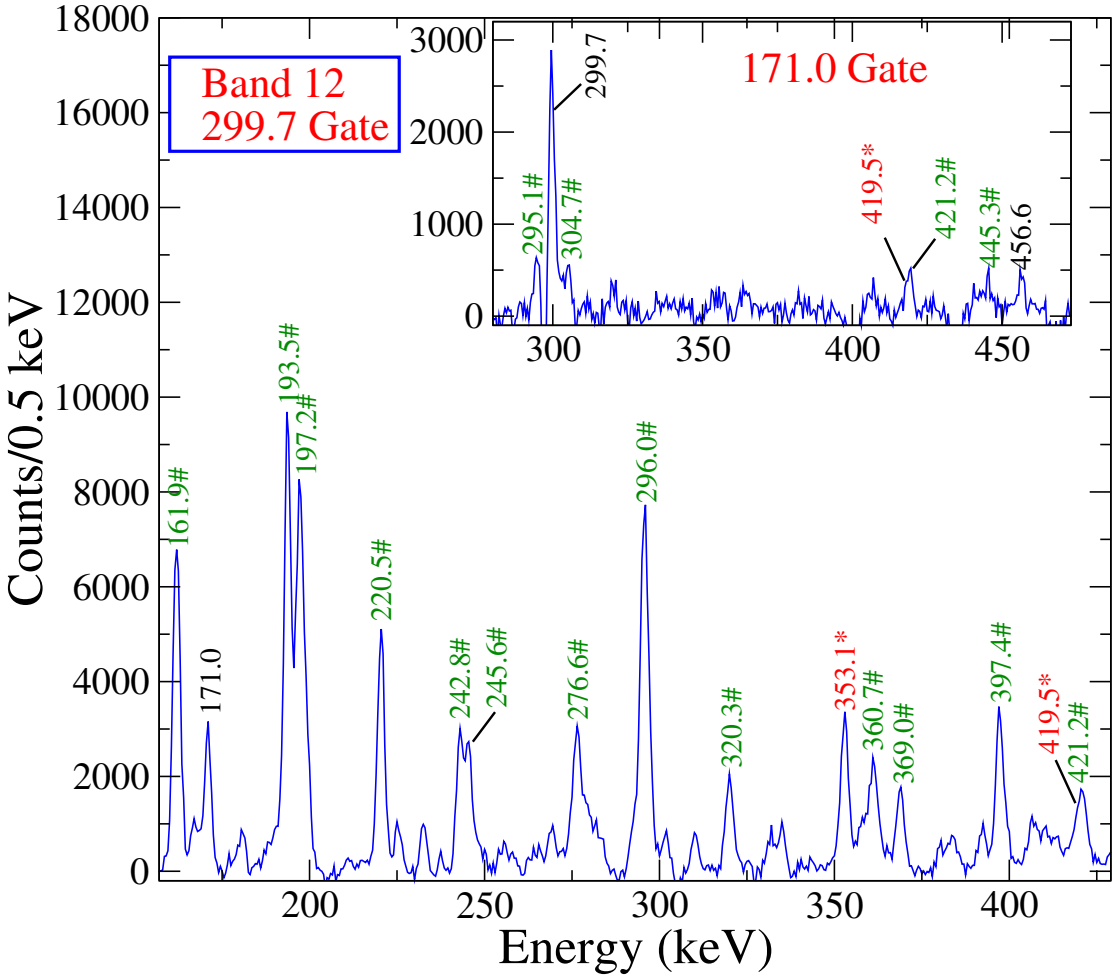

FIGURE 4.17: Coincidence spectrum obtained by setting a gate on the 299.7-keV transition of band 12. New transitions are shown in red and denoted by asterisk (*), while contaminants and other transitions of ^{187}Os not associated with the band of interest, are shown in green and labelled by a hash (#) symbol. The known transitions associated with the band of interest are shown in black. The inset shows a spectrum gated on the 171.0-keV transition to illustrate the known 299.7- and 456.6-keV γ-rays.

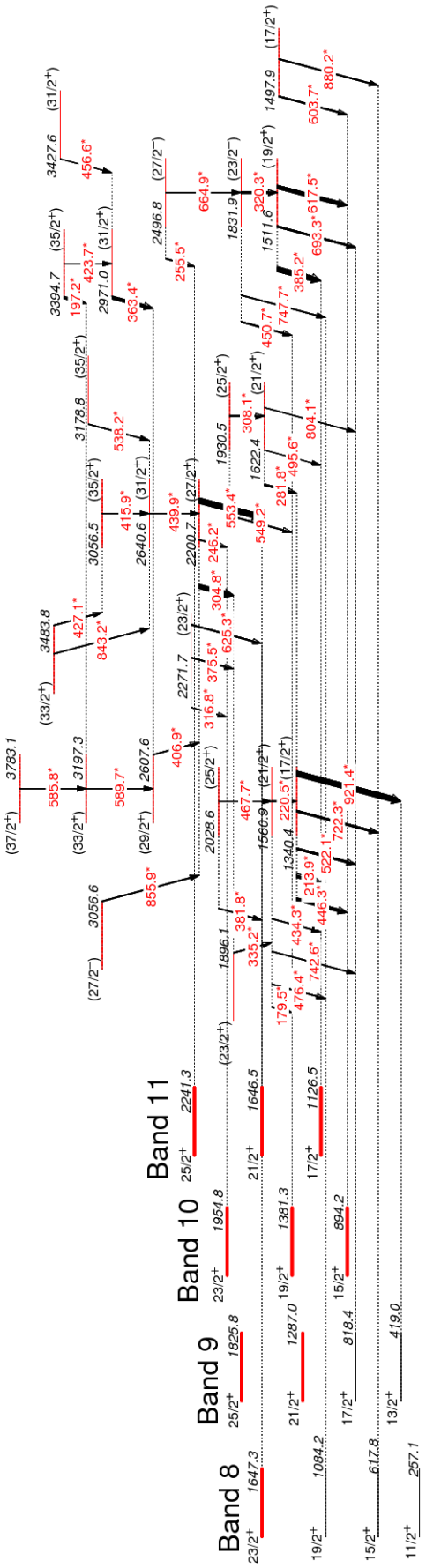

FIGURE 4.18: Partial level scheme of ^{187}Os deduced in the current work showing other states in ^{187}Os that were not grouped in bands. New transitions are labelled in red and asterisk (*) symbol.

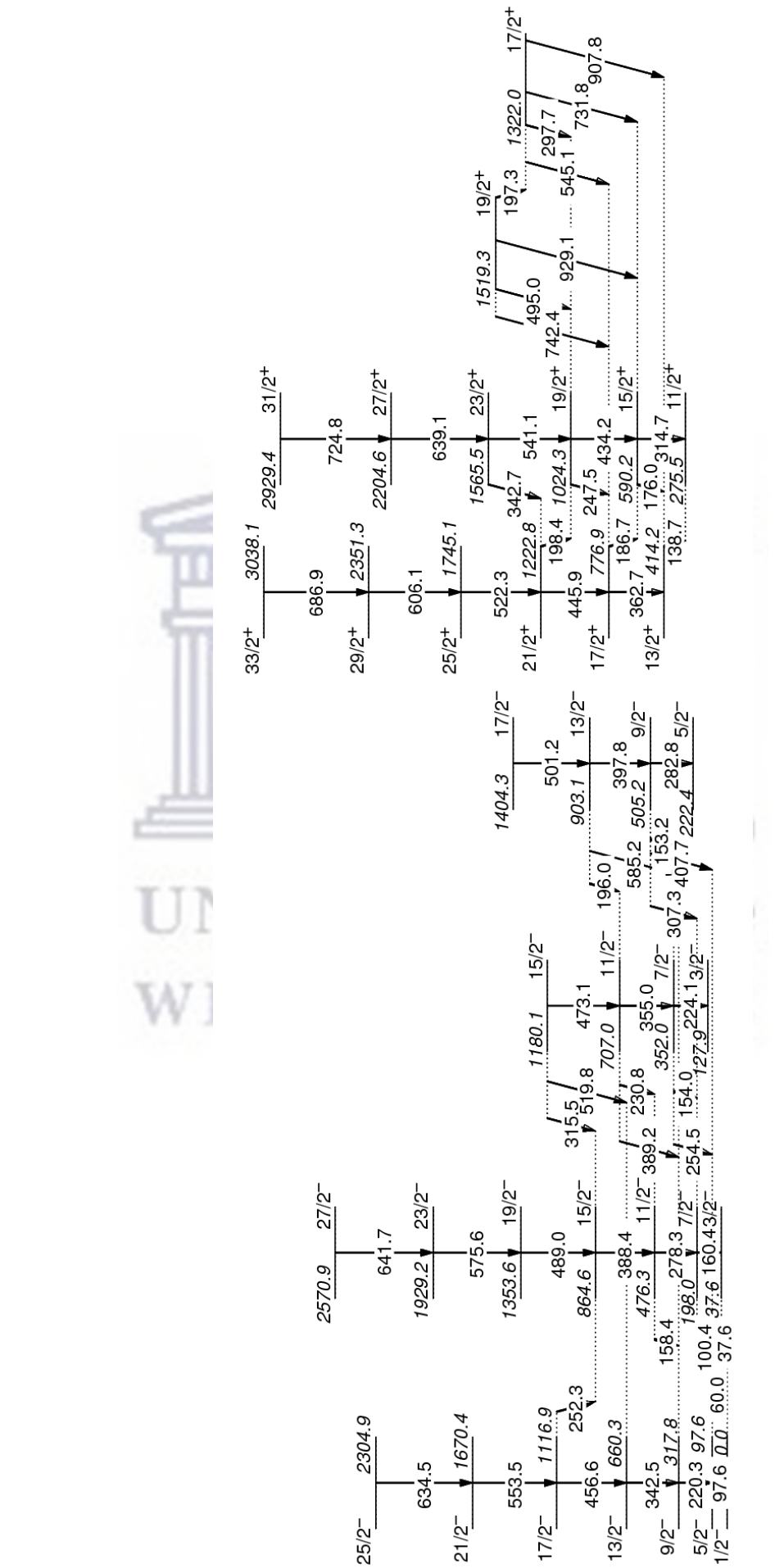

FIGURE 4.19: Partial level scheme of ^{185}Os deduced in the current work.

FIGURE 4.20: Partial level scheme of ^{186}Os deduced in the current work.

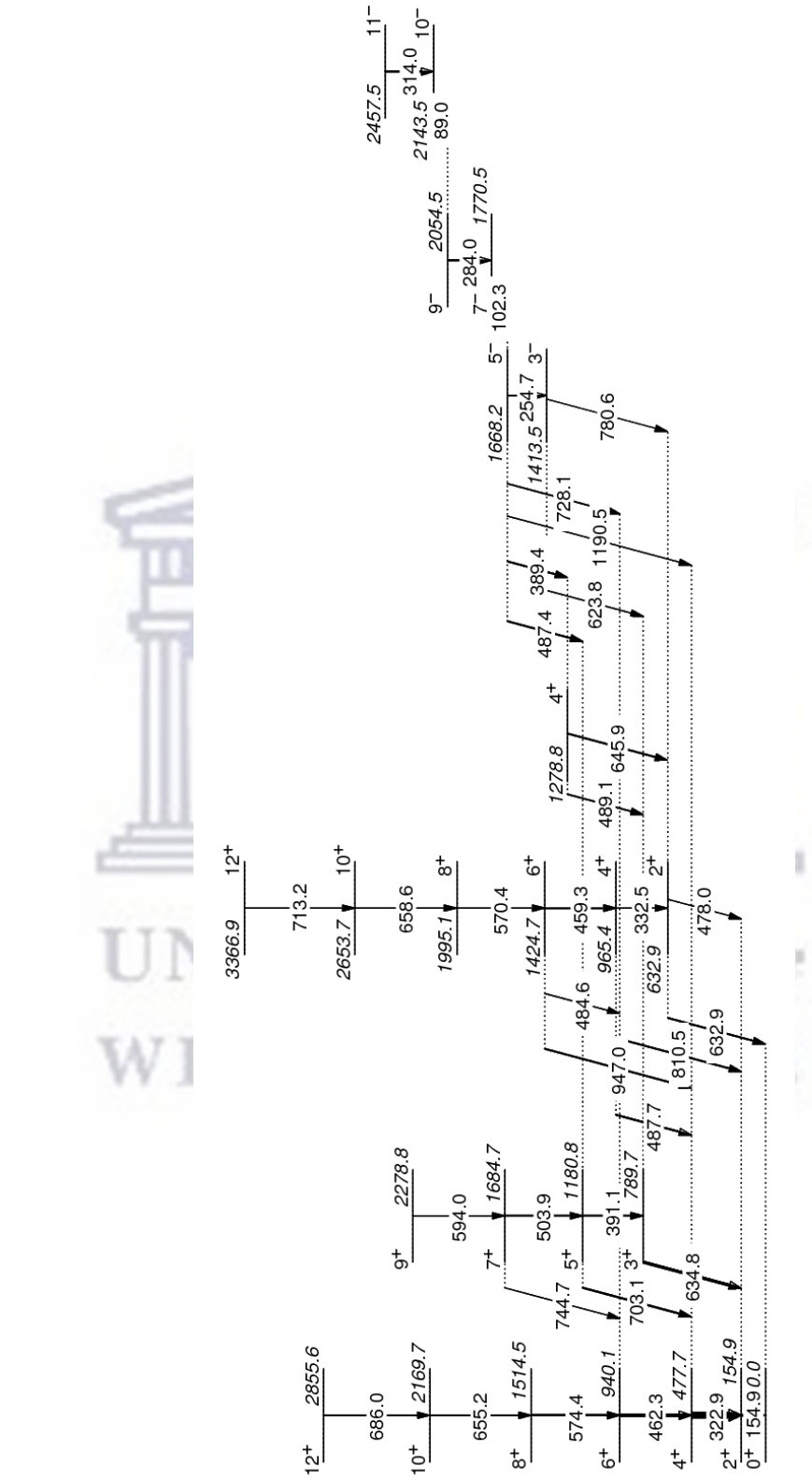

FIGURE 4.21: Partial level scheme of ^{188}Os deduced in the current work.

Chapter 5

Discussion

In order to understand the structure of the newly observed rotational bands in ^{187}Os, four different approaches were used, which are: systematic comparison with the neighboring odd-N isotopes, cranked shell model (CSM), Cranked Nilsson-Strutinsky-Bogoliubov (CNSB) formalism, and quasiparticle-plus-triaxial-rotor model. This chapter seeks to give an insight on how these models were used to explain the microscopic structures of band structures observed in the current work.

5.1 Negative-parity bands in ^{187}Os

5.1.1 Configurations

Band 1 has been reported in numerous studies of ^{187}Os [7, 29–36, 100] and has been assigned to the ground state configuration while band 3 is built on the well-known 74.4 keV level, [7]. The excitation energy of the negative-parity bands in ^{185}Os and ^{187}Os with respect to a rigid rotor are shown in Fig. 5.1. The quasiparticle alignments and Routhians calculated for these bands with Harris parameter of $J_0 = 21\hbar^2$ MeV^{-1} and $J_1 = 65\hbar^4$ MeV^{-3} for ^{187}Os and $J_0 = 24\hbar^2$ MeV^{-1} and $J_1 = 66\hbar^4$ MeV^{-3} for ^{185}Os [13] are shown in Figs. 5.2 and 5.3. In these figures, band 1 seems to track band 2 over the observed frequency range. This is consistent with these bands being signature partners built on the same configuration. For instance, the excitation energies for these bands shown in Fig. 5.1 show very similar trends, the measured alignment of $0.22\hbar$ for the bands in ^{187}Os is similar to the alignment of $0.23\hbar$ for the bands in ^{185}Os (see Fig. 5.2) and the Routhians for these bands shown in Fig. 5.3 look very similar as well. Therefore, bands 1 and 2 are most likely associated with the negative and positive signatures of the 3/2[512] Nilsson configuration, respectively.

The excitation energy, the alignment, and the Routhian for band 3 in ^{187}Os are plotted in Figs. 5.1(a), 5.2(a), and 5.3(a). They look very similar to those of the 1/2[510](−,−1/2) band in ^{185}Os, see Figs. 5.1(b), 5.2(b), and 5.3(b). For instance, the excitation energy follows a similar trend for both nuclei, an alignment of about $1\hbar$ is measured for both bands (see Fig. 5.2), and the Routhians for these bands look similar and lie at lowest energy with respect to the other bands (see Fig. 5.3). We also compare this band with the one predicted by the cranked shell model (more details are given in section 5.1.1 and see Fig. 5.4) and a good agreement is obtained. Therefore we suggest that this band is assigned to the 1/2[510](−,−1/2) Nilsson configuration. It should be noted that in the previous works band 2 was assigned to the ground-state configuration and thus to the 1/2[510](−,−1/2) configuration [7, 29–36, 100], while band 3 was assigned to the 3/2[512](−,−1/2) configuration [7, 29–36, 100]. It is likely that the previous works could not evaluate the behaviour of the bands at medium spins because of the limited experimental data available. They could not distinguish between the possible 1/2[510](−,−1/2) and 3/2[512](−,−1/2) configurations for these bands. The new experimental data at higher spins presented in this work allow a comparison with the bands in the neighboring ^{185}Os isotope (see Figs. 5.1, 5.2, and 5.3) and suggest that bands 2 and 3 have 3/2[512](−,−1/2) and 1/2[510](−,−1/2) natures, respectively.

The low-spin states of bands 4 and 5 were first observed by Harmatz et al. [29] who assigned them to a K = 1/2 band. A modification of these bands was done by Ewbank [100], who pointed out that the 100-keV level has been shown to have a half-life of 112 ns and thus it cannot be the $7/2^-$ member of the K = 1/2 band, and is probably a $7/2^-$[503] state. The existence of this band has been confirmed in [7, 29–36, 100]. The band head energies of both bands 4 and 5 at 100 keV and 263 keV, respectively, have been reported also from the previous in-beam work [7]. These bands were considered as signature partners associated with the $7/2^-$[503] neutron orbital. As mentioned earlier, the sequence of levels added in the present work, which allowed us to observe these bands to higher spins, show that these bands share the same moment of inertia throughout, as a function of spin, see Fig. 5.1 (a). This feature is also displayed in the alignment and Routhian plots shown in Figs. 5.2 (a) and 5.3 (a), respectively. The fact that these bands are connected by interlinking M1 transitions and track each other over the observed frequency range is evidence that these bands are signature partners built on the same configuration. In the current study these bands were compared with the ones observed in the ^{185}Os nucleus and a good agreement was achieved, see Figs. 5.1 (b), 5.2 (b) and 5.3 (b). The assignment of these bands to the 7/2[503] Nilsson configuration is also consistent with the prediction made by the cranked shell model, see Fig. 5.4. It is interesting to note that the band crossing of band 3 with bands 4 and 5 as observed in

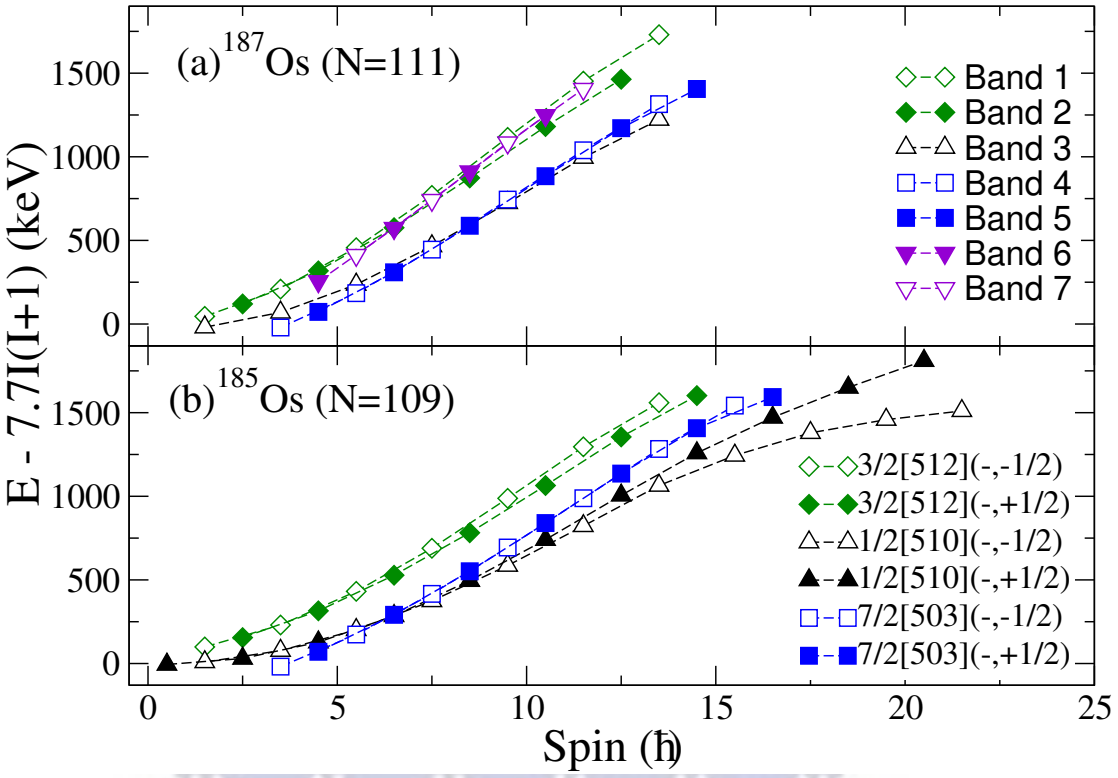

FIGURE 5.1: The experimental excitation energies with respect to rigid rotor energies for the negative-parity bands in ^{187}Os and ^{185}Os nuclei [13, 14]. The signature partner bands are labelled in the same colour, open symbols denote negative signature, closed symbols represent positive signature and (-, -1/2) or (-, +1/2) represent (parity, signature), respectively.

^{187}Os was also found in ^{185}Os, see Fig. 5.1. This highlights further the similar behavior of these bands in the two neighboring nuclei.

The band-head levels of bands 6 and 7 were first observed by Sodan et al., [7], who assigned them to a K = 9/2 band. The sequence of levels added in the current work, which allowed us to observe these bands to higher spins, show that these bands share the same moment of inertia throughout, as a function of spin, see Fig. 5.1 (a). This feature is also displayed in the alignment and Routhian plots, shown in Figs. 5.2 (a) and 5.3 (a), respectively. The bands show no signature splitting (see Fig. 5.1 (a)), which is consistent with a band associated with a neutron configuration with large Ω. This behavior is consistent with the similar bands observed in the A = 160 mass region [26]. Therefore, these bands are assigned as signature partners and associated with the 9/2[505] Nilsson configuration.

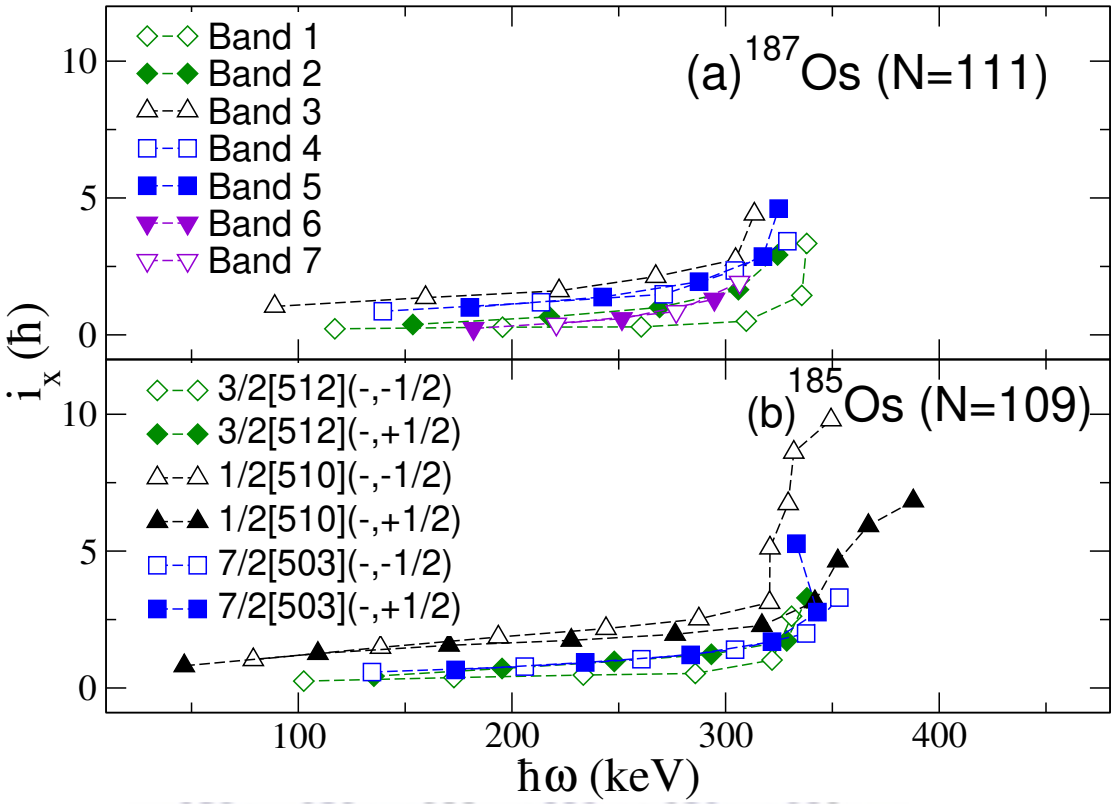

FIGURE 5.2: Aligned angular momentum i_x deduced for the negative-parity bands in ^{187}Os and ^{185}Os as a function of the rotational frequency. The Harris parameters are: $J_0 = 21\hbar^2$ MeV^{-1} and $J_1 = 65\hbar^4$ MeV^{-3} for ^{187}Os and $J_0 = 24\hbar^2$ MeV^{-1} and $J_1 = 66\hbar^4$ MeV^{-3} for ^{185}Os [13].

5.1.2 Cranked Shell Model

We further compare these bands with those predicted by the cranked shell model in Fig. 5.4. The calculations in Fig. 5.4 were carried out with the parameters for ^{186}Os as given in Ref. [62] of $\epsilon_2 = 0.198$, $\epsilon_4 = 0.054$, $\Delta = 0.094$, $\lambda = 6.837$, Z = 76, and N = 110. The cranked shell calculations suggest that the negative-parity Routhian with the lowest energy is associated with the $1/2^-[510]$ Nilsson configuration, the second lowest with the $7/2^-[503]$ configuration, the third with the $3/2^-[512]$ configuration, and the highest energy one with the $9/2^-[505]$ configuration, which is in exact agreement with the relative energy of the experimental Routhians of the bands in ^{185}Os and ^{187}Os, shown in Fig. 5.3. The calculations predict small signature splitting for the $7/2^-[503]$ and $3/2^-[512]$ Routhians with the negative and positive signatures being favored for these configurations, respectively. This is also in good agreement with the experimental observations. The calculated lack of signature splitting for the $9/2^-[505]$ orbital is also in agreement with the plotted experimental Routhians of bands 6 and 7 in Fig. 5.3(a). The excellent agreement of the CSM calculations with the experimental data lends further support for the proposed configuration assignments.

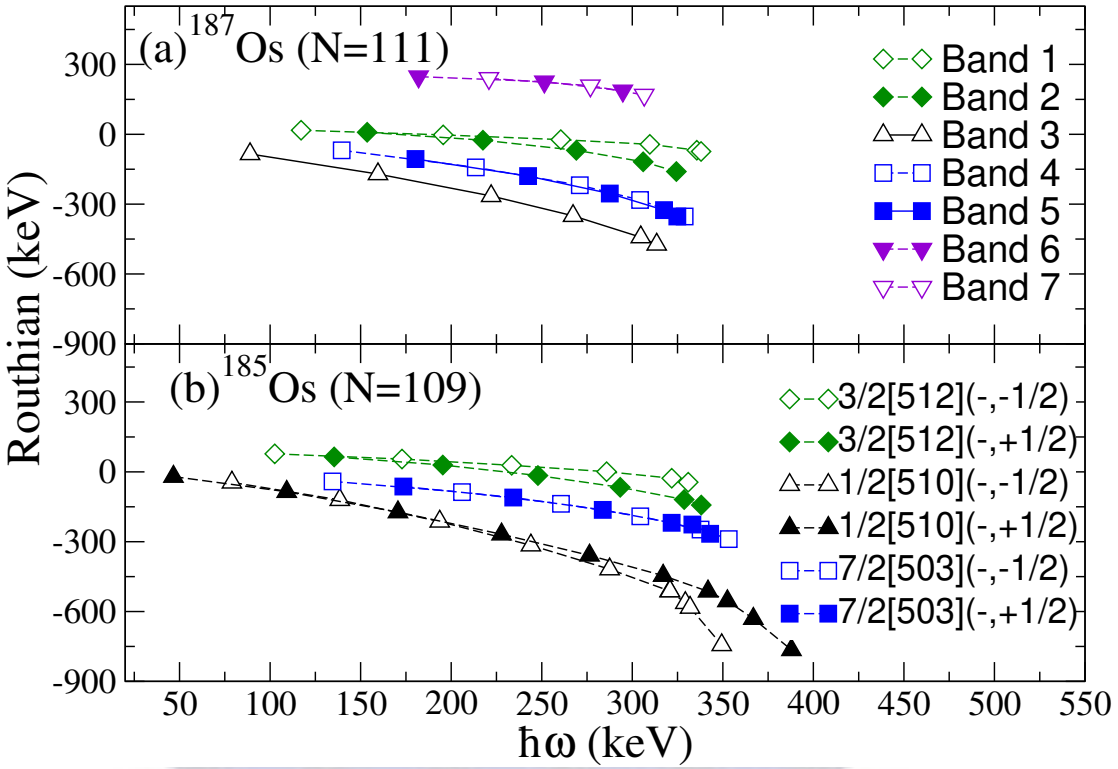

FIGURE 5.3: The experimental Routhians for the bands in ^{187}Os and ^{185}Os. The Harris parameters for ^{187}Os are: $J_0 = 21\hbar^2$ MeV^{-1} and $J_1 = 65\hbar^4$ MeV^{-3} and for ^{185}Os are: $J_0 = 24\hbar^2$ MeV^{-1} and $J_1 = 66\hbar^4$ MeV^{-3} [13]. The signature partner bands are labelled in the same colour, open symbols denote negative signature, closed symbols represent positive signature and (-, -1/2) or (-, +1/2) represent (parity, signature), respectively.

5.1.3 Cranked Nilsson-Strutinsky-Bogoliubov Formalism

Further calculations have been carried out for ^{187}Os, using the CNSB (Cranked Nilsson-Strutinsky-Bogoliubov) formalism as detailed in Refs. [66, 68, 69]. Standard parameters [84] have been used in the calculations. The quantum numbers which are preserved in the CNSB approach are parity and signature, thus, for the odd-mass Os isotopes the neutrons configurations are specified as (π,α). Representative CNSB potential energy surfaces (PES) for the yrast (+,1/2) configuration is presented in Fig. 5.10. These plots represent the potential energy minimum as a function of the spin and of the nuclear deformation of ^{187}Os. The calculated single-particle energies suggest that the negative-parity low-j orbitals in the shell N = 5, 1/2[510], 9/2[505], 3/2[512], 7/2[503], are lying near the Fermi level for N = 110. Therefore, one expects that the negative-parity bands in ^{187}Os are associated with these orbitals. In the CNSB calculations the low-j orbitals are not easily distinguishable, and therefore the labelling of the negative-parity bands in ^{187}Os uses the $(-,\pm/2)_n$ notation, where $n = 1$ denotes the lowest-energy configuration with $(-,\pm1/2)$, while $n = 2$ labels the second lowest-energy configuration, etc., see for instance, Fig. 5.5(a). The calculations suggest that the negative-parity bands have

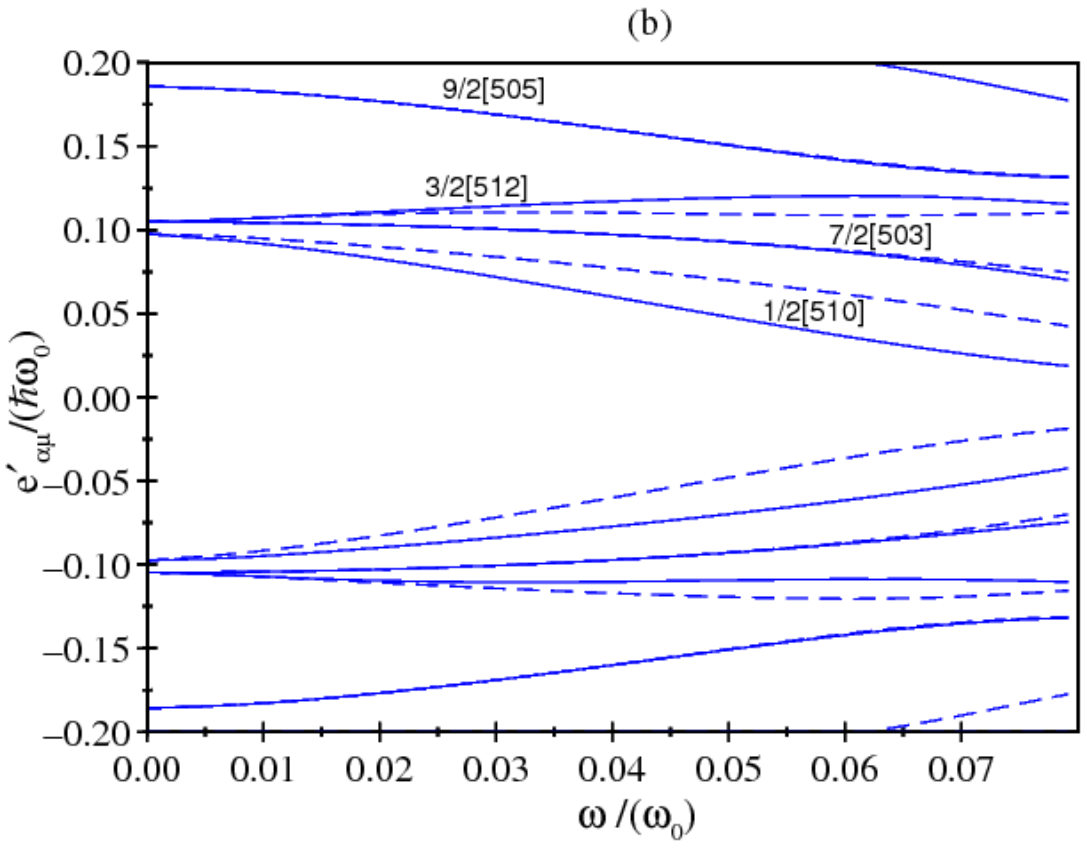

FIGURE 5.4: Cranked shell model negative-parity Routhians for ^{186}Os with N =110 as a function of the rotational frequency ω. The rotational frequency and the quasiparticle energy, are expressed in units of the harmonic oscillator energy $\hbar\omega_0$. In this figure, solid lines represent quasiparticle trajectories with negative parity and signature $\alpha = 1/2$ and dashed lines are used for quasiparticle trajectories with negative parity and signature α = -1/2.

similar but not the same moments of inertia, see Fig. 5.5(a), in agreement with the experimental data (see Fig. 5.1(a)). The calculations predict very small alignments for all three negative-parity bands (see Fig. 5.5(b)), which is also in good agreement with the experimental data (see Fig. 5.2(a)). The calculations predict an alignment of a nucleon pair at a rotational frequency of 0.30–0.35 MeV, which is also in line with the observed onset of alignment for the experimentally observed bands in Fig. 5.2(a). Therefore, the CNSB calculations are generally in good agreement with the proposed nucleon configurations.

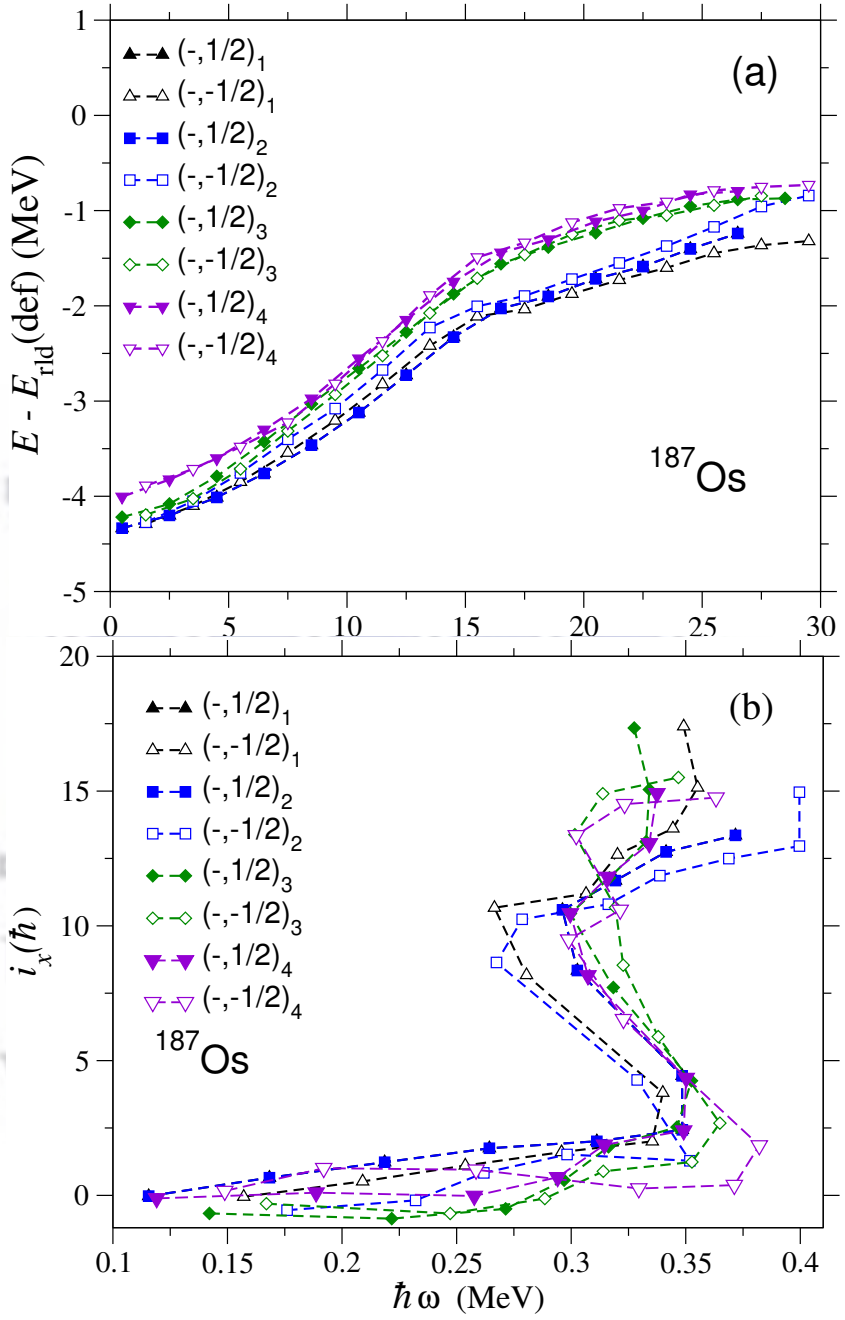

FIGURE 5.5: (a) The excitation energies with respect to a liquid-drop reference for the four lowest-energy $(-,\pm 1/2)_n$ bands of ^{187}Os calculated with the CNSB model. The index n denotes the relative energy of the bands, $n = 1$ corresponds to the yrast negative-parity band, $n = 2$ to the first excited negative-parity band, etc. (b) The alignment of the calculated negative-parity bands in ^{187}Os as a function of rotational frequency. The Harris parameters are the same as in Fig. 5.2.

5.2 Positive-parity bands in ^{187}Os

As mentioned earlier bands 8 and 9 have been previously observed up to spin-parity of $19/2^+$ and $17/2^+$ respectively, and their configuration was assigned by the previous in-beam work [7]. In the current work bands 8 and 9 were extended and two new positive-parity bands, bands 10 and 11, were identified. Bands 8 and 9 have been previously assigned as signature partner bands where the odd neutron occupies the nearest $i_{13/2}$ orbital to the Fermi level [7].

The question is, what is the underlying nature of bands 10 and 11? To answer this question, we first examine the positive parity single-particle orbitals in the Nilsson diagram, that lie near the Fermi surface. As shown in Fig. 1.2, all such orbitals (e.g. the 11/2[615] and 9/2[624]) that can be associated with these bands are already occupied. The second option is to check the possibility of exciting three quasiparticles. This option fails, because the band-head level of band 8 has an excitation energy of 894.2 keV which is too low for a 3-quasiparticle configuration.

Therefore in a quest to identify the microscopic nature of bands 10 and 11, we consider the possible couplings of the odd $i_{13/2}$ neutron with the excited collective states of the core. As illustrated in Fig. 1.2, the lowest collective excitation in the even-even Os isotopes is the γ band. The excitation energies of the ground-state and the γ bands in the even-even $^{182-188}$Os isotopes with respect to a rigid rotor reference are shown in Fig. 5.6. As mentioned earlier the excitation energies of the γ band decrease for the heavier isotopes, this trend is observed in these even-even nuclei. We therefore plotted the excitation energies of the positive-parity bands in ^{187}Os in comparison with the excitation energies of the corresponding bands in ^{183,185}Os, to check if we can still observe the same trend as observed in the even-even isotopes. As shown in Fig. 5.7 the same trend is also observed in the odd-N nuclei. This gives us confidence, to propose that we are dealing with structures associated with coupling with the γ band.

The Fermi level for neutrons for these Os isotopes lies at the upper part of the $i_{13/2}$ sub-shell near the 9/2[624] and 11/2[615] Nilsson orbitals. The lowest-energy positive-parity band in ^{183}Os is built above a $9/2^+$ state and was associated with the 9/2[624] Nilsson orbital [15]. In ^{185}Os positive-parity bands associated with both the 9/2[624] and 11/2[615] Nilsson orbitals were observed with the latter lying at lower energy [13]. In ^{187}Os the yrast positive-parity band is based on a $11/2^+$ level and thus the band was associated with the 11/2[615] Nilsson orbital. The change can be explained as due to the raising of the Fermi level within the $i_{13/2}$ sub-shell for the heavier Os isotopes. These assignments assume that the nuclear shape is axially symmetric, and thus the projection of the total angular momentum, K, and the single-particle angular momentum Ω, on the

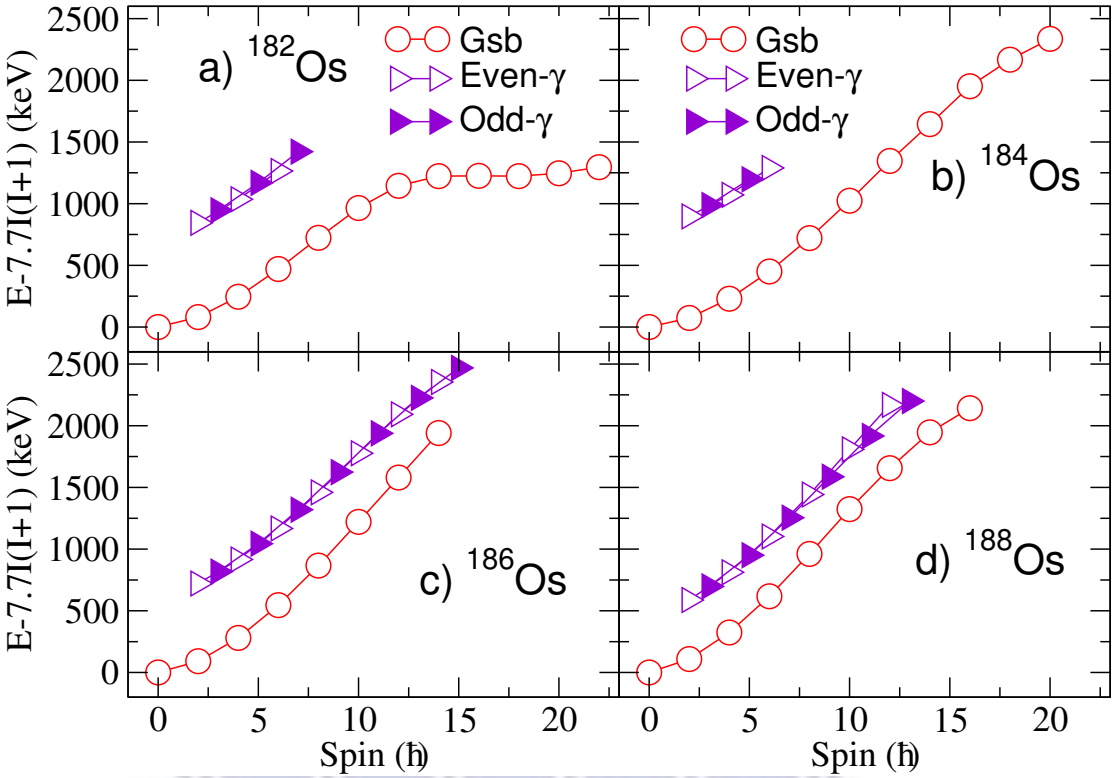

FIGURE 5.6: Compilation of the experimental excitation energies with respect to a rigid rotor reference for the ground state bands and the γ bands of ^{182}Os [1], ^{184}Os [2], ^{186}Os [3] and ^{188}Os [4]. The even- and odd-spin sequences of the γ bands are labelled with open and closed symbols, respectively, and the same colours.

long axis are conserved, and $K = \Omega$. The distinct resemblance of the excited positive-parity bands in ^{183,185}Os with the γ bands in ^{182,184}Os were interpreted as a coupling of the $i_{13/2}$ yrast band with the γ band of the core, [13, 15]. For nuclei with axially symmetric shape the γ band corresponds to a $K = 2^+$ γ vibration, thus the coupling with a Nilsson state with projection Ω can produce excited bands with $K_> = \Omega + 2$ and $K_< = \Omega$ - 2. The excited positive-parity bands in ^{183,185}Os were interpreted as a coupling with the core to give $K_>$ [13, 15]. The new bands in ^{187}Os, bands 10 and 11, follow a similar trend of the excitation energies, see Fig. 5.7, as the corresponding bands in ^{183,185}Os, thus we propose that they result from a coupling with the γ band. Such assignment is further supported by the observed trend of decreasing excitation energy of the excited positive-parity bands for the heavier Os isotopes, which is very similar to the decreasing energy trend observed for the γ bands in the corresponding cores, see Fig. 5.6. In addition bands 10 and 11 decay only to the levels of bands 8 and 9, which also supports the proposed interpretation. Fig. 5.8 shows the experimental alignments and Routhians for the positive-parity bands in ^{187}Os in comparison with the corresponding bands in the neighbouring ^{183,185}Os isotopes. They are calculated assuming $K = 9/2$ and $K = 13/2$ for the yrast (shown with circles) and the excited (shown with triangles) bands in ^{183}Os, respectively, while $K = 11/2$ and $K = 15/2$ were used for these bands

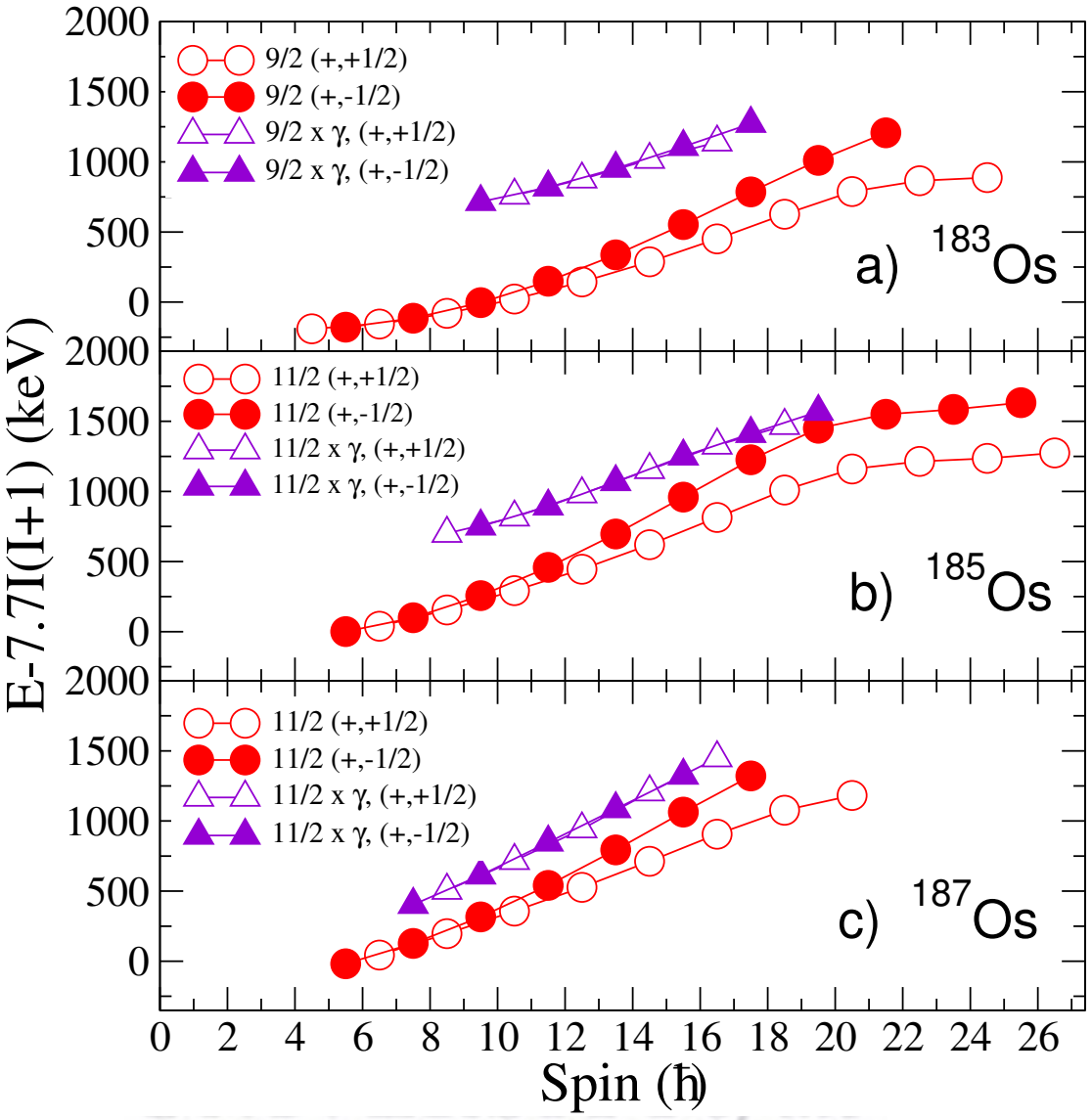

FIGURE 5.7: Experimental excitation energies relative to a rigid rotor reference for the positive-parity bands in ^{187}Os in comparison with the corresponding bands in ^{183}Os [15] and ^{185}Os [13]. The signature partner bands are labelled in the same colours. Open symbols denote positive signature and closed symbols represent negative signature.

in ^{185,187}Os. The plots highlight the similarities of the bands in the three Os isotopes. Following all presented comparisons, the new bands 10 and 11 are associated with a coupling with the γ band of the even-even core.

The yrast positive-parity band, (bands 8 and 9 in Fig. 4.12), shows a large signature splitting. In principle a single-particle configuration with a large projection Ω on the symmetry axis, such as $\Omega = 11/2$, is not expected to show signature splitting. Similar splitting was observed in the ^{183,185}Os neighbours, but was not discussed. It should also be noted that while the splitting is present for the yrast bands in ^{183,185,187}Os, it is absent for the excited bands, see Fig. 5.7. To study the signature splitting CSM calculations are shown in Fig. 5.9. The same parameters as used for ^{186}Os [62] were employed, with

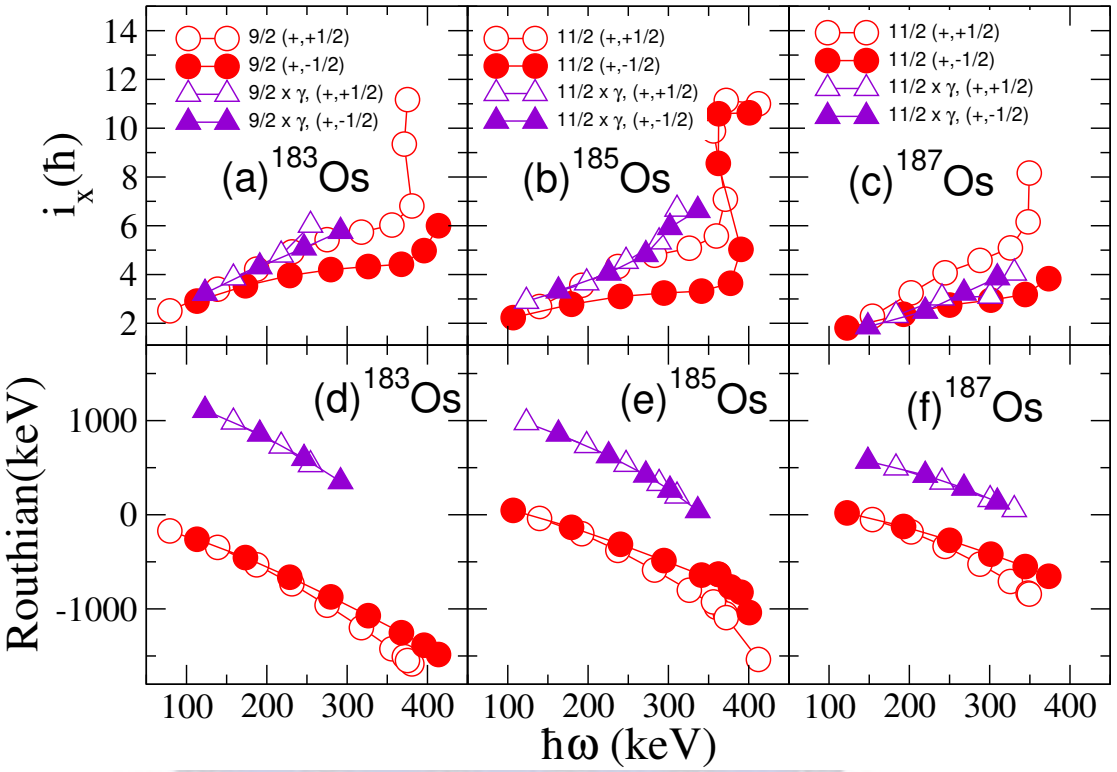

FIGURE 5.8: Alignment and Routhian plots of the bands in ^{187}Os in comparison with those in the ^{183}Os and ^{185}Os isotopes. Harris parameters used here are: $J_0 = 24\ \hbar^2$ MeV^{-1} and $J_1 = 66\ \hbar^4$ MeV^{-3} [13]. The yrast positive-parity bands are labelled by the band-head spin, while the excited bands are labelled as a coupling with the γ band. The signature partner bands are labelled in the same colours, open symbols denote the positive signature and closed symbols represent the negative signature sequences.

quadrupole deformation $\varepsilon_2 = 0.198$, hexadecapole deformation $\varepsilon_4 = 0.054$, pairing gap $\Delta = 0.647$ MeV, $\gamma = 0°$, while the Fermi level was increased to $\lambda = 53.4$ MeV to account for the additional neutron. As expected, the Routhians corresponding to the high-Ω configurations such as 11/2[615] and 9/2[624] do not show signature splitting. However the down-sloping Routhian originating from the 1/2[651] orbital from the $g_{9/2}$ sub-shell interacts strongly with the positive-signature Routhians and pushes them down, creating signature splitting. Therefore signature splitting where the $\alpha = +1/2$ Routhian becomes favoured is predicted by the calculations in agreement with the experimentally observed phase of the signature splitting. On the other hand, the experimental data show signature splitting throughout the whole spin range of the yrast band, while the CSM calculations suggest splitting for rotational frequency above 0.35 MeV (for the lowest-energy Routhian). This indicates that the origin of the signature splitting is most probably of different nature, for instance it can be caused by triaxiality of the nuclear shape.

In the neighbouring Os nuclei the nuclear shape was assumed to be axially symmetric. An assumption of near axially symmetric shape might be suitable for ^{187}Os as well,

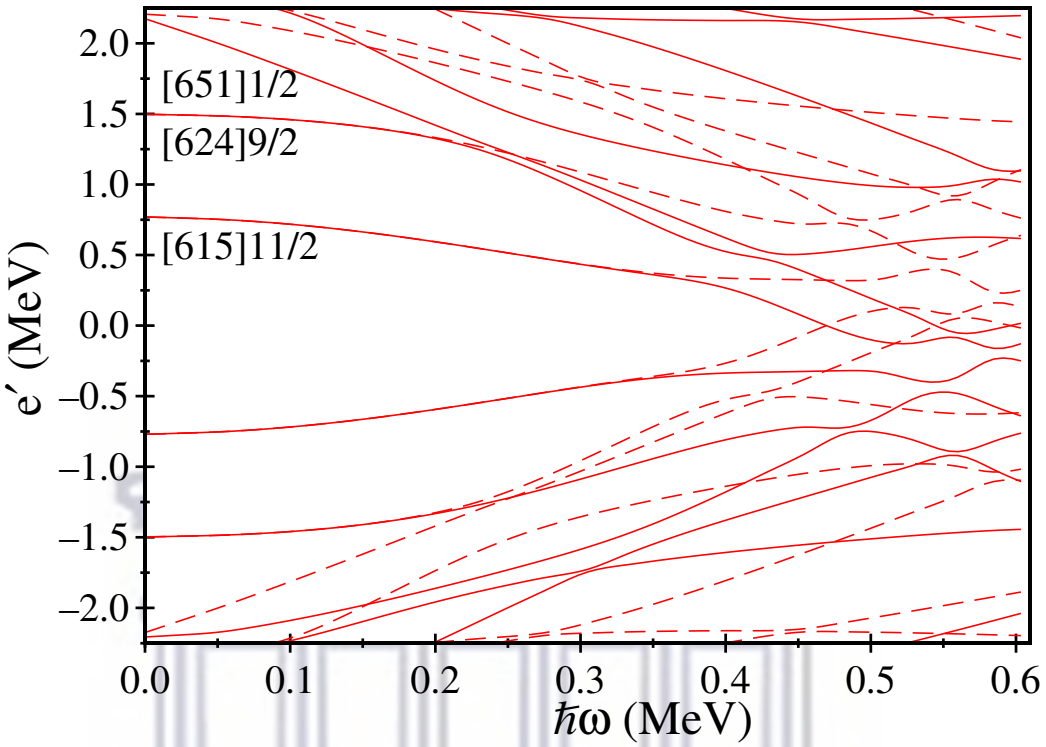

FIGURE 5.9: Cranked shell model positive-parity Routhians for ^{186}Os with N = 110 as a function of the rotational frequency, $\hbar\omega$. In this figure, solid lines represent quasiparticle trajectories with signature $\alpha = +1/2$ and dashed lines are used for quasiparticle trajectories with signature α = -1/2.

however the decreasing trend of the excitation energy of the γ bands with mass, see Fig. 1.2, indicates a more significant role for the γ degree of freedom, where triaxial rigidity might occur. Calculations within the CNSB model, as mentioned earlier, were carried out using standard parameters [84] for the Nilsson potential. The potential energy surface (PES) for the yrast (+,+1/2) configuration is shown in Fig. 5.10. At the ground state I $\approx$ 0.5, the lowest energy minimum corresponds to a well-developed prolate shape at $\varepsilon_2 \approx 0.2$. At higher spin, I $\approx$ 6.5, the potential energy minimum remains at similar quadrupole deformation but shifts to a triaxial shape with $\gamma \approx$ -8°. At spins of I $\approx$ 12.5, the nucleus becomes more triaxial and there is a competition between a rotation around its intermediate axis (the minimum at γ = -17°) and a rotation around its long axis (the minimum at $\gamma \approx$ -105°), with the later minimum being the yrast one. The observed rotational bands in ^{187}Os are collective, thus, the calculations were carried out using a limitation on the deformation mesh to restrict the states to rotation around the intermediate axis.

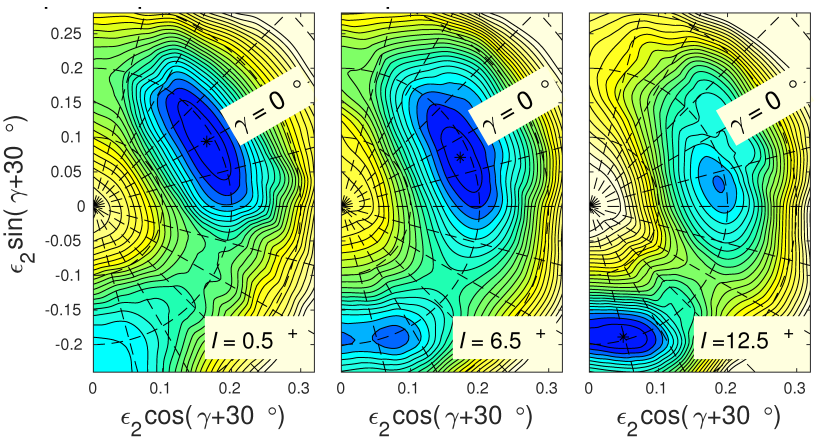

FIGURE 5.10: Calculated total energy surfaces for the yrast $(+, 1/2)$ configuration in the CNSB formalism for increasing spin I. The contour line separation is 0.2 MeV. The absolute minima are indicated by a black asterisk in each of the Figs.

To study further the features of the rotational bands for a deformed triaxial shape we carried out QTR model calculations. The main idea of these calculations is to have a clear understanding of how the excited states of the positive-parity bands in ^{187}Os were generated. The QTR model uses a modified oscillator potential with standard parameters [84] and standard pairing interaction [58]. The deformation parameters were quadrupole deformation of $\varepsilon_2 = 0.21$, hexadecapole deformation of $\varepsilon_4 = 0$, and triaxial deformation of $\gamma = 21°$, while the γ dependence of the moments of inertia was described by the irrotational-flow model. The spin dependence of the moments of inertia were described by Harris parameter of $J_0 = 18.5\ \hbar^2\ \text{MeV}^{-1}$ and $J_0 = 62.5\ \hbar^4\ \text{MeV}^{-3}$. The seven positive-parity orbitals (#25 to #31) that were found near the neutron Fermi level and included in the calculations are listed in Table 5.1. As shown in the Table 5.1, most of these orbitals correspond to major contribution from the $i_{13/2}$ sub-shell. Since the shape is triaxial the orbitals may have contributions from basis wavefunctions with different values of Ω. Orbital #27 was found closest to the Fermi level.

The model couples single-particle and rotational degrees of freedom and calculates the excitation energies and wavefunctions for the states of the predicted rotational bands. Fig. 5.11 shows a comparison of the calculated excitation energies of the two lowest-energy positive-parity bands with the experimental data. The excitation energies for both bands are reproduced well by the model. It is noticeable that while the QTR model predicts signature splitting for the yrast band with the same phase as in the experimental data, it has smaller amplitude.

To understand better the nature of the QTR bands the calculated wavefunctions were examined. In general the rotational bands predicted by the QTR model involve two types of excitations, single-particle, (where the wavefunction comprises a major component

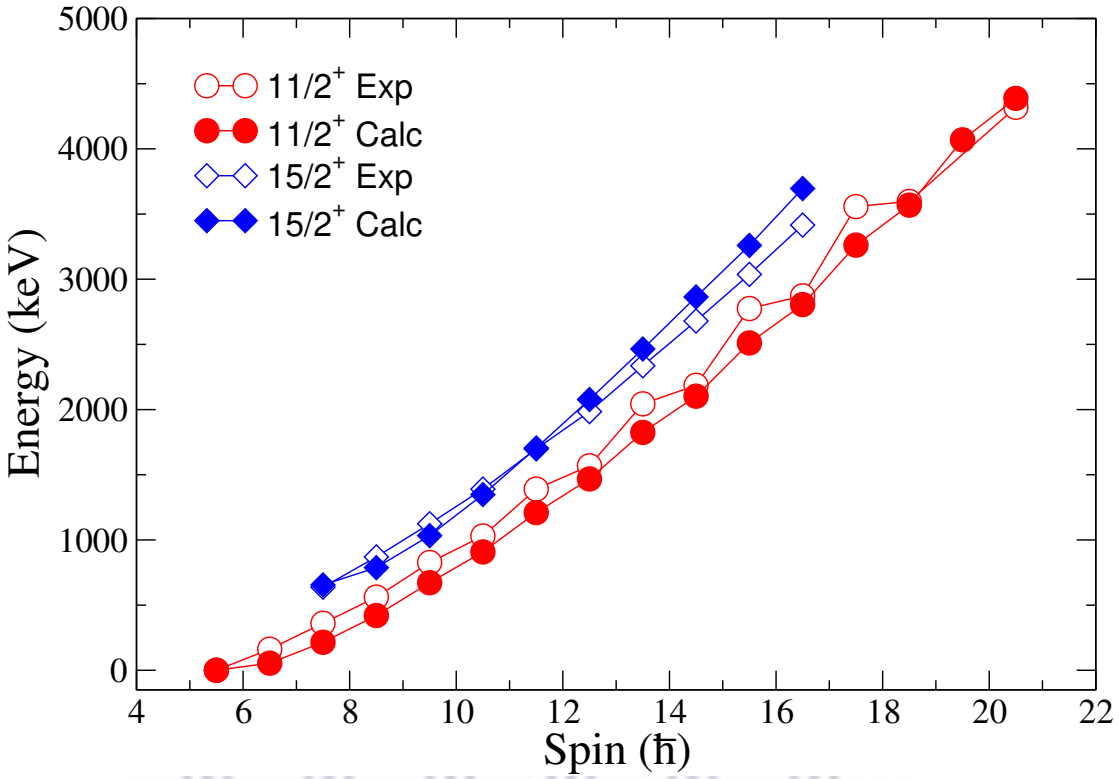

FIGURE 5.11: Calculated excitation energies for the two lowest-energy positive-parity bands of ^{187}Os in comparison with experimental data.

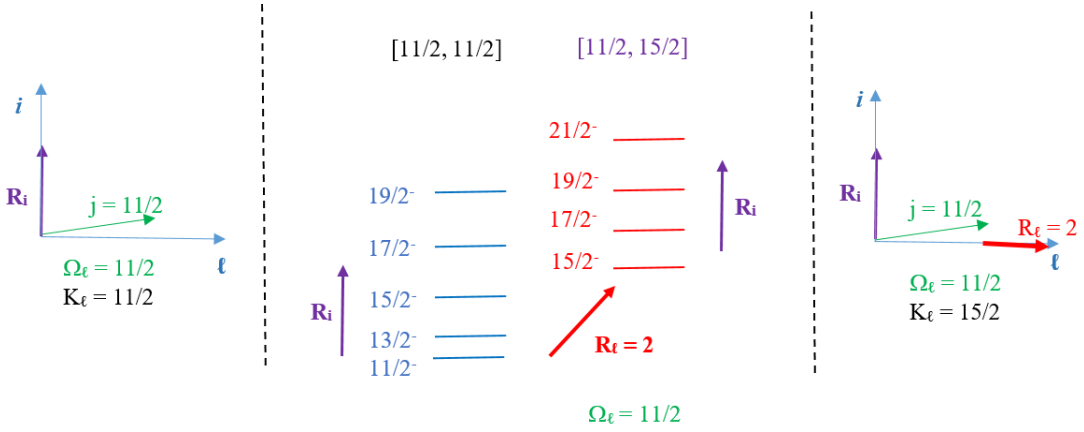

FIGURE 5.12: Sketch illustrating the nature of the collective excitation in QTR model. Both bands illustrated in the middle panel are based on the same single-particle configuration with projection of the angular momentum along the long axis of $\Omega_\ell = 11/2$. The angular momenta coupling for the yrast and excited bands are shown in the left and right panels, respectively. The angular momentum in the yrast band increases due to favourite rotation around the intermediate axis, and the projection of the total angular momentum along the long axis is $K_\ell = \Omega_\ell = 11/2$. The angular momentum in the excited band includes one unit, $2\hbar$, of unfavoured rotation around the long axis, while the remaining rotation is around the intermediate axis, thus $K_\ell = \Omega_\ell + 2 = 15/2$. The bands are labelled according to $[\Omega_\ell, K_\ell]$.

from another single-particle orbital), and collective (where the wavefunction comprises different rotational components). The bands calculated within the QTR represent a precession of the total angular momentum about a given axis. Thus such bands have been called tilted precession (TiP) bands [102].

Fig. 5.12 illustrates schematically the nature of the collective excitations at low rotational frequency assuming that the single-particle component of the wavefunctions remains unchanged and has a dominant contribution from the orbital with projection $\Omega_\ell = 11/2$. A triaxial nucleus with irrotational-flow moments of inertia prefers to rotate around its intermediate axis because this moment of inertia is largest, thus the rotation has lowest energy for given rotational angular momentum. The yrast band, shown in blue in Fig. 5.12, corresponds to such favoured rotation, where the nucleus rotates mainly around its intermediate axis, while the single-particle angular momentum remains aligned along the long nuclear axis. The excited band, shown in red in Fig. 5.12, corresponds to the same coupling, however, it also involves one unit of unfavoured rotation, which is approximately $2\hbar$ along the long axis. The two bands were labelled by the $[\Omega_\ell, K_\ell]$ as [11/2, 11/2] and [11/2, 15/2], respectively. One should keep in mind that the sketch shown in Fig. 5.12 is simplified.

The wavefunctions for the yrast (TiP1) and excited (TiP2) bands in ^{187}Os combine different single-particle and collective contributions and are illustrated in Figs. 5.13 and 5.14. The 11/2 state from the yrast band, see Fig. 5.13, has about 56% contribution from a coupling of orbital #27 with rotation producing $K_\ell = 9/2$, see the column in sky blue. As listed in Table 5.1, orbital #27 is dominated by $\Omega_\ell = 9/2$. Therefore the largest component of the wavefunction is from $\Omega_\ell = K_\ell = 9/2$, of the type [9/2, 9/2]. There are also two significant contributions from orbitals #28 and #29 and with $K_\ell = 11/2$, shown as orange columns, which correspond to a [11/2, 11/2] component. The purple column corresponds to orbital #26 and K = 7/2, therefore to a [7/2, 7/2] component.

The 13/2 state of the yrast, TiP1, band has largest, about 50%, contribution from the [9/2, 9/2] component (column shown in sky blue) and smaller contributions from [11/2, 11/2] (the two columns in orange) and [7/2, 7/2] (the column shown in purple) components. As we approach higher-spin states of this band the contributions associated with orbitals #27, #28 and #29 decrease steadily, while those associated with orbital #26 increase. Such a trend suggests changes in the single-particle component favouring contributions with smaller projections on the long axis. Such a change is understood as induced by Coriolis re-alignment of the angular momentum of the odd neutron away from the long axis and towards the intermediate axis, which is the axis with largest moment of inertia. Therefore the yrast band in ^{187}Os is associated with a major contribution from the $[\Omega_\ell, K_\ell] = [9/2, 9/2]$ component at low spin, but at high spins Coriolis re-alignment

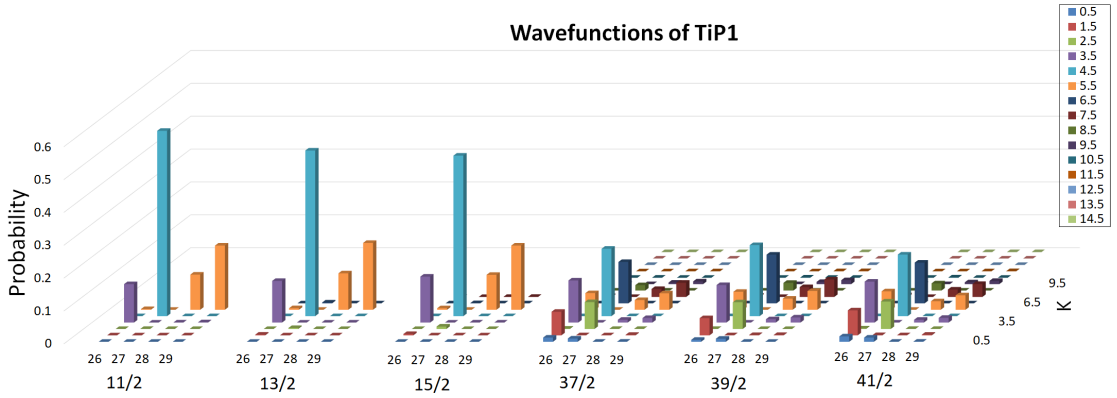

FIGURE 5.13: Contributions of the wavefunctions labelled with their single-particle orbitals and projections K_ℓ on the long axis for the states with I = 11/2-15/2 and 37/2-41/2 from the yrast, TiP1, band in ^{187}Os. The orbitals that contribute to the wavefunction, (26, 27, 28, and 29), are labeled on the x-axis as in Table 5.1. The corresponding K_ℓ values are shown on the y-axis and also illustrated with different colours, see the legend.

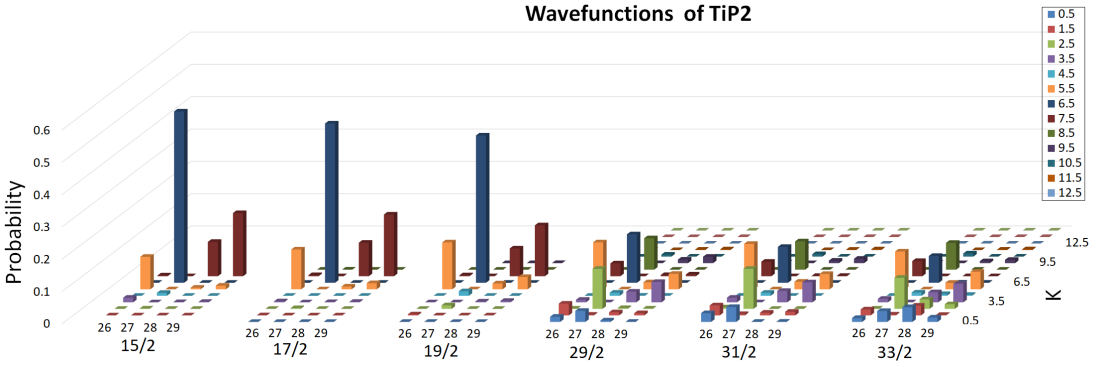

FIGURE 5.14: The same as Fig. 5.13, but for TiP2 band.

of the single-particle angular momentum is also observed. It should be noted that the calculations find the head of this band at I = 11/2 and not I = 9/2, although the largest single-particle configuration is with Ω_ℓ = 9/2. For an axially symmetric nucleus the band head spin of a strongly coupled band has $I = K = \Omega$. This, however, does not necessarily hold true for triaxial shape. In the present case, the QTR model found the lowest-energy $9/2^+$ state at 121.7 keV above the yrast $11/2^+$ state. The wavefunctions for the states from the excited band, TiP2, are illustrated in Fig. 5.14.

There is a major contribution from a coupling of orbital #27 with K_ℓ = 13/2. This [9/2, 13/2] component suggests that there is $2\hbar$ rotation along the long axis, as illustrated in Fig. 5.12 for the excited band (shown in red). The 15/2 state has almost 53% contribution from this [9/2, 13/2] component, as shown by the column in navy blue. The contributions from orbitals #28 and #29, shown in brown, correspond to components

with [11/2, 15/2], while the column in orange represents a [7/2, 11/2] component. Note the similarity in the single-particle component of this state with the wavefunction of the 11/2 state of TiP1 and the added rotational angular momentum of $2\hbar$ along the long axis.

At higher spins the states of TiP2 still have their largest contribution from the [9/2, 13/2] component, but represent a complex mixture of contributions with different nature, in particular there is an increase in the contributions associated with orbital #26 which represents Coriolis re-alignment of the odd neutron away from the long axis.

The QTR calculations successfully describe the observed bands in ^{187}Os. This does not prove that the nuclear shape has stable triaxial deformation. However, one can study the possible rigidity or softness of the nuclear shape if more detailed experimental data become available. For instance, the projection of the total angular momentum on the symmetry axis is a good quantum number for a nucleus with an axially symmetric shape with small vibrations. The yrast and the γ bands in such even-even nuclei correspond to $K = 0$ and $K = 2$. Similarly in odd-mass nuclei the excited and the yrast bands correspond to $\Delta K = 2$. Therefore, the transitions linking the excited and the yrast bands should carry angular momentum of at least $2\hbar$. This indicates that the $\Delta I = 1$ and $\Delta I = 0$ linking transitions should be pure quadrupoles. This is different from the results from the QTR model, where K is not conserved, thus the linking transitions have typically mixed $M1 + E2$ nature. Our data did not have sufficient statistics to measure linear polarization or enough angles to determine precisely the mixing ratios for the linking transitions. Such measurements can be carried out with the upgraded AFRODITE array comprising 17 clover detectors arranged at 7 different measuring angles. The upgrade was completed and is available for experiments.

TABLE 5.1: Composition of the 7 positive-parity orbitals near the neutron Fermi surface which were found to contribute to the levels of the calculated positive-parity bands of ^{187}Os. The orbitals are described as a superposition of spherical shell-model wavefunction, labelled by the corresponding spherical sub-shell, e.g. $i_{13/2}$, and the projection of the single-particle angular momentum on the long axis, Ω_ℓ. The basis wavefunctions with contributions larger than 5%, are listed for each orbital included in the calculations.

Orbital	Contributions by spherical shell-model basis functions
#25	73%($i_{13/2}$, 5/2), 10%($i_{13/2}$, 1/2), 6%($g_{9/2}$, 5/2)
#26	88%($i_{13/2}$, 7/2)
#27	94%($i_{13/2}$, 9/2)
#28	33%($i_{13/2}$, 11/2), 28%($g_{9/2}$, 1/2), 14%($d_{5/2}$, 1/2), 8%($i_{13/2}$,1/2), 6%($g_{9/2}$, 3/2)
#29	63%($i_{13/2}$, 11/2), 15%($g_{9/2}$, 1/2), 8%($d_{5/2}$, 1/2)
#30	31%($g_{9/2}$, 3/2), 17%($i_{11/2}$, 1/2), 10%($g_{7/2}$, 1/2), 9%($i_{11/2}$, 3/2), 8%($i_{13/2}$, 3/2), 8%($d_{5/2}$, 3/2)
#31	97%($i_{13/2}$, 13/2)

Chapter 6

Conclusion

The negative- and positive-parity states in ^{187}Os have been investigated using the AFRODITE array. Our work has extended all bands observed by the previous in-beam work up to high spins. In addition five new bands have been added in the decay scheme of ^{187}Os. The R_{AD} and polarization measurements have been used to assign spin and parity to the observed rotational bands. In order to meaningfully describe the quantum behavior of the newly established structures, the CSM, CNSB and QTR models have been used as well as a systematic comparison with the rotational bands of ^{185}Os. The negative-parity bands have been assigned to the 1/2[510], 3/2[512], 7/2[503] and 9/2[505] neutron configurations. In particular, the new bands 6 and 7 are based on the 9/2[505] configuration. The negative-parity bands that have been previously assigned to 1/2[510](-,-1/2) and 3/2[512](-,-1/2) Nilsson configurations are reviewed based on the new experimental data and their configurations are swapped. Bands 4 and 5 are associated with the 7/2[503] configuration. The good agreement between the theoretical models and the experimental data supports the proposed nucleon configurations of the negative-parity bands in ^{187}Os. Our work has also extended the positive-parity bands 8 and 9 and established two new positive-parity bands decaying to them, namely bands 10 and 11. Based on a comparison with the neighboring isotopes, it was concluded that these new bands (bands 10 and 11) are a result of a coupling of the 2^+ γ band with the 11/2[615] orbital. Indeed, the QTR calculations provide a very good agreement with the experimental data and interprets the newly identified structure as resulting from the three-dimensional rotation of a triaxially deformed nucleus. In spite of this, a description based on the vibrations of a γ soft nuclear shape should also be investigated in order to firmly establish the nature of this excited positive-parity band. In order to distinguish between the possible interpretations based on a stable triaxial shape and on small γ vibrations of an axially symmetric shape, measurements of the mixing ratios of the transitions decaying out of the excited band are needed. Our experimental

setup did not have the geometry neither did the data have sufficient statistics to determine precisely these mixing ratios, however such measurements will be possible with the upgraded AFRODITE array in the near future.

Bibliography

[1] C. Fahlander and G. D. Dracoulis. Sidebands and high-spin states in ^{182}Os. *Nucl. Phys. A*, 375:263, 1982. URL https://doi.org/10.1016/0375-9474(82)90412-2.

[2] C. Wheldon, G. D. Dracoulis, R. T. Newman, P. M. Walker, C. J. Pearson, A. P. Byrne, A. M. Baxter, S. Bayer, T. Kibédi, T. R. McGoram, and *et al.*. Competing phenomena: high-seniority excitations and γ-softness in ^{184}Os. *Nucl. Phys. A*, 699:415, 2002. URL https://doi.org/10.1016/S0375-9474(01)01274-X.

[3] C. Wheldon, P. M. Walker, P. H. Regan, T. Saitoh, N. Hashimoto, G. Sletten, and F. R. Xu. High-K structures and triaxiality in ^{186}Os. *Nucl. Phys. A*, 652:103, 1999. URL https://doi.org/10.1016/S0375-9474(99)00160-8.

[4] V. Modamio, A. Jungclaus, Zs. Podolyak, Y. Shi, F. R. Xu, A. Algora, D. Bazzacco, D. Escrig, L. M. Fraile, S. Lenzi, N. Marginean, T. Martinez, D. R. Napoli, R. Schwengner, and C. A. Ur. Identification of yrast high-intrinsic states in ^{188}Os. *Phys. Rev. C*, 79:024310, 2009. URL https://doi.org/10.1103/PhysRevC.79.024310.

[5] M. A. Cardona, D. Hojman, B. Roussiére, J. Libert, J. Genevey, J. Sauvage, the ISOCELE, ISOLDE, and Collaborations. Low-spin states in ^{182}Os and $K^{\pi} = 0^{+}$, 2^{+} excited bands. *Nucl. Phys. A*, 31:141, 2007. URL https://doi.org/10.1140/epja/i2006-10153-2.

[6] M. Oshima, T. Morikawa, H. Kusakari, N. Kobayashi, M. Sugawara, Y. H. Zhang, A. Ferragut, S. Ichikawa, N. Shinohara, Y. Nagame, and *et al.*. Double-γ vibrational states in ^{168}Er and ^{190}Os. *Nucl. Phys. A*, 557:635c–642c, 1993. URL https://doi.org/10.1016/0375-9474(93)90575-I.

[7] H. Sodan, W. D. Fromm, L. Funke, K. H. Kaun, P. Kemnitz, E. Will, G. Winter, and J. Berzins. Rotational bands in ^{185}Os and ^{187}Os. *Nucl. Phys. A*, 237:333, 1975. URL https://doi.org/10.1016/0375-9474(75)90430-3.

[8] S. N. T. Majola. Exploring the spectroscopy of vibrational levels in the 160 mass region. *PhD Thesis, University of Cape Town and iThemba* LABS, 2015. URL http://hdl.handle.net/11427/20815.

[9] M. Siciliano. Shape coexistence in the neutron-deficient nucleus ^{194}Po: Gamma-ray and electron spectroscopic study employing the sage spectrometer. *MSc Thesis, University of Padua*, 2013. URL https://www.researchgate.net/publication/274733087.

[10] B. R. Mottelson and S. G. Nilsson. Classification of the nucleonic states in deformed nuclei. *Phys. Rev.*, 99:1615, 1955. URL https://doi.org/10.1103/PhysRev.99.1615.

[11] S. G. Nilsson. Binding states of individual nucleons in strongly deformed nuclei. *Mat. Fys. Medd. Dan. Vid. Selsk*, 29:16, 1955. URL https://cds.cern.ch/record/212345/files/p1.pdf.

[12] J. Ndayishimye. Multiple chiral bands in ^{193}Tl. *PhD Thesis, Stellenbosch University*, 2016. URL http://hdl.handle.net/10019.1/98454.

[13] T. Shizuma, S. Mitarai, G. Sletten, R. A. Bark, N. L. Gjørup, H. J. Jensen, M. Piiparinen, J. Wrzesinski, and Y. R. Shimizu. High-spin structure in ^{185}Os. *Phys. Rev. C*, 69:024305, 2004. URL https://doi.org/10.1103/PhysRevC.69.024305.

[14] C. Wheldon, A. E. Stuchbery, A. N. Wilson, G. D. Dracoulis, A. M. Bruce, R. A. Bark, A. P. Byrne, F. M. Prados-Estevez, G. J. lane, C. B. Moon, J. N. Orce, , and R. Wood. Electromagnetic properties of pseudo-Nilsson bands in ^{185}Os. *Eur. Phys. J. A*, 19:319, 2004. URL https://doi.org/10.1140/epja/i2003-10131-2.

[15] T. Shizuma, K. Matsuura, Y. Toh, Y. Hayakawa, M. Oshima, Y. Hatsukawa, M. Matsuda, K. Furuno, Y. Sasaki, T. Komatsubara, and Y. R. Shimizu. Multi-quasiparticle states and K-forbidden transitions in ^{183}Os. *Nucl. Phys. A*, 696: 337, 2001. URL https://doi.org/10.1016/S0375-9474(01)01210-6.

[16] A. Bohr. On the quantization of angular momenta in heavy nuclei. *Phys. Rev.*, 81:134, 1951. URL https://doi.org/10.1103/PhysRev.81.134.

[17] A. Bohr. Nuclear magnetic moments and atomic hyperfine structure. *Phys. Rev.*, 81:331, 1951. URL https://doi.org/10.1103/PhysRev.81.331.

[18] A. Bohr. The coupling of nuclear surface oscillations to the motion of individual nucleons. *Dan. Mat. Fys. Medd*, 26:14, 1952. URL https://www.osti.gov/biblio/4388925.

[19] D. D. Warner, R. F. Casten, and W. F. Davidson. Interacting boson approximation description of the collective states of ^{168}Er and a comparison with geometrical models. *Phys. Rev. C*, 24:1713, 1981. URL https://doi.org/10.1103/PhysRevC.24.1713.

[20] J. M. Allmond and J. L. Wood. Empirical moments of inertia of axially asymmetric nuclei. *Phys. Lett. B*, 767:226, 2017. URL https://doi.org/10.1016/j.physletb.2017.01.072.

[21] G. L. Zimba, S. P. Bvumbi, L. P. Masiteng, P. Jones, J. F. Sharpey-Schafer, S. N. T. Majola, T. S. Dinoko, O. Shirinda, J. J. Lawrie, J. E. Easton, and *et al.*. Yrare low-spin positive-parity states in N = 88 ^{154}Dy. *Eur. Phys. J. A*, 54:59, 2018. URL https://doi.org/10.1140/epja/i2018-12496-3.

[22] S. N. T. Majola, Z. Shi, B. Y. Song, Z. P. Li, S. Q. Zhang, R. A. Bark, J. F. Sharpey-Schafer, D. G. Aschman, S. P. Bvumbi, T. D. Bucher, and *et al.*. β and γ bands in N=88, 90, and 92 isotones investigated with a five-dimensional collective Hamiltonian based on covariant density functional theory: Vibrations, shape coexistence, and superdeformation. *Phys. Rev. C*, 100:044324, 2019. URL https://doi.org/10.1103/PhysRevC.100.044324.

[23] S. N. T. Majola, D. J. Hartley, L. L. Riedinger, J. F. Sharpey-Schafer, J. M. Allmond, C. Beausang, M. P. Carpenter, C. J. Chiara, N. Cooper, D. Curien, and *et al.*. Exploring the spectroscopy of vibrational levels in the 160 mass region. *Phys. Rev. C*, 91:034330, 2015. URL https://doi.org/10.1103/PhysRevC.91.034330.

[24] S. N. T. Majola, M. A. Sithole, L. Mdletshe, D. Hartley, J. Timár, B. M. Nyakó, J. M. Allmond, R. A. Bark, C. Beausang, L. Bianco, and *et al.*. First candidates for γ vibrational bands built on the $[505]11/2^-$ neutron orbital in odd-A Dy isotopes. *Phys. Rev. C*, 101:044312, 2020. URL https://doi.org/10.1103/PhysRevC.101.044312.

[25] L. Mdletshe, S. S. Ntshangase, J. F. Sharpey-Schafer, S. N. T. Majola, T. R. S. Dinoko, N. A. Khumalo, E. A. Lawrie, R. A. Bark, T. D. Bucher, N. Erasmus, and *et al.*. Low-lying positive parity bands in ^{162}Yb. *Eur. Phys. J. A*, 54:176, 2018. URL https://doi.org/10.1140/epja/i2018-12613-4.

[26] J. F. Sharpey-Schafer, R. A. Bark, S. P. Bvumbi, T. R. S. Dinoko, and S. N. T. Majola. Stiff deformed nuclei, configuration dependent pairing and the β and γ degrees of freedom. *Eur. Phys. J. A*, 55:15, 2019. URL https://link.springer.com/article/10.1140/epja/i2019-12665-x.

[27] S. Jehangir, G. H. Bhat, J. A. Sheikh, S. Frauendorf, S. N. T. Majola, P. A. Ganai, , and J. F. Sharpey-Schafer. Quasiparticle and γ-band structures in ^{156}Dy. *Phys. Rev. C*, 97:014310, 2018. URL https://doi.org/10.1103/PhysRevC.97.014310.

[28] J. Ollier, J. Simpson, M. A. Riley, E. S. Paul, X. Wang, A. Aguilar, M. P. Carpenter, I. G. Darby, D. J. Hartley, R. V. F. Janssens, and *et al.*. Structure changes in ^{160}Er from low to ultrahigh spin. *Phys. Rev. C*, 83:044309, 2011. URL https://doi.org/10.1103/PhysRevC.83.044309.

[29] B. Harmatz, T. H. Handley, and J. W. Mihelich *et al.*. Properties of nuclear levels in a number of odd-A nuclei $151 \leq A \leq 191$. *Phys. Rev.*, 128:1186, 1962. URL https://doi.org/10.1103/PhysRev.128.1186.

[30] S. G. Malmskog, V. Berg, B. Fogelberg, and A. Bäcklin. On the low-energy band structure in ^{187}Os. *Nucl. Phys. A*, 166:573, 1971. URL https://doi.org/10.1016/0375-9474(71)90907-9.

[31] K. Ahlgren and P. J. Daly. The level structure of ^{187}Os from the decay of ^{187}Ir. *Nucl. Phys. A*, 189:368, 1972. URL https://doi.org/10.1016/0375-9474(72)90301-6.

[32] P. Morgen, B. S. Nielsen, J. Onsgaard, and C. Søndergaard. The level structure of ^{187}Os. *Nucl. Phys. A*, 204:81, 1973. URL https://doi.org/10.1016/0375-9474(73)90007-9.

[33] R. Thompson and R. K. Sheline. Analysis of the levels of ^{187}Os populated by the (d, t) reaction. *Phys. Rev*, 7:1247, 1973. URL https://doi.org/10.1103/PhysRevC.7.1247.

[34] H. L. Sharma and N. M. Hintz. Osmium isotopes with the (p, t) reaction. *Phys. Rev*, 13:2288, 1976. URL https://doi.org/10.1103/PhysRevC.13.2288.

[35] R. Sahu, M. Satpathy, and L. Satpathy. Microscopic triaxial description of ^{187}Ir, ^{187}Os, and ^{189}Ir. *Phys. Rev. C*, 23:1777, 1981. URL https://doi.org/10.1103/PhysRevC.23.1777.

[36] A. M. Bruce, C. Thwaites, W. Gelletly, D. D. Warner, S. Albers, M. Schimmer, and P. von Brentano. Tests of pseudospin symmetry via coulomb excitation measurements on ^{187}Os and ^{189}Os. *Phys. Rev. C*, 56:1438, 1997. URL https://doi.org/10.1103/PhysRevC.56.1438.

[37] W. Greiner and Joachim A. Maruhn. *Nuclear Models*. Springer and Berlin and Heidelberg, 1996. URL https://link.springer.com/book/10.1007/978-3-642-60970-1.

[38] L. Wilets and M. Jean. Surface oscillations in even-even nuclei. *Phys. Rev.*, 102: 788, 1956. URL https://doi.org/10.1103/PhysRev.102.788.

[39] A. Bohr and B. R. Mottelson. Collective and individual-particle aspects of nuclear structure; 2nd ed. *Dan. Mat. Fys. Medd*, 27:1, 1957. URL https://cds.cern.ch/record/272540.

[40] G. Gervais et al. Collective γ-vibrational bands in ^{165}Ho and ^{167}Er. *Nucl. Phys. A*, 624:257–274, 1997. doi: 10.1016/S0375-9474(97)81838-6. URL https://doi.org/10.1016/S0375-9474(97)81838-6.

[41] R. B. Yadav, W. C. Ma, J. C. Marsh, Q. A. Ijaz, R. V. F. Janssens, M. P. Carpenter, C. R. Hoffman, T. Lauritsen, S. Zhu, F. G. Kondev, G. Gürdal, G. B. Hagemann, D. J. Hartley, L. L. Riedinger, and S. Mukhopadhyay. Multiple excitation modes in ^{163}Hf. *Phys. Rev. C*, 90:054325, Nov 2014. doi: 10.1103/PhysRevC.90.054325. URL https://link.aps.org/doi/10.1103/PhysRevC.90.054325.

[42] J. F. Sharpey-Schafer, T. E. Madiba, S. P. Bvumbi, E. A. Lawrie, J. J. Lawrie, A. Minkova, S. M. Mullins, P. Papka, D. G. Roux, and J. Timár. Blocking of coupling to the 0_2^+ excitation in ^{154}Gd by the $[505]11/2^-$ neutron in ^{155}Gd. *Eur. Phys. J. A*, 47:6, 2011. URL https://doi.org/10.1140/epja/i2011-11006-7.

[43] Y. F. Krechetov. Study of the dynamic properties of nuclei at short nucleon-nucleon distances. *Russian Phys. Journal*, 45:842, 2002. URL https://doi.org/10.1023/A:1022383619078.

[44] O. Shirinda. Studying chirality in A $\sim$ 100, 130 and 190 mas regions. *PhD Thesis, University of the Western Cape*, 2011. URL http://hdl.handle.net/11394/1792.

[45] N. Bohr and J. A. Wheeler. The mechanism of nuclear fission. *Phys. Rev.*, 56: 426, 1939. URL https://doi.org/10.1103/PhysRev.56.426.

[46] K. S. Krane. *Introductory to Nuclear Physics*. John Willey & Sons, 1988.

[47] R. F. Casten. *Nuclear Structure from a Simple Perspective*. Oxford Science Publication Ltd, 2nd ed., 1990.

[48] M.G. Mayer. On closed shells in nuclei. *Phys. Rev.*, 75:1969, 1949. URL https://doi.org/10.1103/PhysRev.75.1969.

[49] O. Haxel, J. Hans D. Jensen, and Hans E. Suess. On the" magic numbers" in nuclear structure. *Phys. Rev.*, 75:1766, 1949. URL https://doi.org/10.1103/PhysRev.75.1766.2.

[50] A. Faessler and W. Greiner. Die rotations-vibrations-wechselwirkung in deformierten gg-kernen. *Z. Phys.*, 168:425, 1962. URL https://doi.org/10.1007/BF01387041.

[51] A. Faessler and W. Greiner. Einteilchen- und kollektivanregung in deformierten kernen ungerader massenzahl. *Nucl. Phys.*, 59:177, 1964. URL https://doi.org/10.1016/0029-5582(64)90076-8.

[52] A. Faessler, W. Greiner, and Raymond K. Sheline. Nuclear models and the osmium isotopes. *Phys. Rev.*, 135:B591, 1964. URL https://doi.org/10.1103/PhysRev.135.B591.

[53] A. Faessler, W. Greiner, and R. K. Sheline. Rotation-vibration-interaction in deformed nuclei. *Nucl. Phys.*, 70:33, 1965. URL https://doi.org/10.1016/0029-5582(65)90224-5.

[54] A. Faessler, W. Greiner, and R. K. Sheline. The coriolis anti-pairing and blocking effects in deformed even nuclei. *Nucl. Phys.*, 62:241, 1965. URL https://doi.org/10.1016/0029-5582(65)90867-9.

[55] A. Faessler and A. Plastino. Surface delta interaction and non-rotational collective states in rare-earth nuclei. *Nucl. Phys. A*, 94:580, 1967. URL https://doi.org/10.1016/0375-9474(67)90433-2.

[56] J. M. Eisenberg and W. Greiner. *Nuclear Models*, volume 1. North Holland Publishing Company, 1970.

[57] D. L. Hill and J. A. Wheeler. Nuclear constitution and the interpretation of fission phenomena. *Phys. Rev.*, 89:1102, 1953. URL https://doi.org/10.1103/PhysRev.89.1102.

[58] S. G. Nilsson, C. F. Tsang, A. S. Z. Szymanski, S. Wycech, C. Gustafson, I. L. Lamm, P. Möller, and B. Nilsson. On the nuclear structure and stability of heavy and superheavy elements. *Nucl. Phys. A*, 131:1, 1969. URL https://doi.org/10.1016/0375-9474(69)90809-4.

[59] D. R. Inglis. Particle derivation of nuclear rotation properties associated with a surface wave. *Phys. Rev.*, 96:1059, 1954. URL https://doi.org/10.1103/PhysRev.96.1059.

[60] D. R. Inglis. Nuclear moments of inertia due to nucleon motion in a rotating well. *Phys. Rev.*, 103:1786, 1956. URL https://doi.org/10.1103/PhysRev.103.1786.

[61] R. Bengtsson and S. Frauendorf. Quasiparticle spectra near the yrast line. *Phys. Rev.*, 327:139, 1979. URL https://doi.org/10.1016/0375-9474(79)90322-1.

[62] R. Bengtsson, S. Frauendorf, and F. R. May. Quasiparticle levels in rotating rare earth nuclei: A cranked shell-model dictionary. *At. Data Nucl. Data Tables*, 35: 15, 1986. URL https://doi.org/10.1016/0092-640X(86)90028-8.

[63] O. Shirinda. Signature splitting and inversion in the $^{186-194}$Au nuclei predicted by the total routhian surface (TRS) and cranked shell model (CSM) calculations. MSc *Thesis, University of the Western Cape*, 2007. URL http://hdl.handle.net/11394/2492.

[64] P. Möller, R. Bengtsson, B. G. Carlsson, P. Olivius, and T. Ichikawa. Global calculations of ground-state axial shape asymmetry of nuclei. *Phys. Rev. Lett.*, 97:162502, 2006. URL https://doi.org/10.1103/PhysRevLett.97.162502.

[65] Z. Szymański. Fast nuclear rotation (Oxford University Press, Oxford), 1983. URL https://www.osti.gov/etdeweb/biblio/6286042.

[66] T. Bengtsson. A method to remove virtual interactions with applications to nuclear spectroscopy. *Nucl. Phys. A*, 496:56, 1989. URL https://doi.org/10.1016/0375-9474(89)90216-9.

[67] A. Bohr and B. R. Mottelson. Some current themes in nuclear research. *Phys. Scr. A.*, 10:13, 1974. URL https://doi.org/10.1088/0031-8949/10/a/002.

[68] B. G. Carlsson, I. Ragnarsson, R. Bengtsson, E. O. Lieder, R. M. Lieder, and A. A. Pasternak. Triaxial shape with rotation around the longest principal axis in ^{142}Gd. *Phys. Rev. C*, 78:034316, 2008. URL https://doi.org/10.1103/PhysRevC.78.034316.

[69] H. L. Ma, B. G. Carlsson, I. Ragnarsson, and H. Ryde. Interpretation of the high spin states in ^{161}Lu: A paired and unpaired study. *Phys. Rev. C*, 90:014316, 2014. URL https://doi.org/10.1103/PhysRevC.90.014316.

[70] K. Heyde. *Basic Ideas and Concepts in Nuclear Physics*. IOP Publishing Ltd, 2nd ed., 1999.

[71] S. K. Abdulvagabova, S. P. Ivanova, and N. I. Pyatov. Excitation of 0^+ states in two-particle transfer reactions. *Phys. Lett. B*, 38:215, 1972. URL https://doi.org/10.1016/0370-2693(72)90382-6.

[72] S. T. Belyaev and B. A. Rumiantsev. Spin-orbit vibrations in nuclei. *Phys. Lett. B*, 30:444, 1969. URL https://doi.org/10.1016/0370-2693(69)90164-6.

[73] D. R. Bes and R. A. Broglia. Pairing vibrations. *Nucl. Phys.*, 80:289, 1966. URL https://doi.org/10.1016/0029-5582(66)90090-3.

[74] D. R. Bes, R. A. Broglia, and B. Nilsson. Importance of the quadrupole pairing field in the $J^{\pi}= 0^{+}$ vibrations of shape deformed nuclei. *Phys. Lett. B*, 40:338, 1972. URL https://doi.org/10.1016/0370-2693(72)90814-3.

[75] R. F. Casten, D. Kusnezov, and N. V. Zamfir. Phase transitions in finite nuclei and the integer nucleon number problem. *Phys. Lett.*, 82:5000, 1999. URL https://doi.org/10.1103/PhysRevLett.82.5000.

[76] R. E. Griffin, A. D. Jackson, and A. B. Volkov. An explanation for the 0^{+} excited pairing state in actinide nuclei. *Phys. Lett. B*, 36:281, 1971. URL https://doi.org/10.1016/0370-2693(71)90703-9.

[77] J. V. Maher, J. R. Erskine, A. M. Friedman, J. P. Schiffer, and R. H. Siemssen. Unexpected strong pair correlations in excited 0^{+} states of actinide nuclei. *Phys. Lett.*, 25:302, 1970. URL https://doi.org/10.1103/PhysRevLett.25.302.

[78] O. Mikoshiba, R. K. Sheline, T. Udagawa, and S. Yoshida. $K= 0^{+}$ excited levels in deformed nuclei and their rotational coupling. *Nucl. Phys. A*, 101:202, 1967. URL https://doi.org/10.1016/0375-9474(67)90299-0.

[79] W. I. van Rij and S. H. Kahana. Low-lying 0^{+} states and (p,t) strengths in the actinides. *Phys. Rev. Lett.*, 28:50, 1972. URL https://doi.org/10.1103/PhysRevLett.28.50.

[80] I. Ragnarsson and R. A. Broglia. Pairing isomers. *Nucl. Phys. A*, 263:315, 1976. URL https://doi.org/10.1016/0375-9474(76)90176-7.

[81] P. E. Garrett. Characterization of the β vibration and 0_2^+ states in deformed nuclei. *Journal of Physics G27*, 27:R1, 2001. URL https://doi.org/10.1088/0954-3899/27/1/201.

[82] W. D. Kulp, J. L. Wood, P. E. Garrett, J. M. Allmond, D. Cline, A. B. Hayes, H. Hua, K. S. Krane, R. M. Larimer, J. Loats, and *et al.*. Identification of a pairing isomeric band in ^{152}Sm. *Phys. Rev. C*, 71:041303(R), 2005. URL https://doi.org/10.1103/PhysRevC.71.041303.

[83] P. B. Semmes and I. Ragnarsson. in Proceedings of the International Conference on High-Spin Physics and Gamma-Soft Nuclei, Pittsburg, 1990, edited by J. X. Saladin, R. A. Sorenson, and C. M. Vincent (World Scientific, Singapore, 1991), p. 500; in Future Directions in Nuclear Physics with 4π Gamma Detection Systems

of the New Generation, edited by J. Dudek and B. Haas (AIP Conf. Proc. 259, 1992), p. 566., 1992.

[84] T. Bengtsson and I. Ragnarsson. Rotational bands and particle-hole excitations at very high spin. *Nucl. Phys. A*, 436:14, 1985. URL https://doi.org/10.1016/0375-9474(85)90541-X.

[85] J. F. Sharpey-Schafer. Laboratory portrait: iThemba laboratory for accelerator-based sciences. *Nucl. Phys. News Int.*, 14:5, 2004. URL https://doi.org/10.1080/10506890491034686.

[86] A. Gavron. Statistical model calculations in heavy ion reactions. *Phys. Rev. C*, 21:230, 1980. URL https://doi.org/10.1103/PhysRevC.21.230.

[87] O. B. Tarasov and D. Bazin. Beam interactions with materials and atoms. *Nucl. Instr. and Meth., B*, 266:4657, 2008. URL https://doi.org/10.1016/j.nimb.2008.05.110.

[88] H. Morinaga and P. C. Gugelot. Gamma rays following (α, xn) reactions. *Nucl. Phys.*, 46:210, 1963. URL https://doi.org/10.1016/0029-5582(63)90581-9.

[89] F. S. Stephens, N. L. Lark, and R. M. Diamond. Rotational states produced in heavy-ion nuclear reactions. *Nucl. Phys.*, 63:82, 1965. URL https://doi.org/10.1016/0029-5582(65)90854-0.

[90] R. Bock. *Heavy Ion Collisions*. North Holland, Amsterdam, 1980.

[91] K. S. Krane. *Tables of coefficients for analysis of angular distribution of gamma radiation from oriented nuclei*. Los Alamos National Lab, 1971. doi: 10.2172/4023856. URL https://www.osti.gov/biblio/4023856.

[92] G. F. Knoll. *Radiation Detection and Measurement*. John Willey & Sons, Inc. 3^{rd} ed., 2000. URL https://phyusdb.files.wordpress.com/2013/03/radiationdetectionandmeasurementbyknoll.pdf.

[93] Nuclear Physics Group. Multi Instance Data Acquisition System, 2019. http://npg.dl.ac.uk/MIDAS/index.html.

[94] J. Cresswell and J. Sampson. MTsort Language - EDOC033. University of Liverpool, 2015. http://npg.dl.ac.uk/MIDAS/manual/MTsort/edoc033.pdf.

[95] P. Jones, R. Bark, S. P. Bvumbi, T. D. Bucher, T. R. S. Dinoko, J. L. Easton, M. S. Herbert, B. V. Kheswa, N. Khumalo, E. A. Lawrie, and *et al.*. Development of the iThemba LABS Digital Data Acquisition System. *Annual Report*, 2013. URL https://tlabs.ac.za/wp-content/uploads/pdf/annaul_reports/Annual_Report_2013_small.pdf.

[96] L. Makhathini. Developing a tape station for β-decay studies at iThemba LABS. *PhD Thesis, Stellenbosch University*, 2020. URL http://hdl.handle.net/10019.1/110041.

[97] D. C. Radford. Escl8r and levit8r: Software for interactive graphical analysis of hpge coincidence data sets. *Nucl. Instr. and Meth., A*, 361:297, 1995. URL https://doi.org/10.1016/0168-9002(95)00183-2.

[98] M. C. Lederer and V. S. Shirley. *Table of Isotopes, 7th Edition,*. John Wiley & Sons, 1978. URL https://www.amazon.com/Table-Isotopes-C-Michael-Lederer/dp/0471041807.

[99] H. Morinaga and T. Yamazaki. *In-Beam Gamma-Ray Spectroscopy*. Amsterdam New York Oxford: North-Holland Publishing Company, 1976. URL https://www.osti.gov/biblio/5297390.

[100] W. B. Ewbank. Nuclear data sheets for A = 187: W, Re, Os, Ir, Pt, Au, Hg. *Nucl. Data B*, 1:23, 1966. URL https://doi.org/10.1016/S0090-550X(66)80095-5.

[101] T. W. Conlon. High-resolution studies of the gamma rays from isomeric states with half-lives of 10μs - 30ms in nuclei with Z = 63-83. *Nucl. Phys. A*, 100:545, 1967. URL https://doi.org/10.1016/0375-9474(67)90123-6.

[102] E. A. Lawrie, O. Shirinda, and C. M. Petrache. Tilted precession and wobbling in triaxial nuclei. *Phys. Rev. C*, 101:034306, 2020. URL https://doi.org/10.1103/PhysRevC.101.034306.